NTNU – Trondheim
Norwegian University of
Science and Technology

Formation of Silicon Carbide and Graphite in the Silicomanganese Process

Jonas Einan

Materials Technology
Submission date: June 2012
Supervisor: Merete Tangstad, IMTE
Co-supervisor: Per Anders Eidem, Eramet Norway AS

Norwegian University of Science and Technology
Department of Materials Science and Engineering

I hereby declare that this work has been carried out independently and in compliance with the examination regulations of the Norwegian University of Science and Technology, NTNU.

Jonas Einan

Trondheim, June 2012

Preface

This thesis describes an investigation of formation of SiC and graphite in the silicomanganese process. The work is the master thesis of the author, and the basis for evaluation in the course TMT 4905 at the Norwegian University of Science and Technology, NTNU. The work has been based on a collaboration between NTNU and Eramet Norway AS, and was part of the Resource Optimization and Recovery in the Material Industry (ROMA) project.

I would like to give my utmost gratitude to my supervisor, Professor Merete Tangstad. Merete has passionately guided me in the world of process metallurgy, and given me courage and support. In addition Merete gave us the oppurtunity to go to TMS in Florida, which was an enjoyable excursions both academically and socially.

An equally large thanks goes to my co-supervisor, Dr. Per Anders Eidem at Eramet Norway AS. First of all I want to thank Per Anders for arousing my interest, and recruiting me into the metallurgical process community with open arms. Your cheerful guidance has been an inspiration throughout the past year.

I would like to thank my fiancee, Gro Anja for unconditional support and love.

At last I would like to thank my fellow graduate students at material science for mischief and fun during the last two years.

Jonas Einan

Trondheim, June 2012

Abstract

When a liquid SiMn alloy is cooled, carbon is dissolved from the melt. The dissolved carbon either forms graphite or reacts with silicon from the melt to form SiC. The goal of this thesis has been to determine how temperature fluctuations affect the formation of SiC and graphite in the SiMn process. The focus of this thesis has been on dissolved carbon from the SiMn alloy due to cooling of the system, and the formation of graphite and SiC from this dissolution of carbon.

The experiments conducted in this thesis is done with near constant silicon content, and temperature as the main variable in addition to carbon. The investigation was carried out by heating SiMn alloys several times, forming SiC and graphite. Carbon from the crucibles dissolved into the liquid SiMn alloy to reach equilibrium between carbon and silicon. This is equivalent to an industrial furnace where coke can dissolve carbon into the SiMn alloy, and thus form SiC or graphite. Accumulation of graphite and SiC is believed to be bad for furnace operations.

SiC that forms in a $Mn-Si-Fe-C_{sat}$ alloy can have an interface structure of granular, angular grains and as dendrites. When SiC accumulates in the $Mn-Si-Fe-C$ system, clusters of SiC particles with intermediate SiMn metal can form. This study shows that SiC clusters is typically a decade larger than the average SiC particle. The SiC particles settles at the top of the melt when a cooling rate of $18^{\circ}\mathrm{C}/_{min}$ is used.

Graphite that forms in the $Mn-Si-Fe-C$ system have an interface structure of flakes. When the carbon content of the liquid SiMn is high enough, nucleation of new graphite grains happens instead of grain growth. The graphite flakes did not settle, but remained evenly dispersed in the SiMn alloy. This may be due to high viscosity in the melt, high friction on the graphite flakes or the buoyancy can be fairly equal to the drag of the graphite particles.

The rate of formation of $^{SiC}/_{graphite}$ in $Mn-Si-Fe-C_{sat}$ alloys is reduced slightly by each consecutive temperature cycle. This suggest that $^{SiC}/_{graphite}$ formed during the first cycles only partly dissolve into the liquid SiMn alloy to reach equilibrium in the system.

Sammendrag

Når en flytende SiMn legering blir kjølt ned, vil karbon bli oppløst fra smelten. Karbon som bli oppløst danner enten grafitt eller SiC ved å reagere med silisium fra smelten. Målet med denne oppgaven har vært å kartlegge hvordan temperatursvingninger påvirker dannelsen av SiC og grafitt i SiMn prosessen. Fokuset i oppgaven har vært på oppløst karbon fra SiMn legeringen når den blir kjølt ned, og dannelsen av grafitt og SiC fra oppløst karbon.

Forsøkene som er utført i denne oppgaven har hatt nær konstant silisium innhold, der temperatur er hovedvariabelen i tillegg til karbon. Undersøkelsen har blitt utført ved å varme SiMn legeringer flere ganger, for så å danne SiC og grafitt. Karbon fra diglene ble oppløst i SiMn legeringene for å nå likevekt mellom karbon og silisium. I en industriell ovn vill dette tilsvare at koks i ovnen vil bli oppløst i SiMn legeringen, og dermed danne SiC eller grafitt.

SiC som dannes i en $Mn-Si-Fe-C$ legering kan være strukturert som granulære, vinkelformede korn og som dendritter. Når SiC akkumuleres i $Mn-Si-Fe-C$ systemet, kan klaser av SiC partikler med mellomliggende SiMn metall dannes. Denne studien viser at SiC klasene har typisk en dekade større areal enn de gjennomsnittlige SiC partiklene. SiC partiklene legger seg på toppen av smelten når en nedkjølingshastighet på $18^{\circ}C/_{min}$ blir benyttet.

Grafitt som dannes i $Mn-Si-Fe-C$ systemet er strukturert som flak. Når innholdet av karbon i den flytende SiMn legeringen er høy nok, vil kimdanning av nye grafittkorn skje istedenfor kornvekst. Grafittflakene la seg ikke på toppen av smelten, men forble gjevnt fordelt i SiMn legeringen. En årsak til dette kan være høy viskositet i smelten, høy friksjon på grafittflakene eller oppdriften kan være ganske lik drakraften på grafittpartiklene.

Dannelseshastigheten av $SiC/_{grafitt}$ i $Mn-Si-Fe-C_{sat}$ legeringer blir noe redusert etter hver påfølgende temperatur syklus. Dette tyder på at $SiC/_{grafitt}$ som blir dannet iløpet av de første syklusene kun blir delvis oppløst i den flytende SiMn legeringen for å oppnå likevekt i systemet.

Contents

Preface **i**

Abstract **iii**

Sammendrag **v**

Contents **vi**

Symbols ix

1 Introduction **1**

2 Theory **3**

2.1 The Si-C system 3

2.2 Production of silicomanganese 6

2.3 Formation of silicon carbide and graphite 9

2.3.1 Formation and phases of SiC and graphite from previous experiments . . . 10

2.3.2 Growth of SiC on carbon 12

2.3.3 Buoyancy 13

2.4 Nucleation 15

2.5 Interface structure 17

3 Experimental **21**

3.1 Raw materials . . . 21

3.2 Vertical tube furnace . . . 22

3.2.1 Experimental setup . . . 24

3.2.2 Sample preparation and experimental parameters . . . 27

3.3 Analyses of the samples . . . 29

3.3.1 Grid analyses . . . 29

3.3.2 Picture analyses . . . 32

3.3.3 Distribution of carbon . . . 33

4 Results **34**

4.1 LC SiMn . . . 34

4.2 Std SiMn . . . 44

4.3 HC SiMn . . . 52

5 Discussion **61**

5.1 Mechanism . . . 61

5.1.1 Main mechanism . . . 62

5.1.2 Mass balance of carbon . . . 62

5.1.3 Rate of formation . . . 64

5.2 Interface structure of SiC and graphite grains . . . 67

5.2.1 Interface structure of SiC . . . 67

5.2.2 Interface structure of graphite . . . 68

5.3 Placement of SiC and graphite grains . . . 69

5.3.1 Placement of SiC . . . 70

5.3.2 Placement of graphite . . . 70

5.4 Uncertainty . . . 72

5.5 Formation of cavities . . . 72

5.6 Industrial formation of SiC and graphite . . . 73

6 Conclusion **75**

Bibliography **76**

Appendix **78**

A Microscope pictures **79**

B Datasheet of the crucible material IG-15 **107**

Symbols

Roman Symbols

F_R	Force on a spherical particle in laminar flow
F_R	Resultant force
r^o	Critical radius of a crystal
$T_{m,}$	Equilibrium solidification temperature
v	Velocity
A	Area
C	Number of components
F	Number of degrees of freedom
g	Gravity
k	Reaction constant
K	equilibrium constant
P	Number of phases
R	Number of restrictions
r	Rate of formation
Re	Reynold's number
V	Volume

Abbreviations

C_{gr}	Carbon in the form of graphite
EPMA	Electron probe micro-analyzer
FeSi	Ferrosilicon

SAF Submerged arc furnace

SiC Silicon carbide

SiMn Silicomanganese

Greek Symbols

ΔT_k Kinetic undercooling

α Dimensionless entropy

$\alpha - SiC$ Phase of SiC

$\beta - SiC$ Phase of SiC

ΔG Gibbs free energy

Δg Gibbs free energy difference per unit volume

ΔG_i Surface free energy change

ΔG_v Volume free energy change

Δs_f Entropy of fusion per unit volume

ΔT_c Constitutional undercooling

ΔT_r Curvature undercooling

ΔT_t. Thermal undercooling

$\Delta_f H^\circ$ Standard enthalpy of formation

Γ Gibbs-Thomson coefficient

γ Activity coefficient of the staded species

μ Viscosity

ρ Density of the stated species

σ Solid/liquid interface energy

S° Standard entropy

Chapter 1

Introduction

section

In silicomanganese (SiMn) production manganese oxides and silica (SiO_2) are reduced from a liquid slag to metal. The standard alloy produced usually consist of 17-20 wt.% silicon and c. 2 wt.% carbon. The customer usually wants a carbon content as low as possible, and this can be achieved by adding sources of silicon such as off grade silicon metal and thus refining the std. SiMn alloy. The resulting SiMn alloy has a low carbon (LC) content and typically a silicon content of c. 29-30 wt.%. The alloy is usually tapped from the submerged arc furnace (SAF) in a discontinuous process, and the temperature of the furnace is known to fluctuate. (Olsen et al. 2007)

A dig out of a furnace is a good way to investigate the process of producing SiMn alloys, and this was done at Furnace 2, Eramet Norway Kvinesdal during the spring 2009. The furnace produced standard SiMn with c. 20 wt.% silicon before the furnace was shut down. Loose samples and drill cores was gathered from the cokebed and investigated, and some silicon carbide (SiC) was found between the electrodes. (Davidsen 2011)

The accumulated SiC in the furnace does not react with slag to form metal, and is thus a loss of silicon. Accumulated SiC or graphite in the furnace is also belived to have a bad influence on the furnace operation. To control the formation of SiC and graphite in the submerged arc furnace it is important to understand how it is formed.

There are two stable phases of carbon in the $Mn-Si-Fe-C$ system. Graphite is the stable phase up to c. 16 wt.% silicon where SiC will take over as the stable carbon phase in the system. The graphite and SiC can form in a SiMn alloy when the melt is cooled and carbon is thus dissolved from the alloy. Normal temperature fluctuations in the submerged arc furnace, over time, is belived to cause formation of SiC and graphite.

Davidsen (2011) found that SiC can form in the reaction between silicon and dissolved carbon in a $Mn-Si-Fe-C$ alloy. This reaction is to be investigated in this thesis. The goal of this thesis will be to determine how temperature fluctuations affect the formation of SiC and graphite in SiMn alloys. The study is limited to the formation of SiC and graphite from the reaction between

silicon and dissolved carbon in the SiMn alloy. Experiments with numerous heating cycles has been conducted in this thesis, and industrial materials have been used to simulate the industrial process to as large degree as possible.

Chapter 2

Theory

This thesis examines the formation of and graphite in the Si-Mn-Fe-C system. Theory of the Si-C system, production of SiMn, formation of SiC, nucleation of grains and the interface structure of SiC and graphite is used to better understand and explain the formation of SiC and graphite.

2.1 The Si-C system

The binary phase diagram of silicon and carbon are presented in Figure 2.1. SiC is the only stable phase in addition to pure silicon and graphite in the Si-C system. Due to high temperatures it is difficult to determine the exact values of the Si-C binary phase diagram and several liquidus temperatures are suggested. The temperature of decomposition of SiC is reported to be $2834 \pm 40^{\circ}C$ in Figure 2.1. Other reported decomposition temperatures of SiC are $2830^{\circ}C$ in HSC chemistry 5.1 by Roine (2002), $2986^{\circ}C$ in SI Chemical Data and $2300^{\circ}C$ by Washington Mills. (WashingtonMills 2012, Aylward & Findlay 2008)

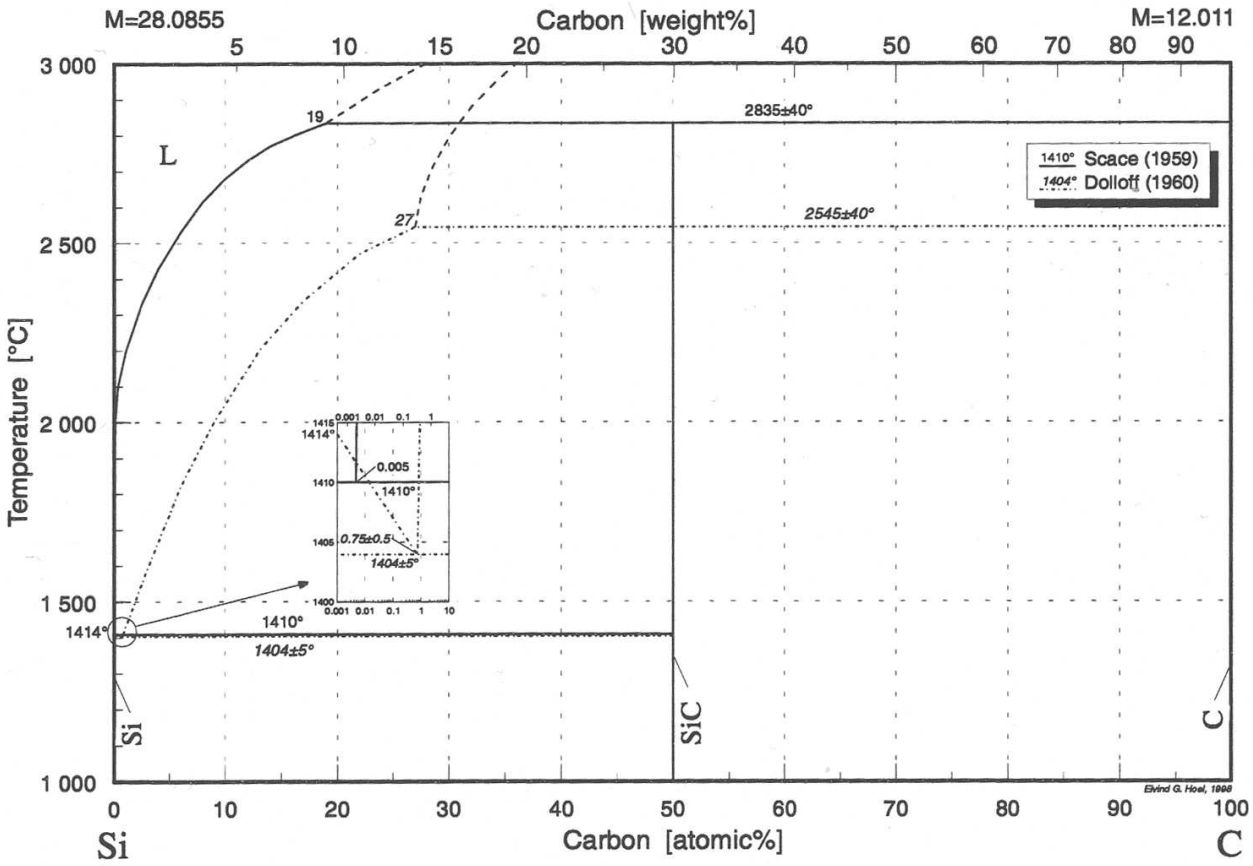

Figure 2.1: The Si-C equilibrium phase diagram. Figure is taken from Hoel (1998).

The maximum operation temperature in the SiMn process is between 1600-1700°C, and the interesting temperature area in Figure 2.1 is thus below 2000°C. The binary phase diagram Si-C is a peritectic system with SiC as the only intermediate compound. The stoichiometric composition of SiC is 50 at.% Si and 50 at.% C. Below 50 at.% C the system will consist of solid or liquid Si and solid SiC. Above 50 at.% C the system will consist of solid graphite and SiC. (Olsen et al. 2007)

Silicon carbide has a hardness between 9 and 10 on Moh's hardness scale and is thus one of the hardest substances in the world. Silicon carbide does not melt, but decomposes at temperatures above c. 2800°C. It is insoluble in water, acids and bases,but can be solved in unsaturated metal and oxide melts. The impurities in technical silicon carbide consists of free C and SiO_2 in varying amounts. Other impurities as silicon, iron and small quantities of aluminum and calcium may also occur (WashingtonMills 2012, Lindstad 2002)

SiC can be divided into two different phases, α- and β-SiC as presented in Table 2.1. The different polytypes are defined by different ways of stacking the SiC layers, while the thermodynamical differences are considered to be insignificant. α-SiC can have over 200 different polytypes which have hexagonal or rhombohedral structure.

Table 2.1: The most common polytypes of α- and β-SiC, their heat of formation and entropy at 25°C. "C" is the cubic crystal structure, "H" is hexagonal and "R" is rhombohedral. The table is made by Davidsen (2010) with data from Chase (1998).

SiC type	Polytypes	$\Delta_f H^\circ \left[{}^{kJ}/_{mol}\right]$	$S^\circ \left[{}^{J}/_{Kmol}\right]$
α-SiC	4H	-71.546 $\pm$ 6.3	16.485 $\pm$ 0.13
	6H		
	15R		
β-SiC	3C	-73.220 $\pm$ 6.3	16.610 $\pm$ 0.13

β-SiC has a cubical crystal structure and is the most stable SiC phase up to c. 1700°C according to JANAF thermochemical tables. Above 1700°C the stability difference is believed to be small, however the main product of the Acheson process is α-SiC, thus this structure is favored when the temperature exceeds c. 2000°C. (Chase 1998)

The colour of silicon carbide can be affected by crystal structure, polytype and impurities. Pure $\alpha-$SiC is white while pure β-SiC is yellow. According to Nelson et al. (1966) an increasing amount of impurities will result in a blue-black colour for both α- and $\beta-$SiC. The colour variations of SiC as a function of impurities are presented in Table 2.2.

Table 2.2: Colours SiC can take caused by crystal structure, different polytypes and impurities. "H" is hexagonal crystal structure and "R" is rhombohedral crystal structure. The table is made by Davidsen (2011) with data from WashingtonMills (2012), Lindstad (2002), Harris (1995)

Impurity element	α-SiC	β-SiC
Pure	colorless	yellow
Nitrogen	green (6H)	yellow-green
	yellow-orange (4H, 8H)	
	orange-yellow (15R)	
Aluminium	blue-black	
Boron	brown-black	

2.2 Production of silicomanganese

Silicomanganese is produced when oxide raw materials are reduced in an submerged arc furnace (SAF). Carbon, in the form of coke, is usually used as the reducing agent. Energy is supplied through electrodes, generating heat through ohmic heating of the coke bed. Silicomanganese is typically produced from a mixture of high carbon ferromanganese (FeMn) slags, manganese ores, quartzite, fluxes, some silicon remelts and coke. The low carbon silicomanganese (LC SiMn) is produced by upgrading standard SiMn (std. SiMn) with adding waste silicon or other sources of silicon from the ferrosilicon (FeSi) industry. After the alloy is casted it can be crushed to meet the customers demands in respect to sizing, and the smaller the size reduction is the better the product. Olsen et al. (2007)

The inside of the SiMn furnace can be divided into two zones as presented in Figure 2.2. The first is the prereduction or preheating zone, where the charge materials is still solid. The second zone is the cokebed, where the slag, fluxes and ores are liquid. The reduced metal drains down through the cokebed to the bottom of the furnace, creating a separate metal layer. (Olsen & Tangstad 2004)

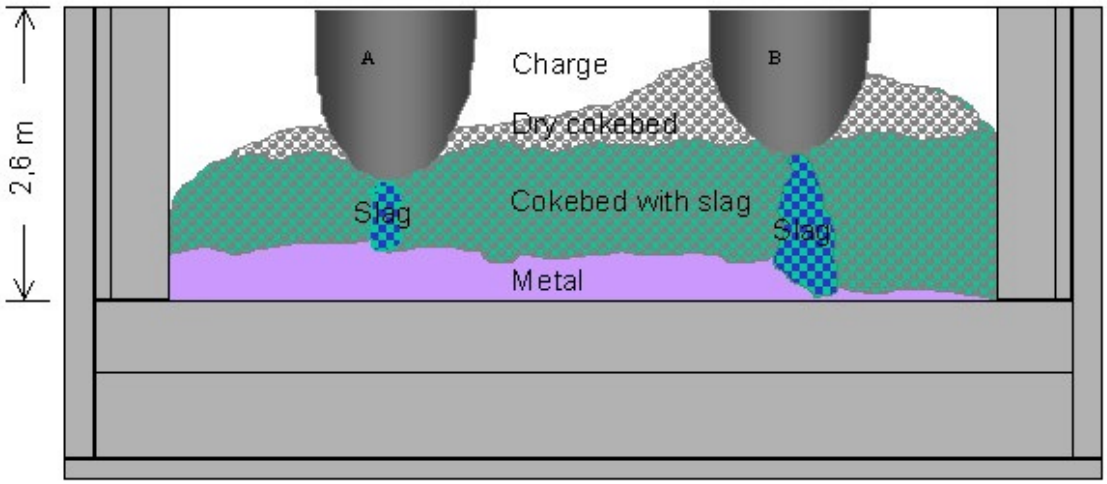

Figure 2.2: Zones in an excavated SiMn furnace. Figure is taken from Olsen & Tangstad (2004)

The MnO and SiO_2 are reduced from the slag. The distribution between metal and slag is controlled by the following equilibrium reactions:

$$(SiO_2) + 2C = \underline{Si} + 2CO(g) \tag{2.1}$$

$$(MnO) + C = \underline{Mn} + CO(g) \tag{2.2}$$

$$(SiO_2) + 2\underline{Mn} = \underline{Si} + 2(MnO) \tag{2.3}$$

$$(SiO_2) + \underline{Si} = 2SiO(g) \tag{2.4}$$

$$\underline{Mn} = Mn(g) \tag{2.5}$$

The parentheses indicates species in the slag and underscore indicates species in alloy. The expected silicon content in an SiMn alloy can be derived from Equation (2.1). The equilibrium constant of Equation (2.1) is dependent on the activity of silicon, the pressure of CO, the activity of SiO_2 in the slag and the activity of carbon as presented in Equation (2.6). In the SiMn furnace the pressure of CO is assumed to be 1 and the activity of carbon is assumed to be unit. Equation (2.6) can be rewritten as Equation (2.7) and thus the expected content of silicon is given by Equation (2.8).

$$K = \frac{a_{Si} \cdot p_{CO}^2}{a_{SiO_2} \cdot a_C^2} \tag{2.6}$$

$$K = \frac{\%Si \cdot \gamma_{Si}}{a_{Si} \cdot \%SiO_2 \cdot \gamma_{SiO_2}} \tag{2.7}$$

$$\%Si = \frac{K(T) \cdot \%SiO_2 \cdot \gamma_{SiO_2}}{\gamma_{Si}} \tag{2.8}$$

The silicon content in an SiMn alloy is dependent on the temperature dependent , K(T), wt.% SiO_2 in the slag, the activity coefficient of SiO_2, γ_{SiO_2}, and the activity coefficient of silicon, γ_{Si}. γ_{SiO_2} is dependent on other species in the slag and γ_{Si} is dependent on other species in the alloy. Thus the silicon content is also dependent on other species in the slag and alloy.

The effect of temperature on silicon content in an Mn-Si-C_{sat} alloy is presented in Figure 2.3. The Mn-Si-C_{sat} alloy is in equilibrium with a $SiO_2 - CaO - Al_2O_3 - MnO$ slag with ${}^{CaO}/_{Al_2O_3} = 4$. The solubility of silicon increases with increasing temperature.

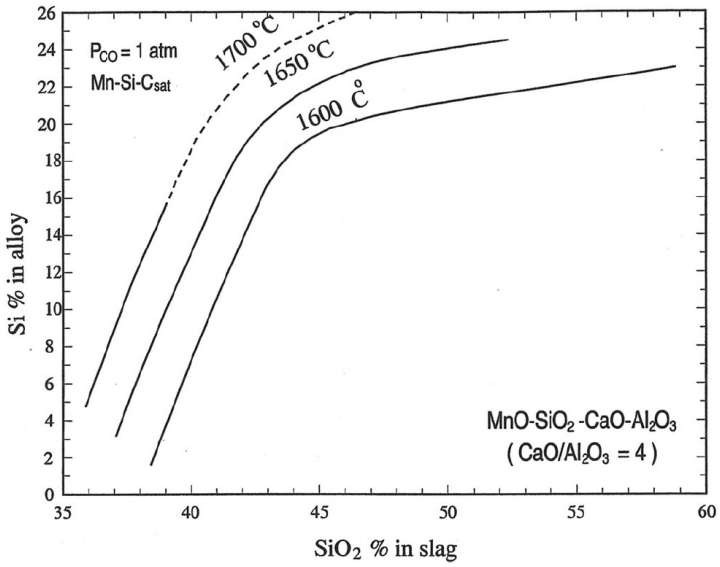

Figure 2.3: (a) The effect of temperature on silicon content in an Mn-Si-C_{sat} alloy in equilibrium with a $SiO_2 - CaO - Al_2O_3 - MnO$ slag with ${}^{CaO}/_{Al_2O_3} = 4$. Figure is taken from Olsen (2001)

The SiMn-alloy is usually graded by its carbon content, and a low carbon content is preferred by the customer. The solubility of carbon in a Mn-Fe-Si-C_{sat} alloy decreases with the silicon content. Olsen et al. (2007) made the solubility diagram of carbon and silicon in a Mn-Fe-Si-C_{sat} alloy with additional data from Tuset & Sandvik (1970) as presented in Figure 2.4. It can be seen from Figure 2.4 that a Mn-Fe-C_{sat} alloy have a carbon content between 7 and 8 wt.% at 1600°C. A Mn-Fe-Si-C_{sat} alloy with 25 wt.% silicon will have less than 1 wt.% carbon at 1600°C.

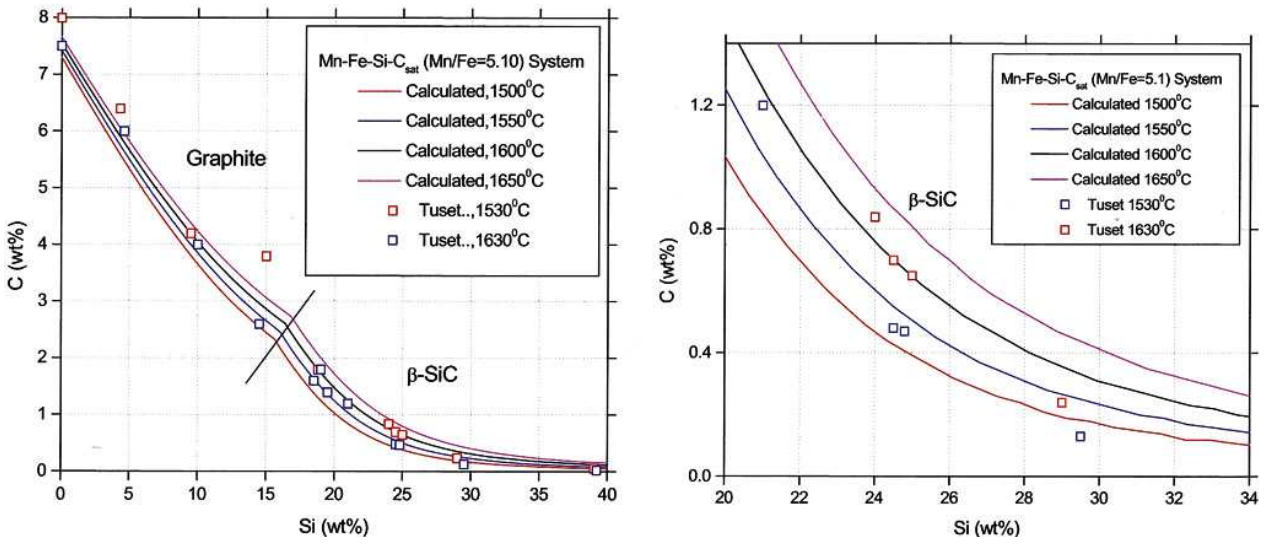

Figure 2.4: Calculated carbon solubility as a function of silicon content in a Mn-Fe-Si-C_{sat} alloy with ${}^{Mn}/_{Fe}$ = 5.1 between 1500°C and 1600°C. The graph on the right side show a close up of the high silicon area. Figure is taken from Olsen (2001)

2.3 Formation of silicon carbide and graphite

The solubility lines in Figure 2.4 is the equilibrium of carbon in the liquid Mn-Fe-Si-C_{sat} alloy when $^{graphite}/_{SiC}$ is present. The line between graphite and SiC in Figure 2.4 is the coexisting point, where SiC replaces graphite as the stable carbon phase. In the furnace the alloy will always be saturated on carbon due to the presence of coke. The solubility of carbon in the Mn-Fe-Si-C_{sat} alloy is reduced with decreasing temperature as presented in Figure 2.4. At 28 wt.% silicon and 1600°C the carbon content solved in the Mn-Fe-Si-C_{sat} alloy is c.0.4 wt.%. If the temperature would be reduced to 1500°C the solubility of carbon would be reduced to c.0.2 wt.%. The dissolved carbon would react with silicon in the liquid alloy and form SiC as presented in equation 2.9. The carbon can also react with slag with high silica content as presented in Equation (2.10).(Olsen et al. 2007)

$$C + \underline{Si} = SiC\,(s) \tag{2.9}$$

$$C + (SiO_2) = SiC\,(s) + 2CO\,(g) \tag{2.10}$$

The equilibrium constant of Equation (2.9) is dependent on the activity of SiC, the activity of silicon and the activity of carbon as presented in Equation (2.11). Either there is a presence of SiC or there is no presence of SiC, thus the activity of SiC is either 1 or 0, and in a SiMn furnace unit activity of carbon is assumed. The wt.% silicon is dependent on the activity coefficient of silicon and the temperature dependent equilibrium constant as presented in Equation (2.12).

$$K = \frac{a_{SiC}}{a_{Si} \cdot a_C} \tag{2.11}$$

$$wt.\%Si = \frac{K}{\gamma_{Si}} \tag{2.12}$$

The amount of silicon that can form SiC is dependent on the temperature dependent equilibrium constant and the activity coefficient of silicon. The activity coefficient of silicon is depending on other pure elements in the SiMn melt such as manganese and iron. Since the formation of SiC is dependent on wt.% silicon in the alloy, it is also dependent on slag composition, metal composition and temperature as described in chapter Production of silicomanganese. The dissolving of carbon from the SiMn alloy to form graphite can be described by Equations (2.13) and (2.14). The activity coefficient of carbon in Equation (2.13) is dependent on other pure elements in the alloy such as silicon, manganese and iron.

$$\underline{C} = C_{gr} \tag{2.13}$$

$$wt.\%C = \frac{\gamma_C}{K} \tag{2.14}$$

The Gibbs phase rule is used to analyze a multiphase equilibrium and it is presented in Equation (2.15).

$$F = C - P + 2 - R \tag{2.15}$$

F is the number of degrees of freedom, C the number of components, P the number of phases and R the number of restrictions, such as $^{Mn}/_{Fe}$ ratio, temperature and pressure. The silicon content of the SiMn alloy can be determined at a given temperature when the phases liquid, gas, $^{SiC}/_{C_{gr}}$ is present and the ratio of iron and manganese is fixed as in Figure 2.4.

2.3.1 Formation and phases of SiC and graphite from previous experiments

Tuset & Sandvik (1970) established during solubility experiments of carbon and silicon in manganese alloys that SiC can form in a SiMn-alloy. They investigated the solubility of carbon in silicomanganese at 1330-1630°C where liquid samples were tapped from the crucible at different temperatures. The tapping was conducted with a bolt on the bottom of the crucible that allowed several tappings into a rotating sample holder during the experiment. Tuset & Sandvik (1970) found that the SiC particles were located in the central zone of the samples, and no SiC particles in the rim of the sample. This indicates that the SiC particles were formed during the solidification process. Tuset & Sandvik (1970) found that with silicon concentrations less than 20wt.% the dissolved carbon precipitated out as graphite flakes in the cross section of the sample.

Davidsen (2011) also found that SiC formed in a SiMn-alloy and much of the SiC formed in the metal was likely to be tapped together with the metal. The experiments conducted by Davidsen (2011) to investigate the reaction presented in Equation (2.9) that takes place in liquid alloy was done with a master SiMn-alloy in a vertical tube furnace. A master alloy consisting of 43.9g high carbon FeMn (HC FeMn) and 25g Si was heated in the furnace at 1600°C for 90 minutes with argon atmosphere. The furnace was then turned off, and the samples cooled rapidly the first 300°C. Figure 2.5 show a picture taken with an electron probe micro-analyzer (EPMA) of the HC FeMn and Si experiment. The SiC was found in the metal and not as a separate layer at the top. The whole sample had a similar distribution of $\beta-$SiC as presented in Figure 2.5. Davidsen (2012)

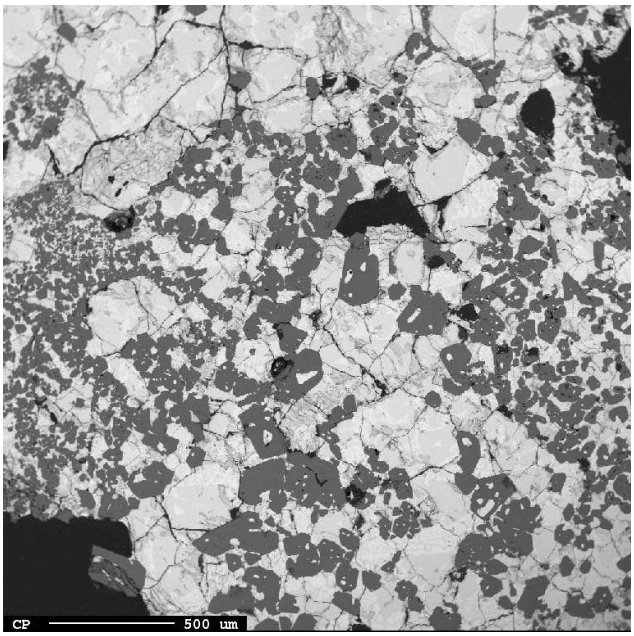

Figure 2.5: SiC formed in a HC FeMn and Si master alloy in experiment by Davidsen (2011). The gray phase is metal, while the dark gray phase is SiC.

Davidsen (2011) also did experiments with SiMn-alloy and a coke particle, and experiments with SiMn-slag and a coke particle. The SiC was formed on the coke particle interface and grew into the alloy/slag, and the formation rate increased with silicon content. The formation of SiC in the metal was faster than in the slag.

A summary of previous work with SiC and its polytypes is reviewed by Davidsen (2011) as presented in Table 2.3. It can be seen from Table 2.3 that temperature is a very important factor to determine what polytype of SiC is formed. Based on the reported data in Table 2.3 $\beta - SiC$ is the only phase of SiC under c. 1700°C, and both α- and $\beta - SiC$ can form above c. 1700°C which corresponds with Chase (1998). α- and $\beta - SiC$ can form through both precipitation in molten silicon, gas phase and react from SiO_2 and carbon.

Table 2.3: Summary of the different SiC types and how they were produced. The table is taken from Davidsen (2011), reviewed and modified. The information from the different systems are given by the following authors in descending order: Li et al. (2009), Krishnarao & Subrahmanya (1995), Zhou & Singh (1995), Nelson et al. (1966), Ivantsov & Dmitreiev (1998), Ciftja (2011*a*,*b*) and Davidsen (2011) based on information from Washington Mills. TM = transition metals.

System	Medium	T [°C]	Phase	Polytypes
$SiO+C$	gas	1300	β	3C
SiO_2+C	solid/gas	1300-1600	β	3C
$Si+Mo+C$	liquid	1430-1510	β	3C
$Si+C$	liquid	1500	β	3C
$Si+TM+C$	liquid	1700-1950	α,β	6H, 15R, 21R, 3C
$Si+O+C$	gas/liquid	≥ 2100	α,β	2H, 4H, 6H, 15R, 3C
SiO_2+C	solid/gas	≥ 2500	α	4H, 6H, 15R

Li et al. (2009) investigated the $SiO+C$ system and the formation of SiC nanowires from SiO(g). The reaction between SiO and carbon from pyrolyzed bamboo slices at 1300°C was reported to be β-SiC as presented in Table 2.3.

Krishnarao & Subrahmanya (1995) investigated the SiO_2+C system and the formation of SiC from rice husk silica and carbon black. The experiments were conducted in the temperature range of 1300-1600°C, with and without a CO- catalyst. With a CO catalyst β-SiC formed above 1400°C, and without the catalyst β-SiC formed above 1550°C.

Zhou & Singh (1995) investigated the $Si+Mo+C$ system and the formation of SiC particles in a silicon-molybdenum melt. The melt consisted of up to 10% Mo and the temperature ranged between 1430 and 1510°C. They found that β-SiC was formed under these conditions. Nelson et al. (1966) investigated a $Si-C_{sat}$ system and found that β-SiC formed in a melt at 1500°C.

2.3.2 Growth of SiC on carbon

SiC can form on carbon either through the reaction with silicon from the SiMn alloy or SiO_2 from the slag as presented in Equations (2.9) and (2.10) respectively. The reaction between the SiMn alloy and carbon will be presented here.

The thickness of the SiC layer depends on the how fast reactants are transported to the reaction interface. The simplified growth model of SiC on carbon particles mainly consists of four steps:

1. Transport of silicon from the bulk SiMn alloy to the carbon surface.
2. Transport of silicon from the metal phase through the SiC layer.
3. Transport of carbon from the carbon particle through the SiC layer.
4. Chemical reaction between silicon and carbon on the reaction interface.

Before a layer of SiC is formed, transport of carbon and silicon, step 2 and 3 can be neglected. After a SiC layer is formed, transport of either carbon or silicon through this layer is necessary for growth of the SiC layer. Step 4, the rate of chemical reaction at high temperatures is fast and thus not the rate determining step. The growth rate is determined by the solid state diffusion of the slowest species.

Hon et al. (1980) investigated the self diffusion of silicon in crystalline $\beta - SiC$ at temperatures between 2010°C and 2274°C. They found that the diffusion of carbon in SiC was c. two orders of magnitude bigger than the diffusion of silicon. This is in accordance with Davidsen (2011) that found that SiC grew from the $^{coke}/_{metal}$ interface into the SiMn alloy and thus diffusion of carbon through the SiC layer is larger than the diffusion of silicon. The rate of formation can be described by Equation (5.1), where r is the rate of the reaction, A is the area of the reaction interface, k is the reaction constant and $U_1 - U_2$ is the driving force of the reaction. The equilibrium composition is often used for U_2. The rate of reaction is dependent on the area of the reaction interface and is thus affected by surface tensions such as wetting between the reacting surfaces.

$$r = A \cdot k \cdot (U_1 - U_2) \tag{2.16}$$

2.3.3 Buoyancy

When SiC is formed in the liquid SiMn alloy it can be transported upwards in the system. According to Sandvik et al. (1999), this can be caused by density differences between SiC particles and the liquid SiMn alloy, viscosity and movements of the particle and the system.

If the density of the particle is lower than the density of the bulk alloy, the particle will rise. The speed of the particle is determined by a set of forces working on it. When laminar flow and spherical particles is assumed in the melt, the main forces is the buoyancy caused by the density differences and downward drag caused by gravity as presented in Figure 2.6.

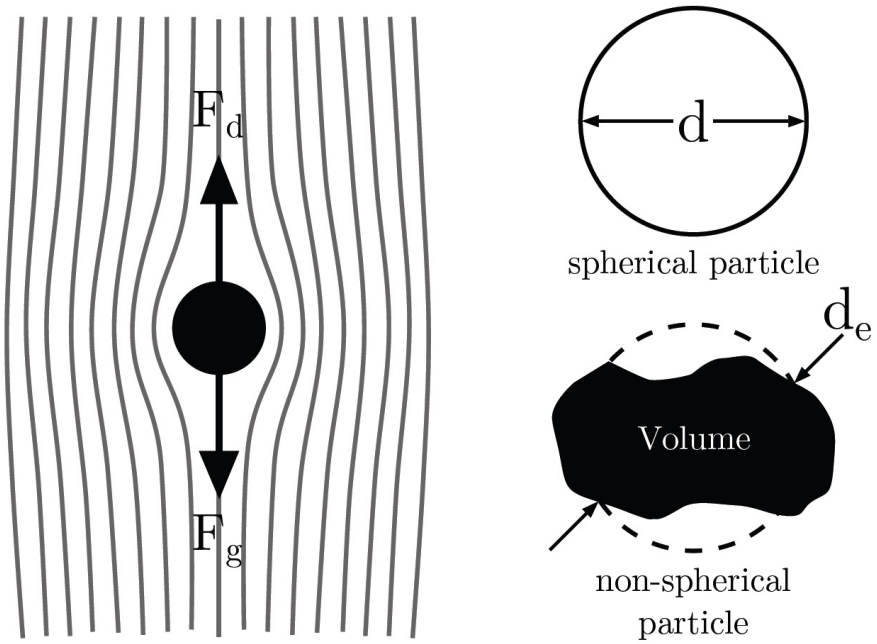

Figure 2.6: (a) Sketch of the forces working on a particle suspended in a liquid with laminar flow and (b) a spherical and non-spherical particle with equivalent diameter, d and d_e. Figure taken from Davidsen (2011).

The buoyancy of a small particle in a gravity field can be described by Equation (2.17). The resultant forces acting on the particle, F_r, is a function of particle size, gravity, the difference in densities of the fluid, the spherical particle.

$$F_R = \frac{\pi d^3}{6} \left(\rho_f - \rho_s\right) g \tag{2.17}$$

At a certain point there will be a balance between the outer forces affecting the particle and the frictional forces. When that happens the particle will obtain constant velocity, referred to as terminal velocity. Stoke's Equation gives this for laminar flow as presented in Equation (2.18).

$$F_{sphere} = \frac{24}{8 \cdot Re} \cdot \pi \cdot \rho \cdot f \cdot v^2 \cdot d^2 = 3\pi \cdot d \cdot v \cdot \mu \tag{2.18}$$

where Re is Reynold's number, v is the velocity and μ is the viscosity of the melt. By combining Equation (2.17) and (2.18) an expression of the terminal velocity of the particle is obtained as presented in Equation (2.19).

$$v_{stokes} = \frac{d^2 \cdot g \cdot \left(\rho_f - \rho_s\right)}{18\mu} \tag{2.19}$$

This can also be used for non-spherical particles with diameters under $100\mu m$. The equivalent diameter, d_e, as presented in Figure 2.6 can be calculated based on the particle volume according to Equation (2.20).

$$d_e = \sqrt[3]{\frac{6V}{\pi}} \tag{2.20}$$

where V is the particle volume. Equation (2.19) is then modified for non-spherical particles to Equation (2.21). This equation can be used to calculate the terminal velocity of SiC and graphite particles for particle diameters less than $100\mu m$.

$$v_{stokes\,d_e} = \frac{d_e^2 \cdot g \cdot \left(\rho_f - \rho_s\right)}{30\mu} \tag{2.21}$$

2.4 Nucleation

The formation of SiC and graphite in the Mn-Fe-Si-C system has been investigated in this thesis. It is important to understand the mechanics of nucleation and formation of interface structure to understand how SiC and graphite is formed in a SiMn alloy.

Nucleation is the first stage of solidification and it begins with some degree of undercooling. Increasing the undercooling, ΔT_n, increases the driving force of nucleation, ΔG, the nucleation rate, I, and the growth rate, V, of SiC dendrites. When this occurs the first fraction of solid, f_s, appears. The nucleation rate is more sensitive to temperature than the growth rate. (Kurtz & Fisher 1998, Cantor & Doherty 1979)

Nucleation is the dominant process at the start of solidification and establishes the final grain population, with each grain forming equiaxed grains. Homogeneous nucleation can occur when the undercooling gets large enough to cause a stable nucleus, but it rarely happens except in controlled laboratory experiments. Heterogeneous nucleation occurs at impurities and preexisting surfaces in the melt, i.e.: on a crucible wall that holds the liquid. (Kurtz & Fisher 1998, Askeland & Phulé 2006)

At atomic dimensions the interface of a crystal has a large curvature. The curvature lowers the equilibrium temperature so that the smaller the crystal size becomes, the lower is its melting point. The lower melting point occurs because the low curvature creates a large pressure difference between the two phases. The equilibrium melting point is thus lowered by ΔT_r and the critical size of the crystal, r°, can be calculated as shown in Equation (2.22). (Kurtz & Fisher 1998, Askeland & Phulé 2006)

$$r^o = \frac{2\Gamma}{\Delta T_r} = \frac{2\sigma}{\Delta T_r \Delta s_f} = \frac{2\sigma T_m}{\Delta H_f \Delta T} \tag{2.22}$$

Γ is the Gibbs-Thomson coefficient, σ is the solid/liquid interface energy, Δs_f is the entropy of fusion per unit volume, $T_{m,}$ is the equilibrium solidification temperature and ΔH_f is the latent heat of fusion. Equation (2.22) indicates that the smaller the undercooling between the melting point and the temperature of the melt, the larger the size of the equilibrium crystals. The nucleation of a spherical crystal with radius, r, is given by the number of atoms, each of volume V', and given by Equation (2.23). (Kurtz & Fisher 1998, Askeland & Phulé 2006)

$$n \cong \frac{4r^3\pi}{3V'} \tag{2.23}$$

The nucleation of a crystal depends on two processes: thermal fluctuations that creates various sized crystal embryos (clusters), and creation of an interface between the solid and liquid phase. The free energy change ΔG_v which is associated with the first process is described in Equation (2.24).

$$\Delta G = \Delta G_i + \Delta G_v = \Delta g \cdot v + \sigma A = \frac{4}{3}\pi r^3 \Delta G_v + 4\pi r^2 \sigma \tag{2.24}$$

Δg is the Gibbs free energy difference per unit volume. The volume free energy change ΔG_v is proportional to the volume transformed and thus the cube of the cluster radius. The surface free energy change, ΔG_i, is associated with creating an interface between the solid and liquid phase. ΔG_i is thus proportional to the area of solid/liquid interface formed, and thereby proportional to the square of the cluster radius. (Askeland & Phulé 2006, Kurtz & Fisher 1998, Ray 1993)

When a thermal fluctuation causes the cluster to become larger than r°, growth will occur because of the decrease in total free energy, ΔG as presented in Figure 2.7. Thus a crystal cluster becomes a nucleus.

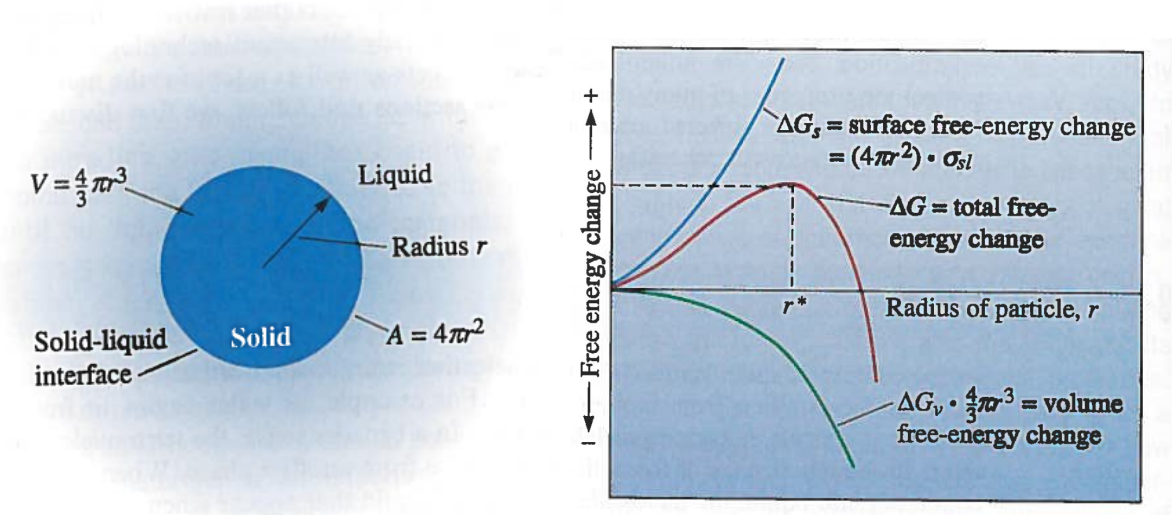

Figure 2.7: Free energy of a crystal cluster as a function of its radius. a) An interface is created when a solid forms from a liquid. (b) The total free energy of the solid-liquid system. The solid is a crystal cluster until it reaches r°,when it becomes a nucleus. Figures taken from Askeland & Phulé (2006).

The solid composition that is most likely to nucleate first is the one with the largest difference in free energy. The composition of the first nuclei formed is near the equilibrium composition at the liquidus temperature for small undercooling.(Thompson & Spaepen 1983, Ishihara et al. 1985)

The rate of nucleation is a function of temperature. When the temperature drops under the melting point of the material,T_m, (undercooling) the driving force of nucleation increases. The undercooling also causes atoms to be slower and that slows the nucleation process. Typically the rate of nucleation reaches a maximum or a critical temperature at some point below the transformation temperature.(Askeland & Phulé 2006, Kurtz & Fisher 1998)

2.5 Interface structure

When a nucleus is formed it starts to grow. The grain growth can be limited by either one or all of the following undercoolings of the melt:

- Kinetic undercooling, ΔT_k, due to atomic attachment at the interface, which is a local equilibrium.
- Curvature undercooling, ΔT_r due to curvature of the particles.
- Constitutional undercooling caused by diffusion of mass, ΔT_c.

- Thermal undercooling, ΔT_t.

The total undercooling can thus be described as $\Delta T = \Delta T_k + \Delta T_r + \Delta T_c + \Delta T_t$. (DiVenuti & Ando 1998, Löser & Herlach 1992)

Two different growth morphologies are presented in Figure 2.8. At the non-faceted surface presented in Figure 2.8a, atoms can be added at any point of the surface and the shape of the crystal is dictated by capillarity action, diffusion of heat and/or mass. Slightly anisotropic properties such as interface energy leads to growth of dendrite arms. Faceted materials, presented in Figure 2.8b often have complex crystal structures and form planar angular surfaces. (Kurtz & Fisher 1998)

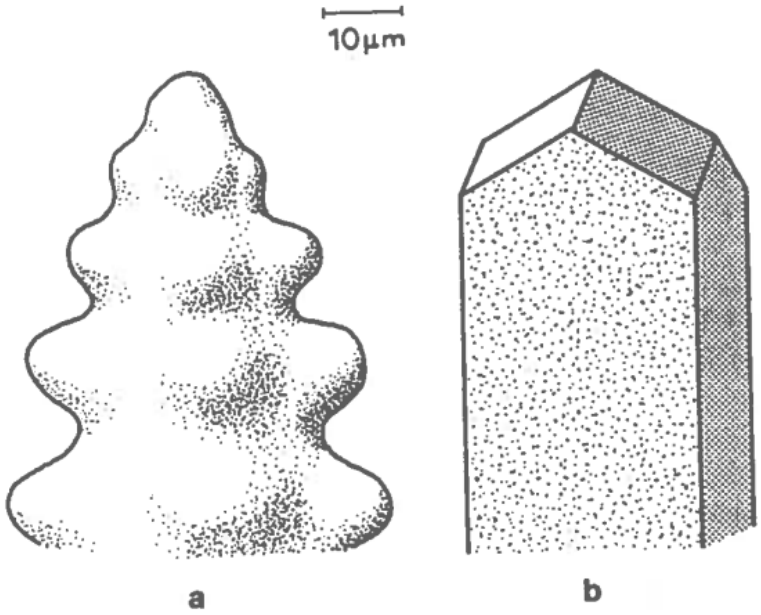

Figure 2.8: (a) Non-faceted and (b) faceted growth morphologies. Figure from Kurtz & Fisher (1998)

The faceted growth is usually into a well-inoculated liquid. A faceted solid/liquid interface is jagged at the microscope scale, but smooth at the atomic scale as presented in Figure 2.9a. Grain growth is determined by the probability that an atom will reach the interface and remain there until it has been fully absorbed by the crystal. The probability increases with increasing number of atoms to the crystal. At an atomically flat solid/liquid interface there will be few bonds to atoms from diffusion through the liquid. This causes the crystal to close its gaps in the interface at atomic scale. This results in a crystal that is faceted at microscopic scale and often exhibit high kinetic undercooling.

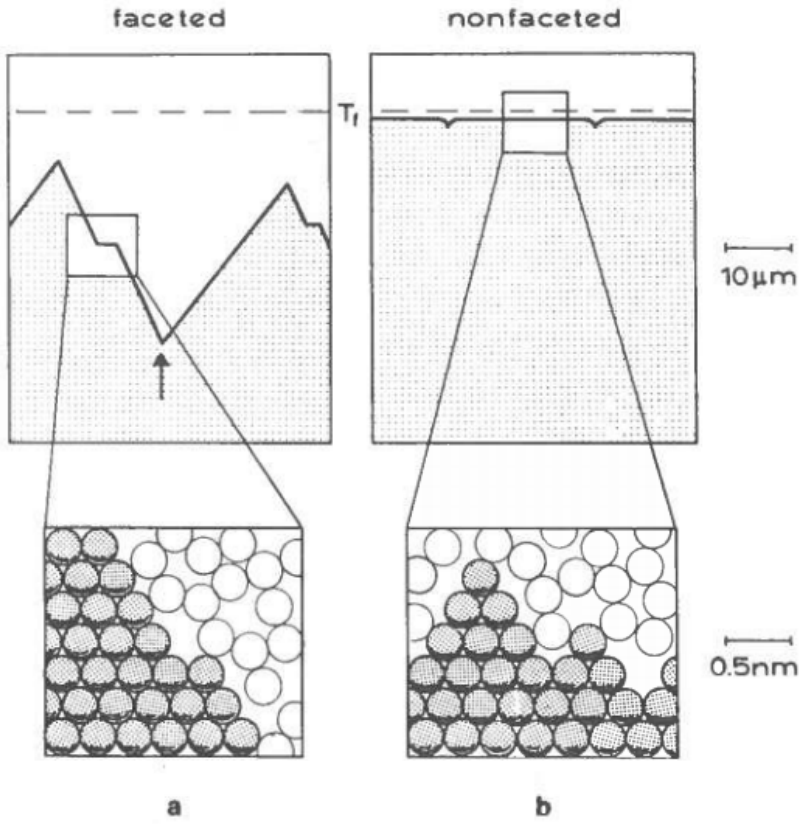

Figure 2.9: (a) Faceted and (b) non-faceted solid/liquid interfaces. Figure is taken from Kurtz & Fisher (1998)

The non-faceted growth happens into a poor inoculated liquid. The non-faceted solid/liquid interface presented in Figure 2.9b can be microscopically flat, but the atomic scale can be rough and uneven. This causes new atoms to attach easily, independent of crystal orientation. Thus the dendritic growth is non-faceted at the microscopic scale and exhibit low kinetic undercooling (Askeland & Phulé 2006, Kurtz & Fisher 1998)

The greater the difference in structure and bonding between the solid and the liquid phases results in fewer newly arriving atoms into the crystal and thus a faceted microstructure. Metals have a similar density, structure and bonding in solid and liquid states, thus the transition from liquid to solid is gradual and the interface becomes non-faceted. The melting entropy can be used to predict the morphology of the material as presented in Equation (2.25).

$$\alpha = \frac{\Delta S_f}{R} \tag{2.25}$$

α is the dimensionless entropy, ΔS_f is the melting entropy for the material in question and R is the gas constant. When the values of α is below ~ 2 it implies a tendency to non-faceted growth.

Values of α above 2 implies that faceted growth will occur. $\beta - SiC$ have a α value of 2.0, and it is expected to have a faceted growth, but non-faceted growth can occur.

Graphite, which is faceted, grows in different rate in different directions. Graphite often have morphology called "flakes", but can also have spheroidal morphology as presented in Figure 2.10.(Gruzleski 1975, Kurtz & Fisher 1998)

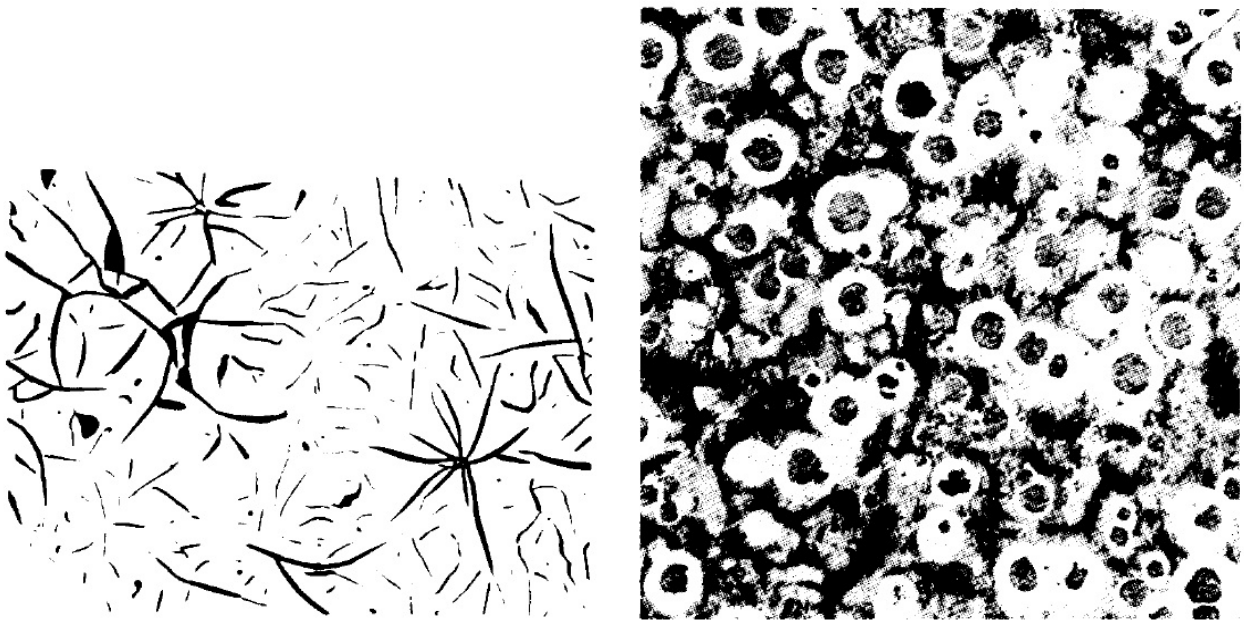

(a) **(b)**

Figure 2.10: (a) Flake graphite and (b) spheroidal graphite in cast iron. In (a) the the black rods are graphite and in (b) the black spheres inside the white iron matrix are graphite. Figures taken from Gruzleski (1975)

Chapter 3

Experimental

In this chapter the experiment conducted, raw materials used and analyses method in this thesis will be presented. The experiments were done in a vertical tube furnace, where three manganese alloys were exposed to cyclic temperature change. The goal was to look at the kinetics of formation of SiC in SiMn-metal, and investigate the grain size and quantify amount of silicon carbide and graphite formed.

It was assumed that carbon from the crucible could dissolved in the liquid alloy at c. 1610°C and thus reach equilibrium between carbon and silicon in the alloy. When the temperature was lowered slowly to 1290°C the equilibrium between carbon and silicon would change in accordance with Figure 2.4. Thus the carbon above the equilibrium at 1290°C would form graphite or SiC depending on the silicon amount in the alloy. When this was repeated in temperature cycles it could be expected that equilibrium between carbon and silicon was reached at c. 1610°C and thus graphite would accumulate. At the higher cycles, carbon could be dissolved from the crucible or from previously formed SiC or graphite to reach a equilibrium at 1610°C. When SiC is formed it can be expected that a layer of SiC is formed at the crucible wall, thus stopping the dissolving of carbon from the crucible into the liquid alloy. It can thus be expected a slower rate of formation of SiC in the experiments with LC SiMn compared with rate of formation of graphite in the HC and std. SiMn experiments.

3.1 Raw materials

The raw materials used in the experiments were std. SiMn and LC SiMn supplied and analyzed by Eramet Norway AS, HC SiMn supplied by Vale Manganese Norway AS and analysed by Mo Lab AS. The chemical composition of HC, std. and LC SiMn is presented in Table 3.1.

Table 3.1: Composition of HC, std. and LC SiMn in weight percent. Std. and LC SiMn is supplied from Eramet Norway AS, while the HC SiMn is supplied from Vale Manganese Norway AS.

Compound	HC SiMn	Std. SiMn	LC SiMn
Mn	65.5	68.8	60.7
Si	16.4	19.0	29.1
C	2.47	1.66	0.24
Fe	14.0	10.8	8.9
Oxygen	1.0	3.2	0.23

3.2 Vertical tube furnace

The vertical tube furnace supplies heat by a resistance graphite element and is presented in Figure 3.1. The experiments conducted in the graphite thermogravimetric heat resistance furnace reached a holding temperature at c.1610°C at a heating rate of $18^{\circ}C/_{min}$ as shown in Figure 3.2. Argon atmosphere was used.

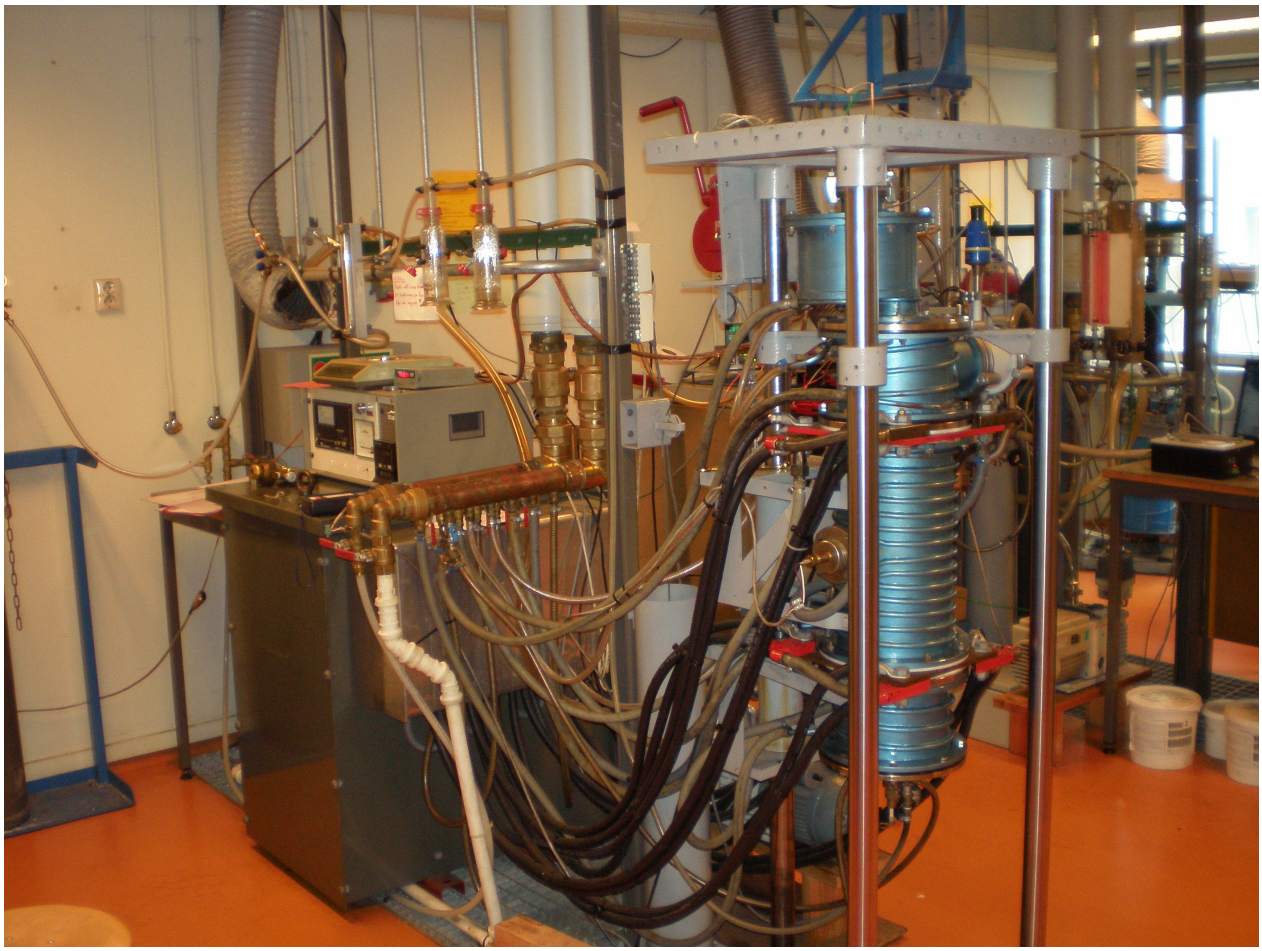

Figure 3.1: Graphite thermogravimetric heat resistance furnace used in the experiments.

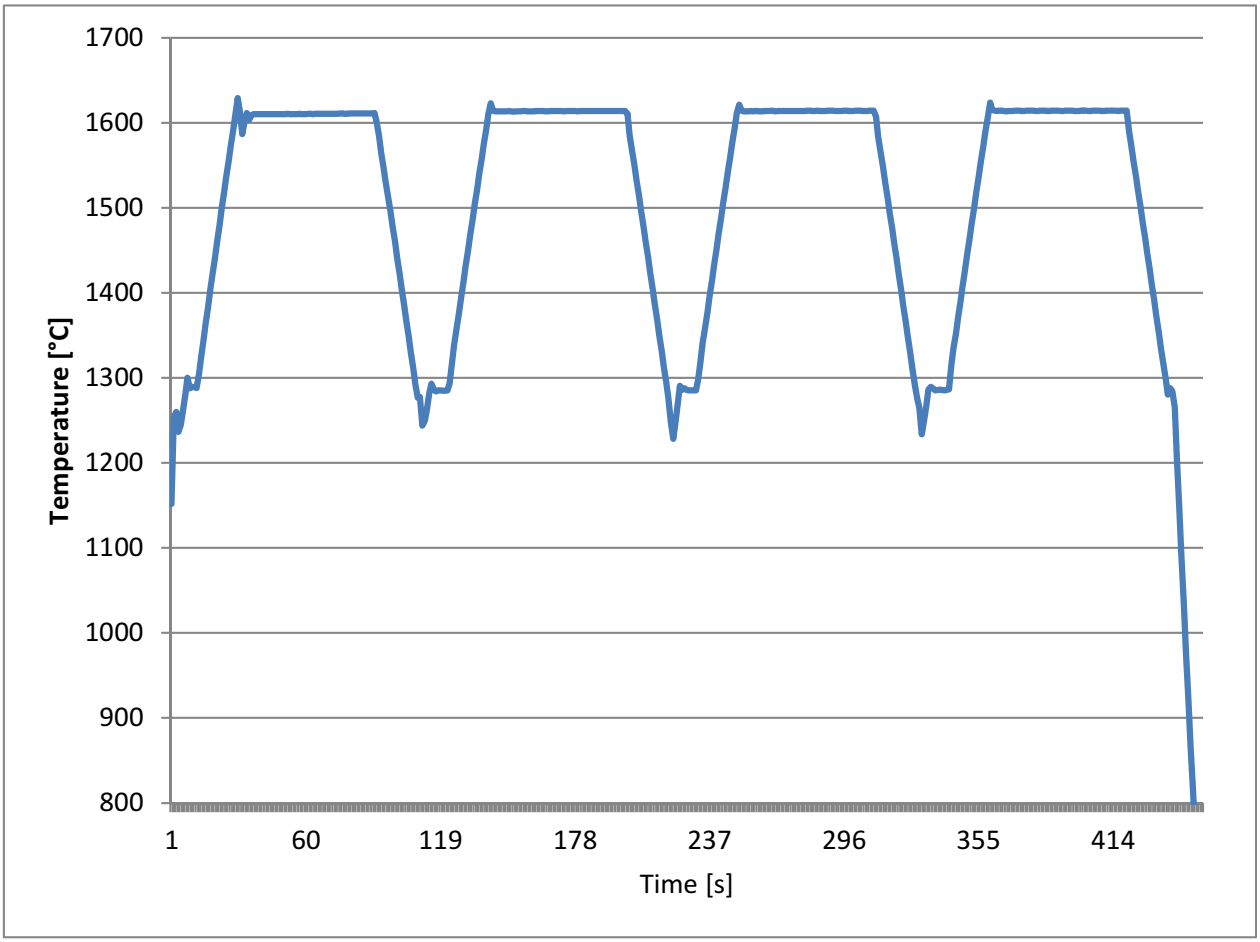

Figure 3.2: Cyclic temperature changes conducted with specimen 3. The temperature range of interest is between 1300°C and 1610°C. The heating and cooling rate from 1290°C to 1610°C was $18^{\circ C}/_{min}$.

3.2.1 Experimental setup

The furnace used is presented in Figure 3.1 and a schematic drawing in Figure 3.3. A temperature profile of the furnace was conducted and the bottom of the crucible was placed in the homogenous temperature range of the furnace as presented in Figure 3.4.

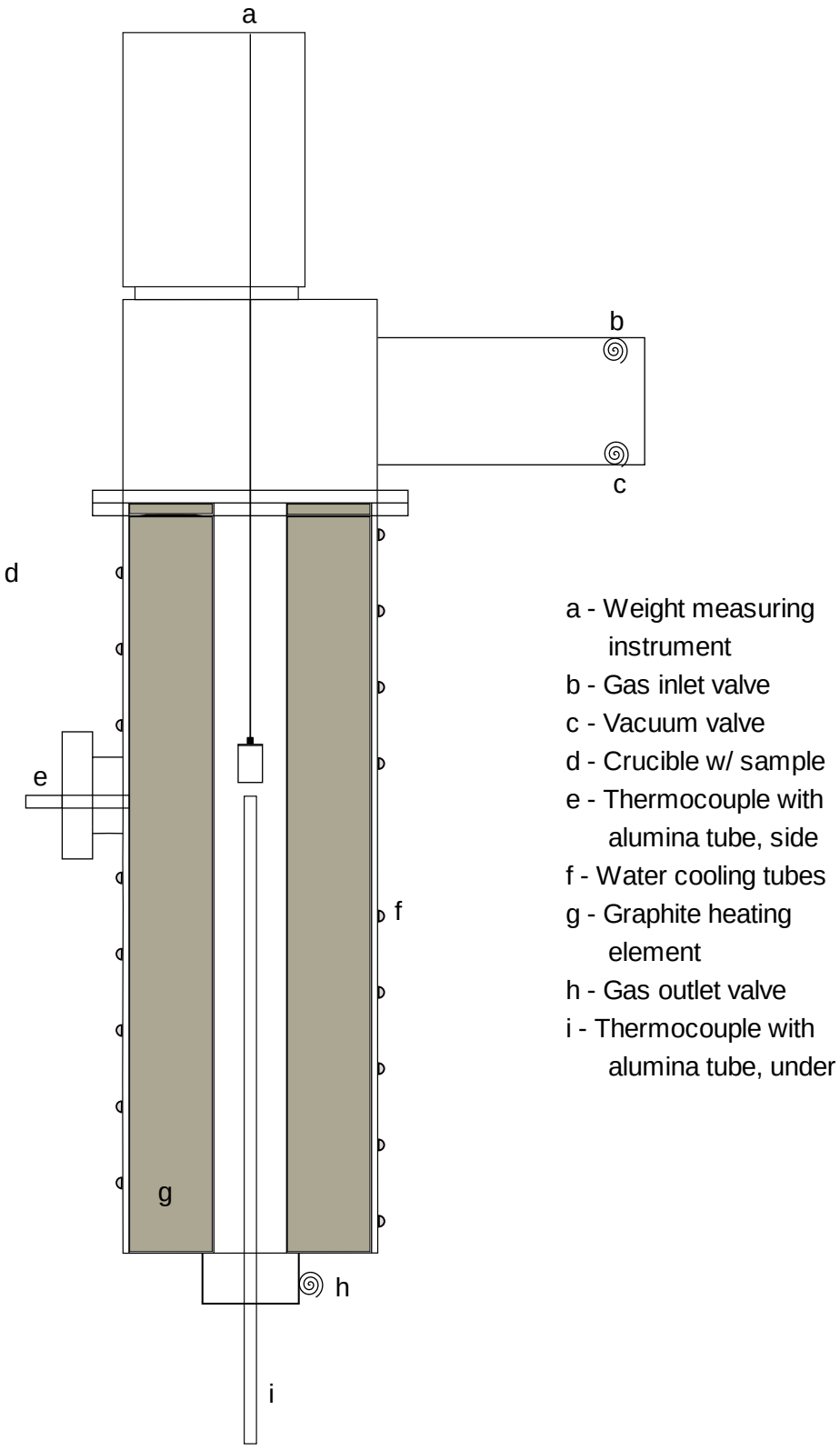

Figure 3.3: Schematic drawing of the vertical tube furnace used in the experiments.

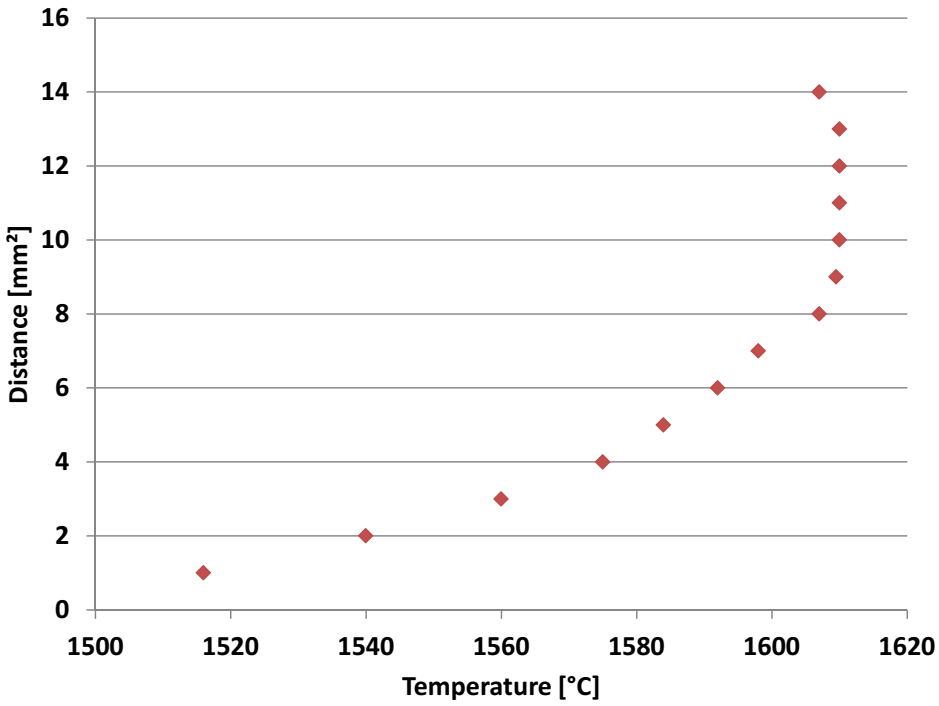

Figure 3.4: Temperature profile of the vertical tube furnace used in the experiments. The homogenous temperature range is the vertical line of measuring points at c. 1610°C.

The crucibles used in the experiment were 36mm wide and 70mm long. The crucible had threads in the top and matching lids. The lids had three holes to ensure free gas flow in and out of the crucible, and one threaded hole to hang it in the furnace as illustrated in Figure 3.5. The datasheet of the crucible material, IG-15 is presented in Appendix B.

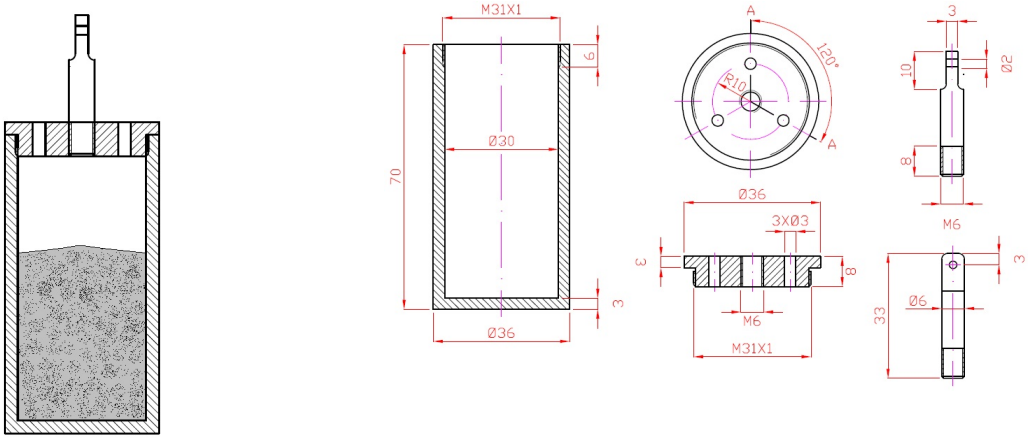

(a) (b)

Figure 3.5: The crucible used for the experiments. (a) is an illustrative drawing of the crucible with metal and (b) technical schematics with crucible dimensions. (Alstad 2011)

3.2.2 Sample preparation and experimental parameters

The HC and std. SiMn was crushed to -5mm size with a mortar and pestle, while the LC SiMn raw material was delivered as industrial fines. The crucibles were filled with 100g of the selected alloy. All experiments were in Argon 4.0 gas atmosphere, with a gas flow of c. 4 dm^3/min. Argon 4.0 had a purity of minimum 99.99 % Ar.

The specimen presented in Table 3.2 were heated in cycles as presented in Figure 3.2. The temperature cycles ranged from 1290°C to 1610±2°C and back down to 1290°C. The heating rates was $18^{\circ}C/min$, and the heating from 1300°C to 1610°C took c.17 minutes. This was repeated for the cooling from 1610°C to 1300°C. The holding time at 1610°C was 1 hour. For the experiments with 4 cycles the holding time below at 1290°C was 15 minutes. The cooling from 1290°C to room temperature was approximately $80^{\circ}C/min$.

Table 3.2: LC, std., and HC SiMn was underwent cyclic heat treatment in 9 experiments. The respective alloys with their wt.% silicon and carbon were heated to 1610°C in cycles as presented in the table.

Sample number	Alloy	wt.%*Si*	wt.%*C*	#Cycles
1	LC SiMn	29.1	0.24	1
2				2
3				4
4	Std. SiMn	19.0	1.66	1
5				2
6				4
7	HC SiMn	16.4	2.47	1
8				2
9				4

After the samples was cooled down, a vertical cross sections of the crucible was cut as presented in Figure 3.6, where one part was casted with epoxy to be analysed and the other was cut into horizontal cross sections at the top, middle and bottom of the crucible. This was done to ensure that any anisotropic behavior in the samples would be detected. Both the vertical and horizontal cross sections of the samples was analysed.

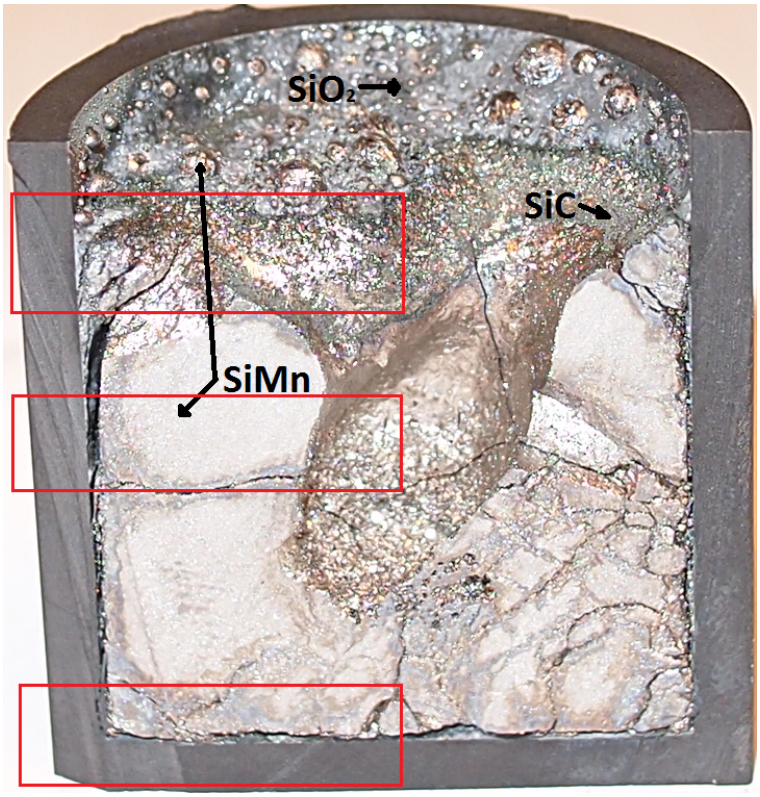

Figure 3.6: Cross section of sample 1. Samples were cut from the top, bulk and bottom of the cross section.

3.3 Analyses of the samples

There was conducted grid analyses of samples 1-3 and picture analyses of sample 4-9. The grid analyses was conducted with a optical light microscope as described in Grid analyses. The picture analyses was conducted due to graphite being difficult to differentiate from dimples and pores in samples 4-9 due to its low atomic number. Previous experiments with formation of SiC by Einan (2011) shows that grid analyses and picture analyses have a good correlevance. All samples were continuously analysed with Energy-dispersive X-ray spectroscopy (EDS) in a scanning electron microscope (SEM) to determine phases in each sample. The EDS results are presented in the results chapter.

3.3.1 Grid analyses

The area of SiC can be determined with a grid count of the samples. The grid counting is done with a transparent grid in the optical light microscope presented in Figure 3.7. Each time a injunction in the grid is on top of a SiC particle or the metal phase the point is registered. This way it is possible

to register the fractions of SiC and metal phase in the samples. There were taken c.500 counts of injunction points in each area of the sample, ie. top, bulk and bottom of the crucible. (Einan 2011)

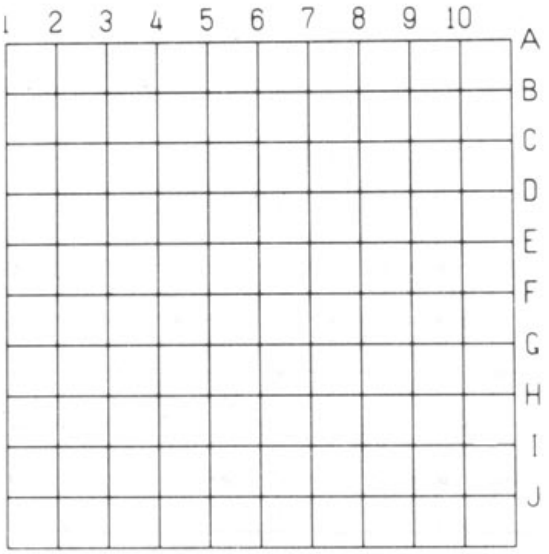

Figure 3.7: A grid counting tool in the light microscope. Each time a injunction is above a SiC or alloy particle, it is registered. Figure taken from Fullham (2012).

When looking at the cross section of the samples, the further from the middle of the crucible, the larger is the fraction this area represent. Thus during the grid analyses this had to be compensated for. A practical way of doing this was to "cut" the radius of the crucible into 3 equally large sections, thus representing 3 areas in the cylinder as presented Figure 3.8 and in Equations (3.1), (3.2) and (3.3). The area A_1 is closest to the center of the crucible, A_2 in the middle and A_3 closest to the crucible wall. The fraction of SiC is thus obtained in each section of the samples, and total amount of SiC can be calculated. This compensation was used when registering SiC particle fractions in sample 1-3 and graphite particle fractions in sample 4-9.

$$A_1 = \pi \cdot \left(\frac{r}{3}\right)^2 \tag{3.1}$$

$$A_2 = \pi \cdot \left(\frac{2 \cdot r}{3}\right)^2 - A_1 \tag{3.2}$$

$$A_3 = \pi \cdot r^2 - (A_1 + A_2) \tag{3.3}$$

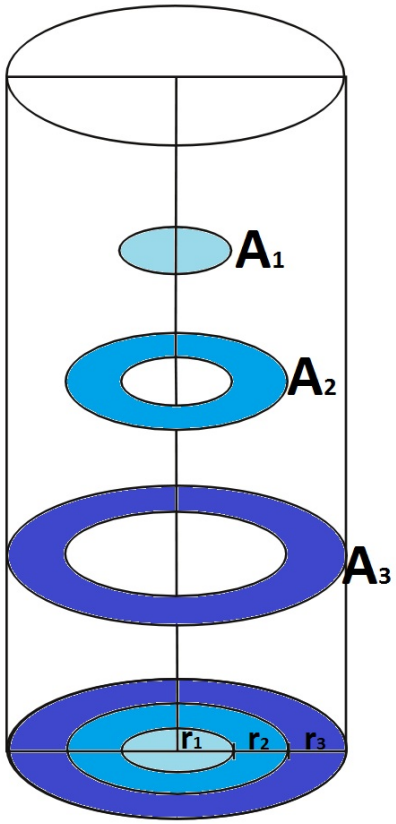

Figure 3.8: Compensation for cross section analysis. Finding the $^{SiC}/_{alloy}$- and $^{graphite}/_{alloy}$ fractions with a compensation of the geometry of the cylindrical crucible.

The size of SiC grains was measured with a measuring tool in the light microscope and the areal was calculated. An example of this is presented in Table 3.3. It was found appropriate to divide the SiC grains into two groups:

1. Angular grains.
2. Dendrites and clusters of dendrites with angular grains.

Table 3.3: Angular SiC particles in sample 3, LC SiMn with 4 temperature cycles.

Length $[mm]$	Width $[mm]$	Area $[mm^2]$
0.25	0.27	0.068
0.20	0.25	0.050
0.30	0.34	0.10
0.30	0.30	0.090
0.12	0.14	0.017
0.26	0.28	0.073
	Average :	0.067

3.3.2 Picture analyses

Pictures of samples 4-9 was taken in SEM (LVFESEM, Zeiss Supra, 55VP). Overlapping pictures from the crucible wall to the middle of the cross section of the top, bulk and bottom of the samples were taken. They were analysed in Adobe Photoshop CS5.1 were the area of graphite and total area of the samples could be compared as presented in Figure 3.9. The program counts amount of pixels total in the picture as presented in Figure 3.9a and amount of pixels inside the marked graphite area as presented in Figure 3.9b. The fraction of graphite is thus obtained in each picture, and total amount of graphite can be calculated. The area of each graphite grain was measured in Adobe Photoshop CS5.1 with an area measurement tool, and average graphite grain size in each sample was calculated.

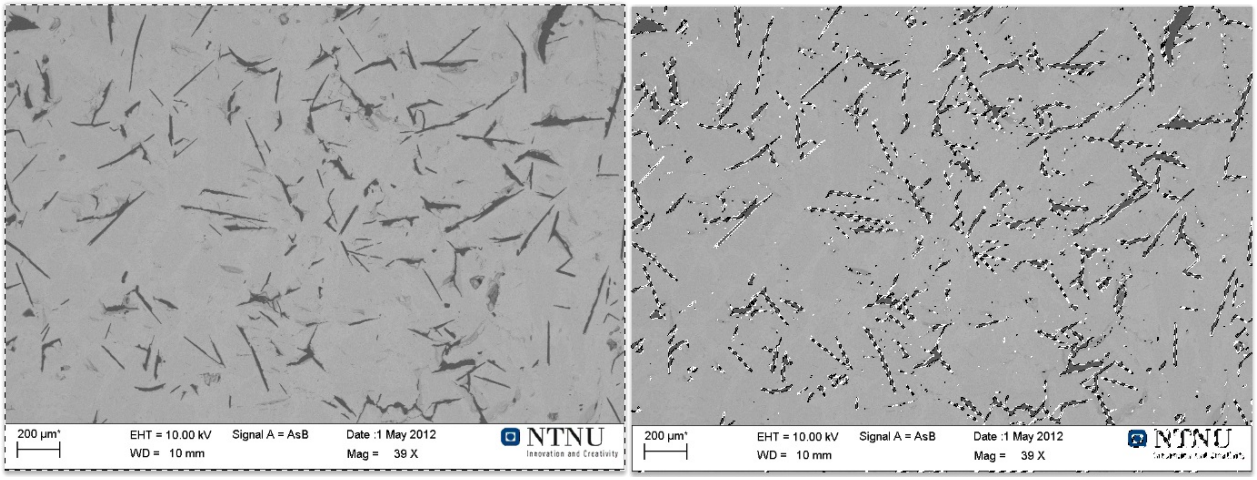

(a) **(b)**

Figure 3.9: Picture from bulk of sample 6. When the entire picture (a) is selected, 706560 pixels are counted. In picture (b) the area of graphite is selected and 48101 pixels are counted. Thus the fraction graphite in this picture is 6.8%. The information labels on the pictures are removed when the picture analyses are conducted. The area of each graphite grain on the picture was also measured with the program.

3.3.3 Distribution of carbon

After the volume fraction of $^{SiC}/_{alloy}$ and $^{graphite}/_{alloy}$ was found in the, the amount of carbon in the form of SiC or graphite was calculated. Amount of carbon as SiC, $m_{C_{SiC}}$ in samples 1-3 was calculated with Equation (3.4), and amount of carbon as graphite, $m_{C_{graphite}}$ in samples 4-9 was calculated with Equation (3.5). $X_{SiC/graphite}$ was amount of SiC or graphite found in each sample. The solidified alloy was c. 3cm high in the crucible, thus resulting in a estimated alloy volume, V_{alloy} of c. $21cm^3$. ρ is the density of the material in question, Mw is the molecular weight of silicon and carbon. An example of the calculation of amount of carbon in sample 1 is presented in Equation (3.6).

$$m_{C_{SiC}} = \frac{X_{SiC} \cdot V_{alloy} \cdot \rho_{SiC} \cdot Mw_C}{(Mw_{Si} + Mw_C)} \tag{3.4}$$

$$m_{C_{graphite}} = X_{graphite} \cdot \rho_{graphite} \tag{3.5}$$

$$m_{C_{Sample\,1}} = \frac{0.34\% \cdot 21cm^3 \cdot 3.21g/cm^3 \cdot 12.01g/mol}{(28.08 + 12.01)\,g/mol} = 0.07g \tag{3.6}$$

Chapter 4

Results

It was conducted experiments on 3 different SiMn alloys. Results from these 3 alloys, LC SiMn, std. SiMn and HC SiMn are presented in the following chapters. In each section in the results chapter the following will be presented:

- Amounts of $^{SiC}/_{graphite}$ formed and the average grain size.
- Calculations on distribution of carbon in the samples and dissolved carbon from the crucibles.
- Macrostructure pictures of each experiment.
- Microstructure pictures of the top, bulk and bottom of each sample.
- Quantification of the different phases, including SiMn alloy, graphite and SiC.

The microscope pictures presented in the results chapter are enlarged and presented in Appendix A.

4.1 LC SiMn

Measured volume fraction from analyses of LC SiMn with 29.1 wt.% Si and 0.24 wt.% C is presented in Table 4.1. Sample 1 was heated to 1610$\pm$2°C once, sample 2 twice and sample 3 was heated to 1610$\pm$2°C 4 times as described in section 3.2.2. The results from samples 1-3 presented in Table 4.1 shows that heating the LC SiMn samples to 1610$\pm$2°C formed 3 times the SiC with 4 cycles compared to 1 cycle, and the average SiC grain size and calculated amount of carbon in the form of SiC is also presented. The distribution of SiC grain size has been divided into two groups as described in Grid analyses and is presented in Figure 4.1. The equilibrium composition does not change significantly due to the reacted silicon from the alloy to SiC. There was conducted a reference experiment of sample 3, but not of sample 1 and 2.

Table 4.1: LC SiMn analysed with grid count and volume % SiC was measured. The average SiC grain size was measured, m_{SiC} is the calculated weight of SiC and $m_{C_{SiC}}$ is the calculated amount of carbon in the form of SiC.

Sample #	# cycles	vol.% SiC	m_{SiC} $[g]$	$m_{C_{SiC}}$ $[g]$	SiC grain size $[mm^2]$
1	1	0.34	0.23	0.07	0.015
2	2	0.86	0.59	0.18	0.033
3a	4	1.11	0.76	0.23	0.43
3b	4	1.30	0.88	0.27	0.41

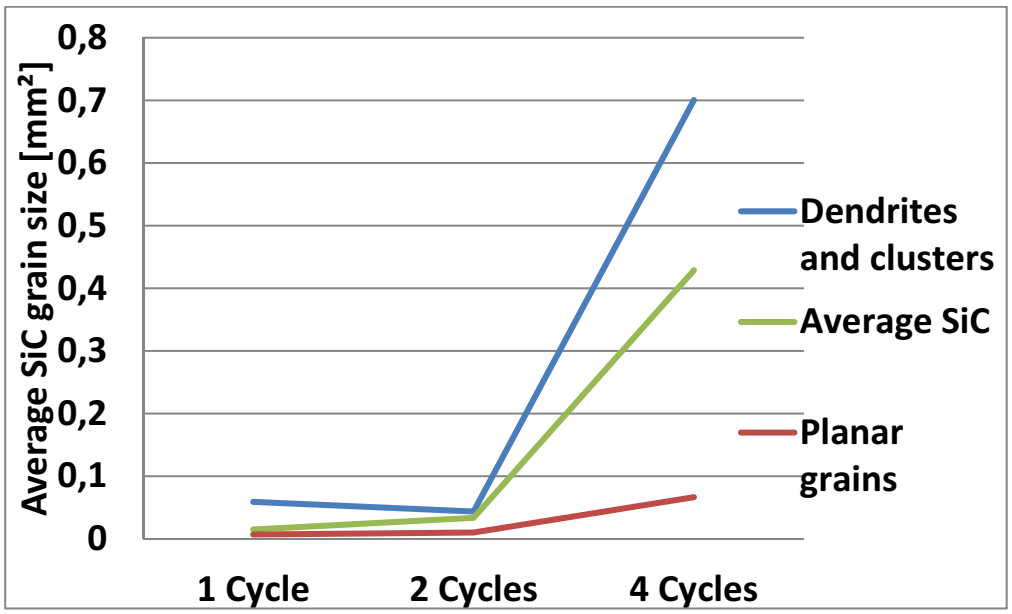

Figure 4.1: Average SiC grain size of angular grains, dendrites and clusters of angular grains. A total average SiC grain size is included in the figure.

The macroscopic pictures of sample 1-3 are presented in Figure 4.2. Above 90% of SiC found in samples 1-3 was found on top of the samples. The bulk of the samples were free of SiC, and less than 10% of the SiC found was in the bottom of the samples. In sample 2 there was partly a layer of SiC on the crucible wall with thickness ranging from $1\mu m$ to $60\mu m$. In sample 3 there was signs of the same layer of SiC, but c.80% of the crucible wall was free from SiC. The samples are separated by a gap from the crucible wall and are quite brittle in the zones with SiC is present.

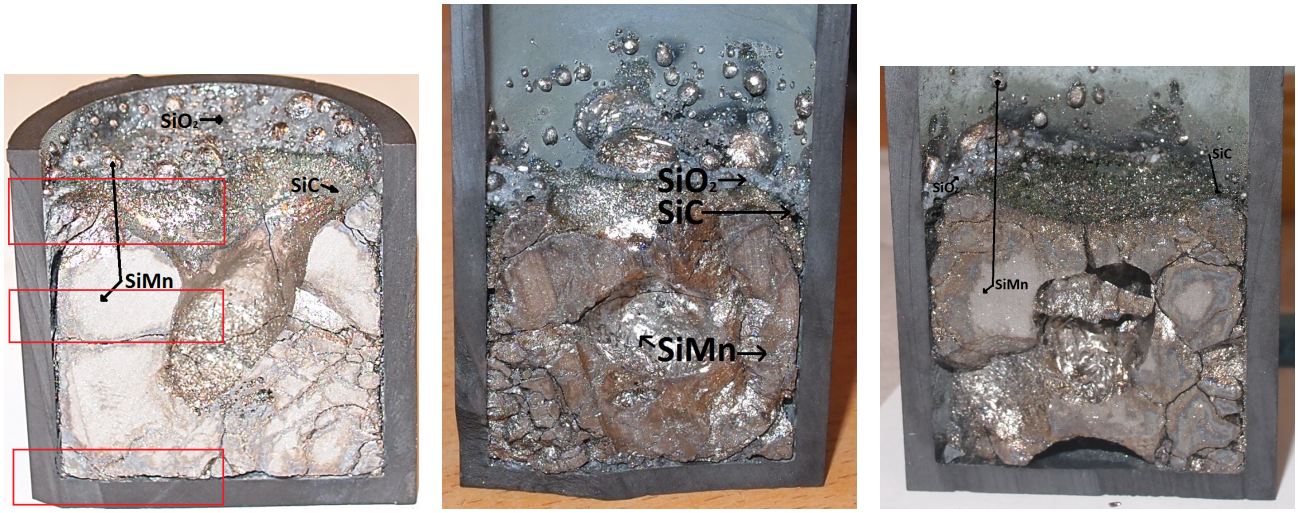

(a) LC SiMn, 1 cycle **(b)** LC SiMn, 2 cycles **(c)** LC SiMn, 4 cycles

Figure 4.2: Macroscopic picture of (a) sample 1 with 1 temperature cycle, (b) sample 2 with 2 temperature cycles and (c) sample 3a with 4 temperature cycles.

In Figures 4.3, 4.4 and 4.5 SEM pictures of the top, bulk and bottom of sample 1-3 are presented.

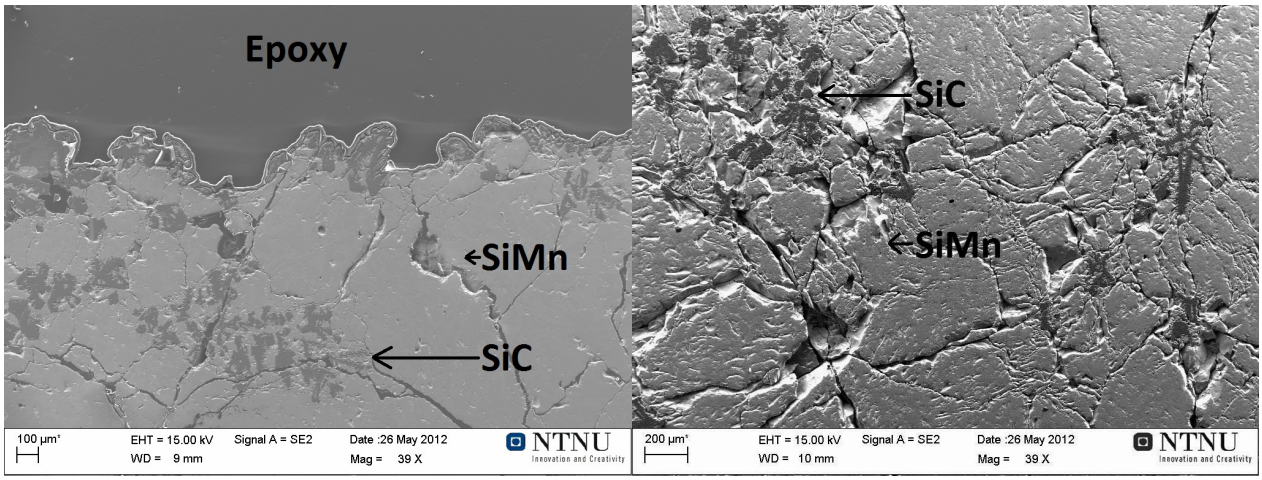

(a) 1 cycles, top of sample 1

(b) 2 cycles, top of sample 2

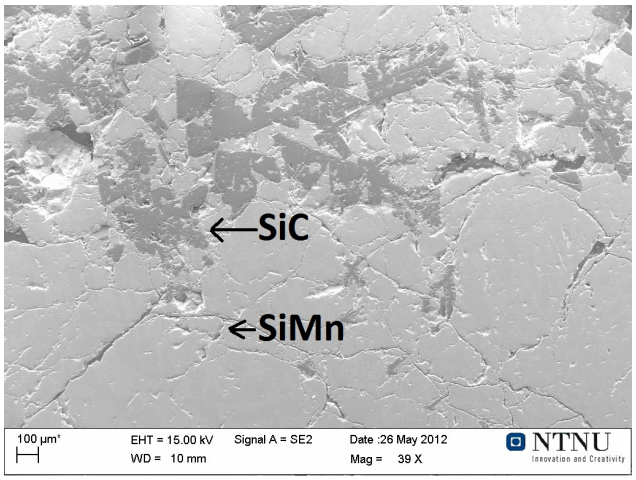

(c) 4 cycles, top of sample 3a

Figure 4.3: (a-c) Pictures of the top of sample 1-3 taken in the SEM.

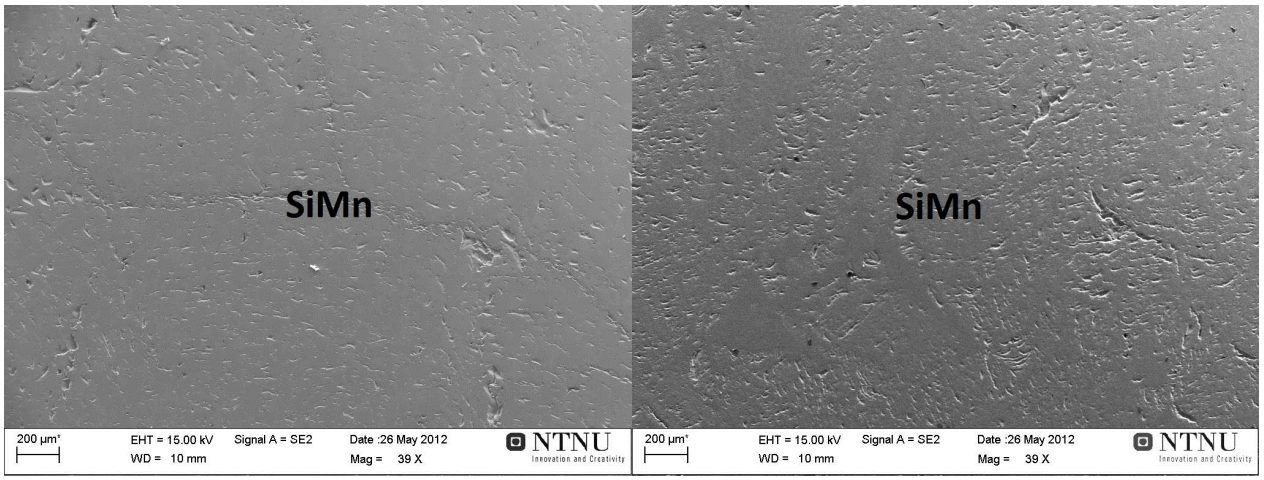

(a) 1 cycles, bulk of sample 1 **(b)** 2 cycles, bulk of sample 2

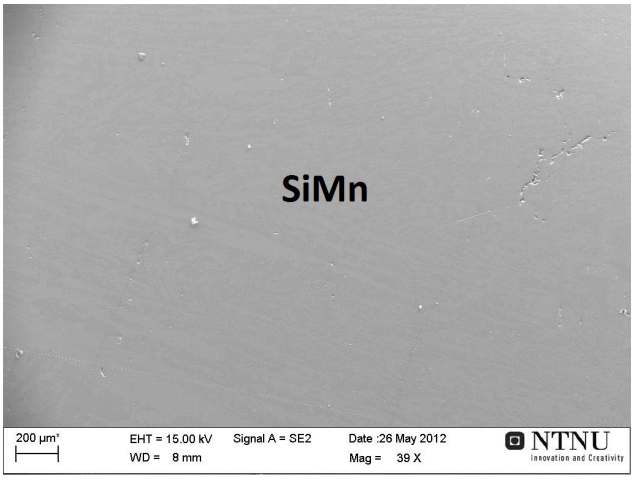

(c) 4 cycles, bulk of sample 3

Figure 4.4: (a-c) Pictures of the bulk of sample 1-3 taken in the SEM.

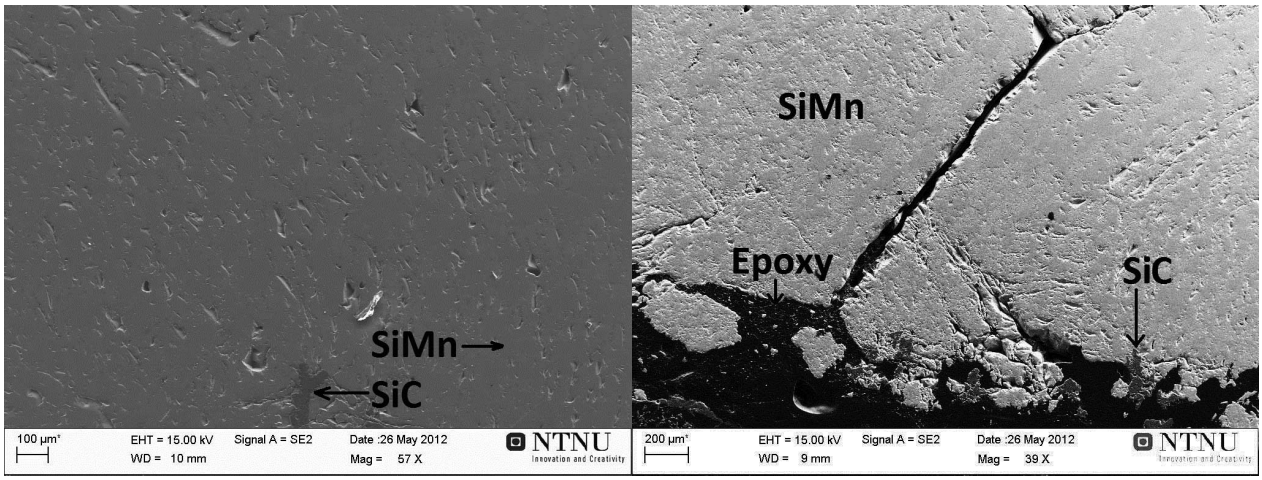

(a) 1 cycles, bottom of sample 1

(b) 2 cycles, bottom of sample 2

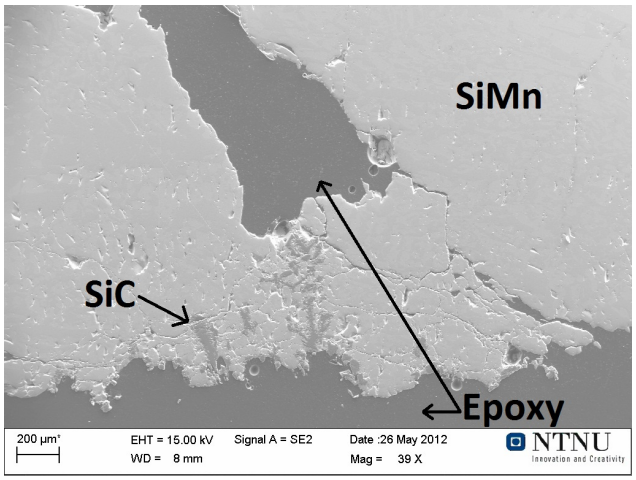

(c) 4 cycles, bottom of sample 3a

Figure 4.5: (a-c) Pictures of the bottom of sample 1-3 taken in the SEM.

Pictures of SiC particles taken in the SEM are compared in Figure 4.6. It can be seen that with one temperature cycle mostly planar, angular SiC particles was formed, while with 4 temperature cycles SiC dendrites was formed as well as planar angular SiC particles. After 2 cycles both dendrites and angular SiC particles was formed.

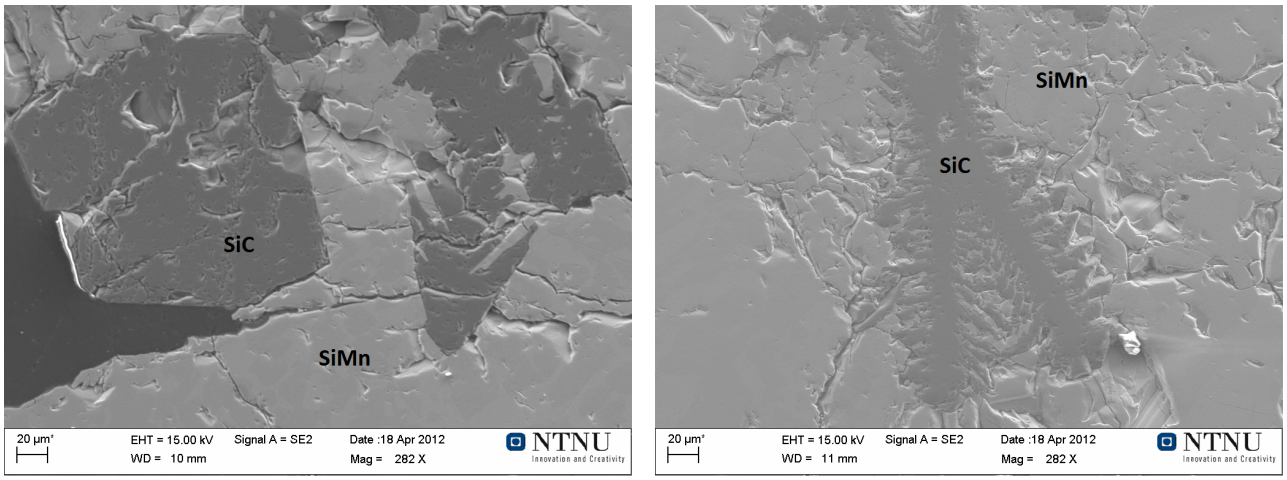

(a) **(b)**

Figure 4.6: Pictures taken in SEM from top of (a) sample 1 with 1 temperature cycle and (b) sample 3a with 4 temperature cycles. Both pictures taken from cross section of their respective samples.

In sample 3 there was clusters of SiC dendrites and planar grains as presented in Figure 4.7. It is is taken from the top of sample 3a and 96% of SiC found in sample 3a was at the top. Most of the planar grains have dendrites growing out of them, and grows to a cluster of SiC with SiMn-metal as an intermediate phase. It is difficult to observe where one SiC particle stops and the next starts. The largest cluster of SiC planar/dendritic grains with intermediate SiMn-metal is c. $3.3mm^2$, while the average size of the clusters is c.$0.7mm^2$. The planar grains that is not in a coherent cluster have an average size of c.$0.07mm^2$.

In Figure 4.7, to the left it can be observed a coherent cluster of dendritic SiC without any planar grains. The size of this cluster of SiC dendrites with intermediate SiMn-metal is c.$1mm^2$. To the right in Figure 4.7 it can be observed a coherent cluster of planar SiC grains and some dendritic SiC.

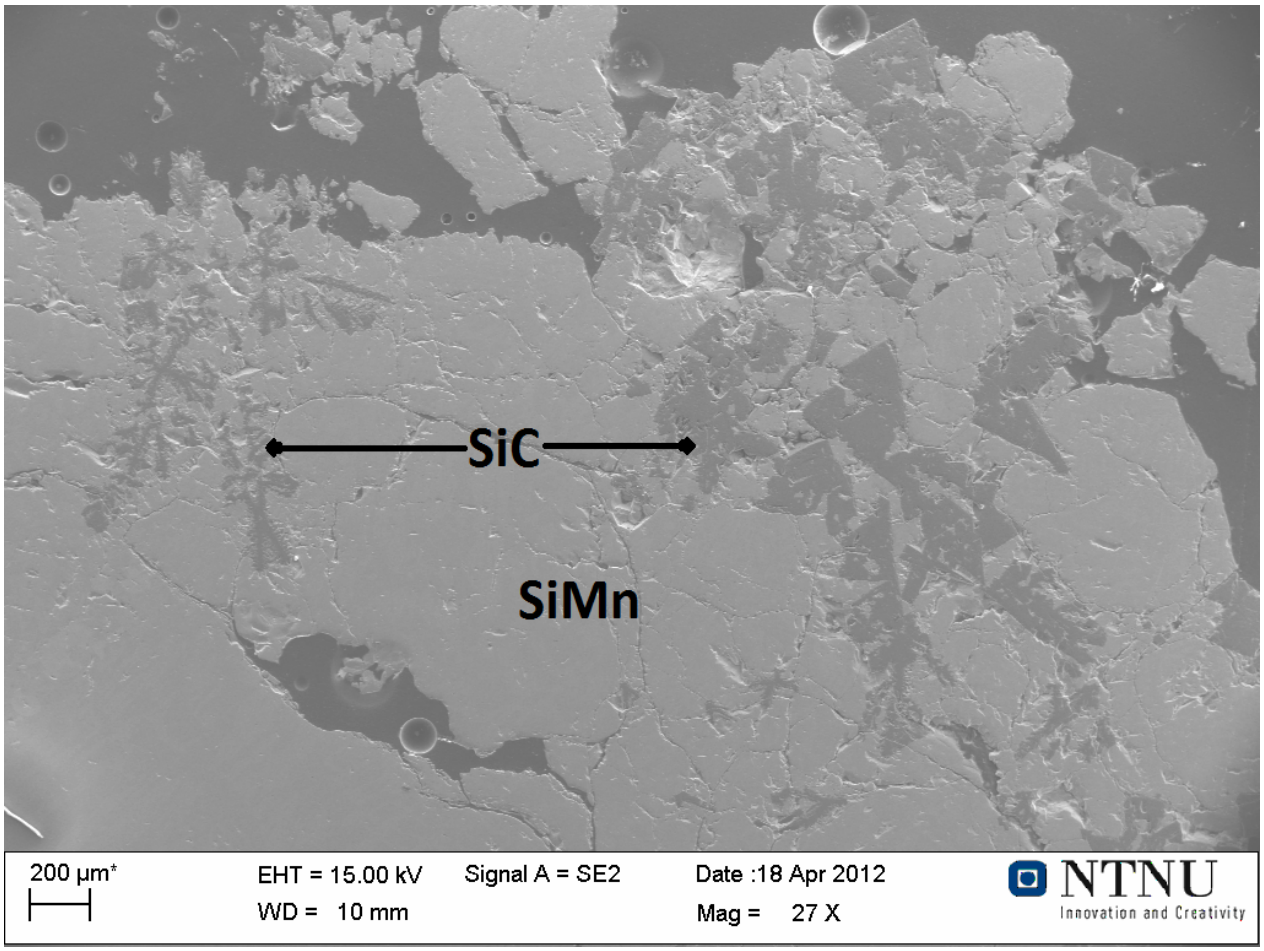

Figure 4.7: Cluster of SiC particles in the form of both dendrites and planar grains.

There was conducted EDS analyses on sample 2 and chemical compositions of SiC and SiMn alloy was found. The analyses of sample 2 is presented in Figure 4.8 and 4.9. The samples were coated with carbon, and the EDAX program compensates for the carbon coat thickness. The exact carbon thickness is still hard to know, and thus the carbon amount in the quantification is not very reliable. The EDS analyses was used continuously on all samples for verification of the phases, but the data was not registered.

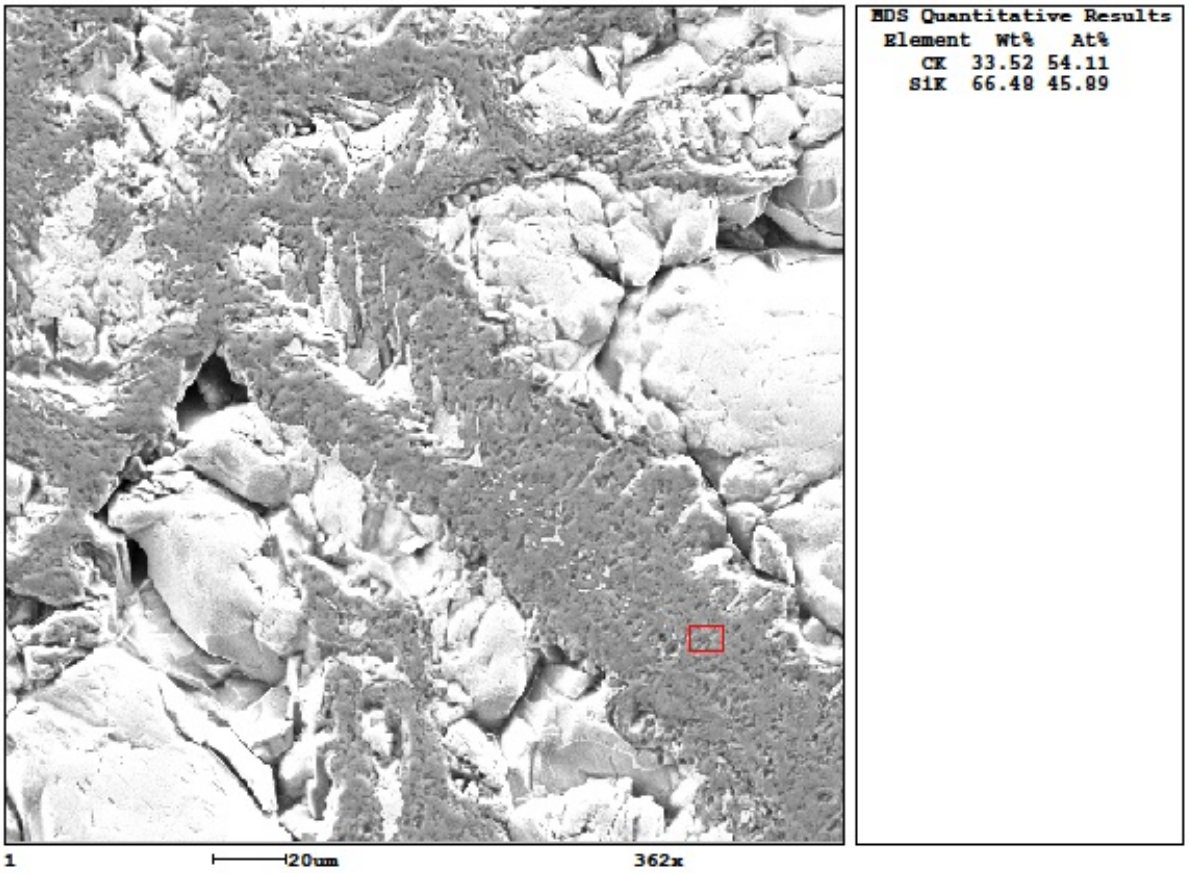

Figure 4.8: EDS analyses of SiC in sample 2 (2 cycles, LC SiMn).

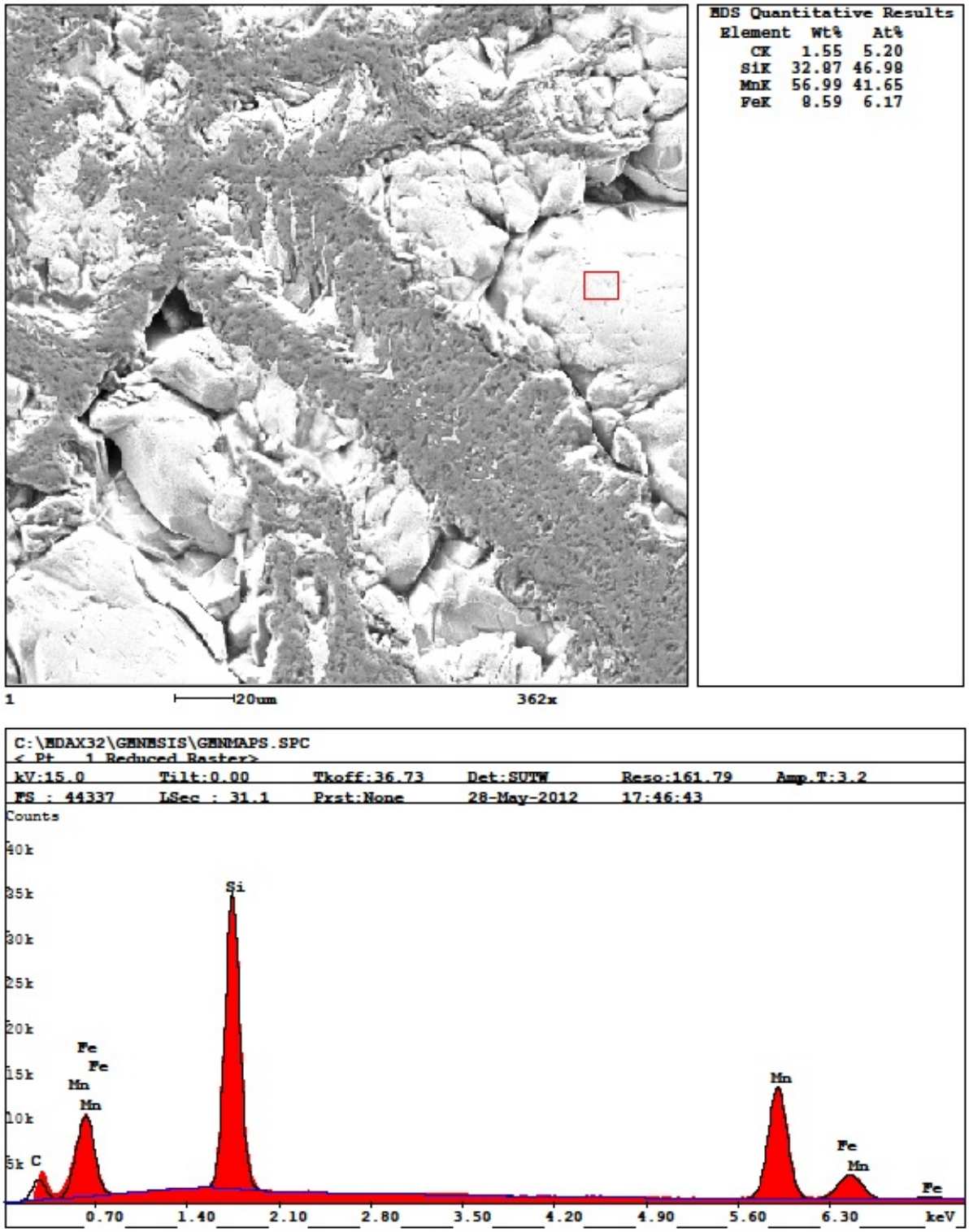

Figure 4.9: EDS analyses of SiMn alloy in sample 2 (2 cycles, LC SiMn).

4.2 Std SiMn

Vol.% of graphite in samples 4-6 is presented in Table 4.2. The data presented in Table (4.2) comes from pictures taken in SEM and analysed as described in section (3.3.2). The vol.% of graphite formed in the SiMn-alloy is rising with amount of cycles from 3.5vol.% to 6.5vol.%. The distribution of graphite grain size is presented in Figure 4.10. There was not conducted any reference experiments of samples 4-6.

Table 4.2: Std. SiMn samples 4-6 at 1, 2 and 4 cycles and volume % graphite. The total average graphite grain size based on measurements, and $m_{C_{Graphite}}$ is the calculated amount of carbon in the form of graphite.

Sample number	# cycles	volume % graphite	$m_{C_{Graphite}}$ $[g]$	Graphite grain size $[mm^2]$
4	1	3.5	1.6	$2.5 \cdot 10^{-3}$
5	2	5.7	2.5	$5.5 \cdot 10^{-3}$
6	4	6.5	2.9	$5.6 \cdot 10^{-3}$

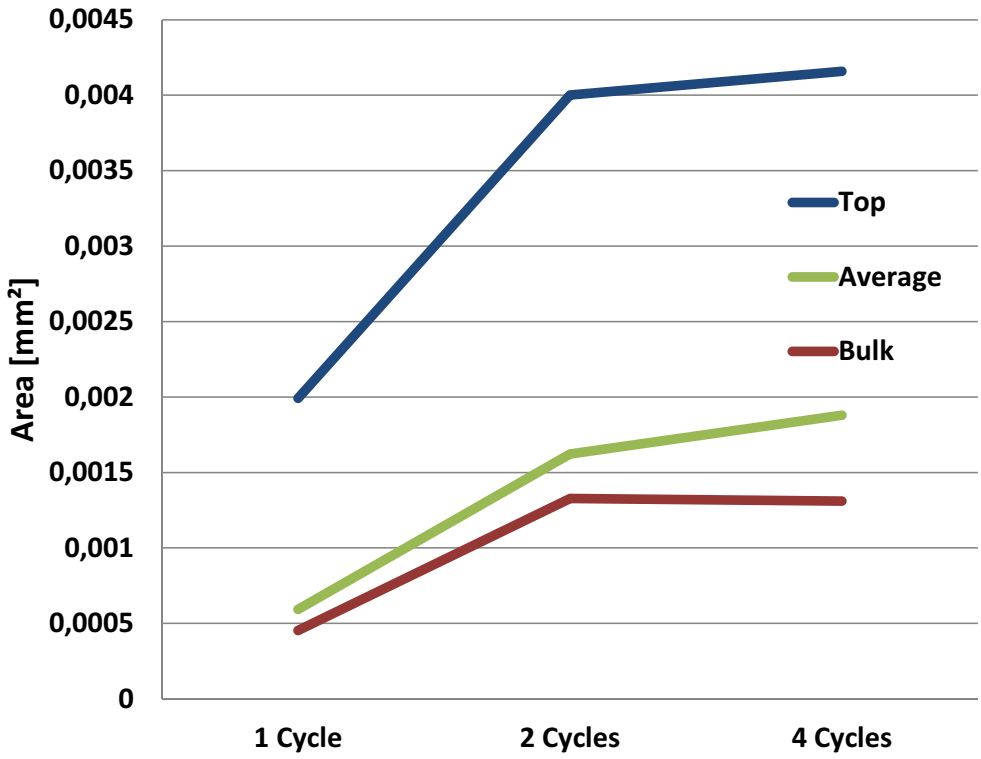

Figure 4.10: The average graphite grain size in the top and bulk of the samples 4-6. The green line is the total average graphite grain size in samples 4-6.

The macroscopic pictures of sample 4-6 are presented in Figure 4.11.

(a) 1 cycle **(b)** 2 cycles **(c)** 4 cycles

Figure 4.11: (a-c) Macroscopic pictures of sample 4-6.

The microscope pictures of samples 4-6 at the top is presented in Figure 4.12 and the bulk in Figure 4.13

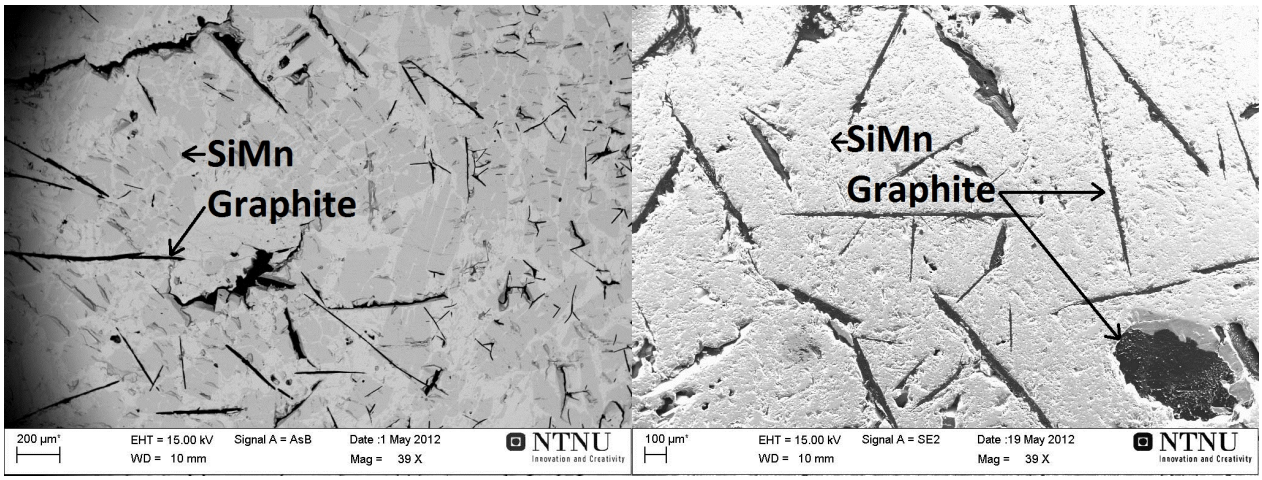

(a) 1 cycle, top of sample 4 **(b)** 2 cycle, top of sample 5

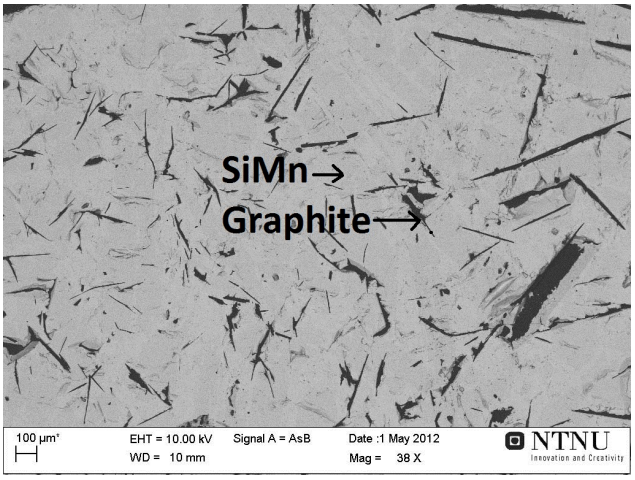

(c) 4 cycle, top of sample 6

Figure 4.12: (a-c) Pictures of the top of sample 4-6 taken in the SEM.

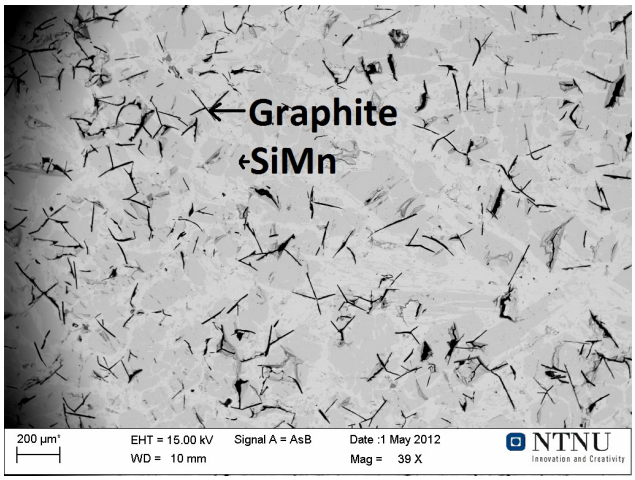

(a) 1 cycle, bulk of sample 4

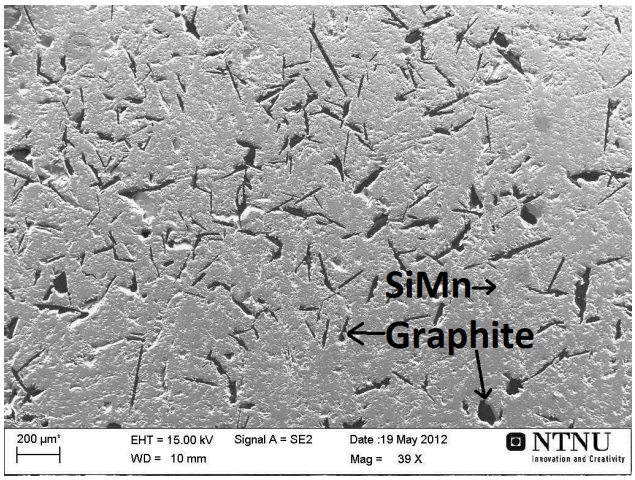

(b) 2 cycles, bulk of sample 5

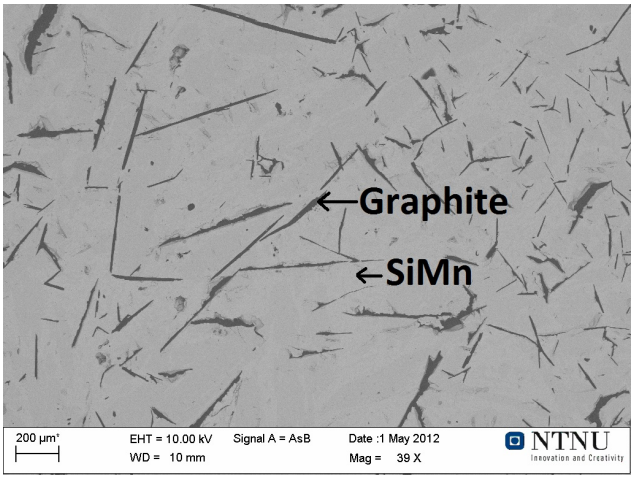

(c) 4 cycles, bulk of sample 6

Figure 4.13: (a-c) Pictures of the bulk of sample 4-6 taken in the SEM.

In Figure 4.14 the bottom of sample 4-6 are presented.

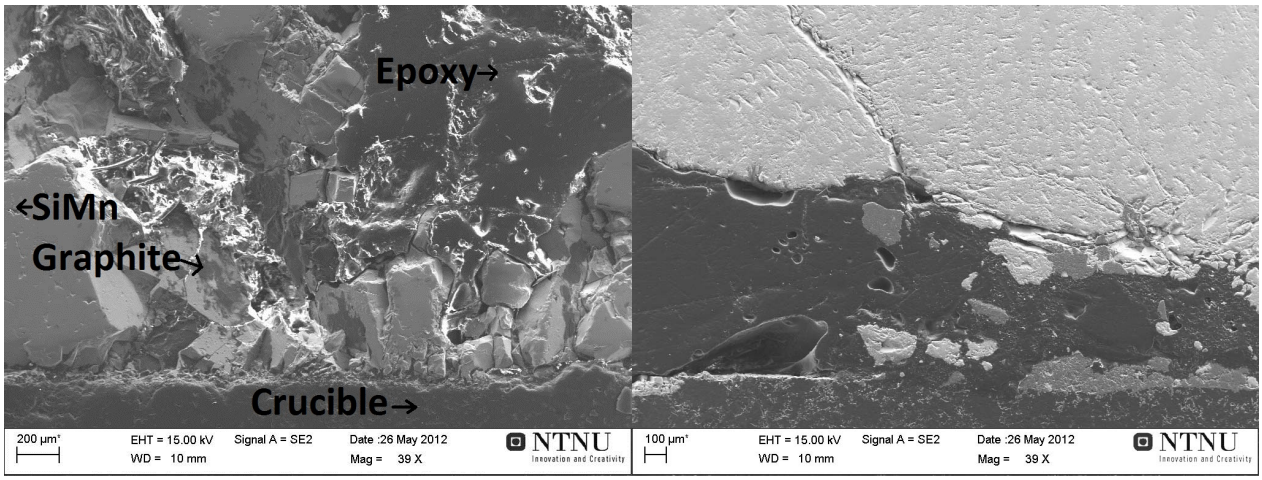

(a) 1 cycle, bottom of sample 4 **(b)** 2 cycles, bottom of sample 5

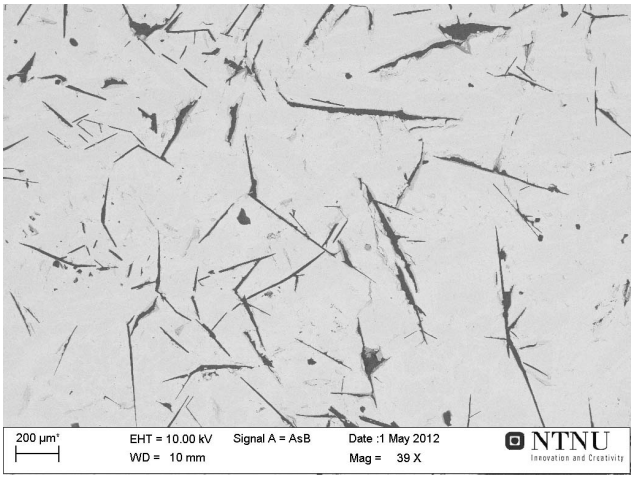

(c) 4 cycles, bottom of sample 6

Figure 4.14: (a-c) Pictures of the bottom of sample 4-6 taken in the SEM.

The transition from larger graphite grains at the top to smaller graphite grains in the bulk are presented in Figure 4.15. It can be seen that the graphite flakes are fairly larger at the top than in the bulk of sample 4, and this is fairly typical for sample 4-9 with graphite formation. The graphite rods on the top of sample 4-6 is at an area protruding c. 2mm deep into the sample. Two phases of SiMn-metal can also be observed in Figure 4.15.

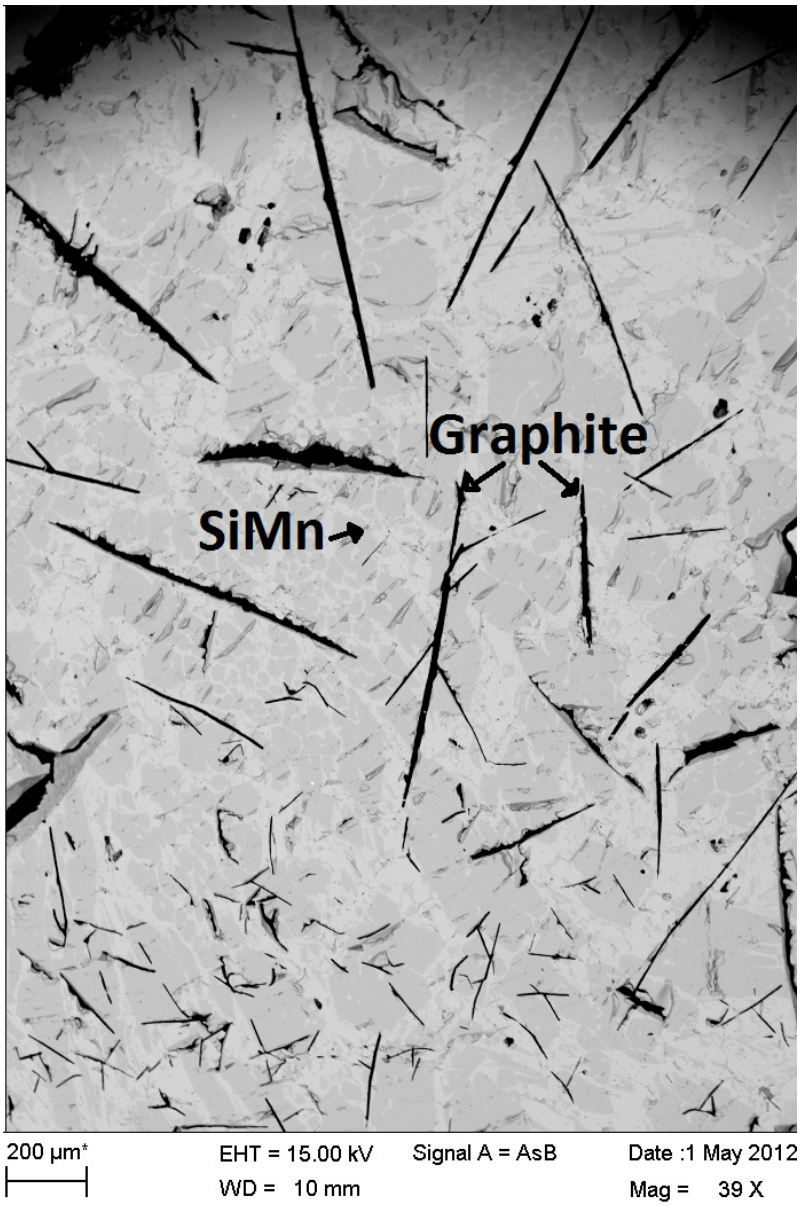

Figure 4.15: Transition area between top and bulk of sample 4. It can be seen that there is c. 2mm with larger graphite flakes at the top of the samples, and the graphite grain size gets smaller further down in the sample. As shown by Einan (2011) the two phases of gray are likely different compositions of SiMn-metal.

There was conducted EDS analyses on sample 5 and chemical compositions of graphite and SiMn alloy was found. The EDS analyses of sample 5 is presented in Figure 4.16 and 4.17 . The samples were coated with carbon, and the EDAX program compensates for the carbon coat thickness. The exact carbon thickness is still hard to know, and thus the carbon amount in the quantification is not very reliable. The EDS analyses was used continuously on all samples for verification of the phases, but the data was not registered. The analyses of graphite show some of SiMn alloy in the background.

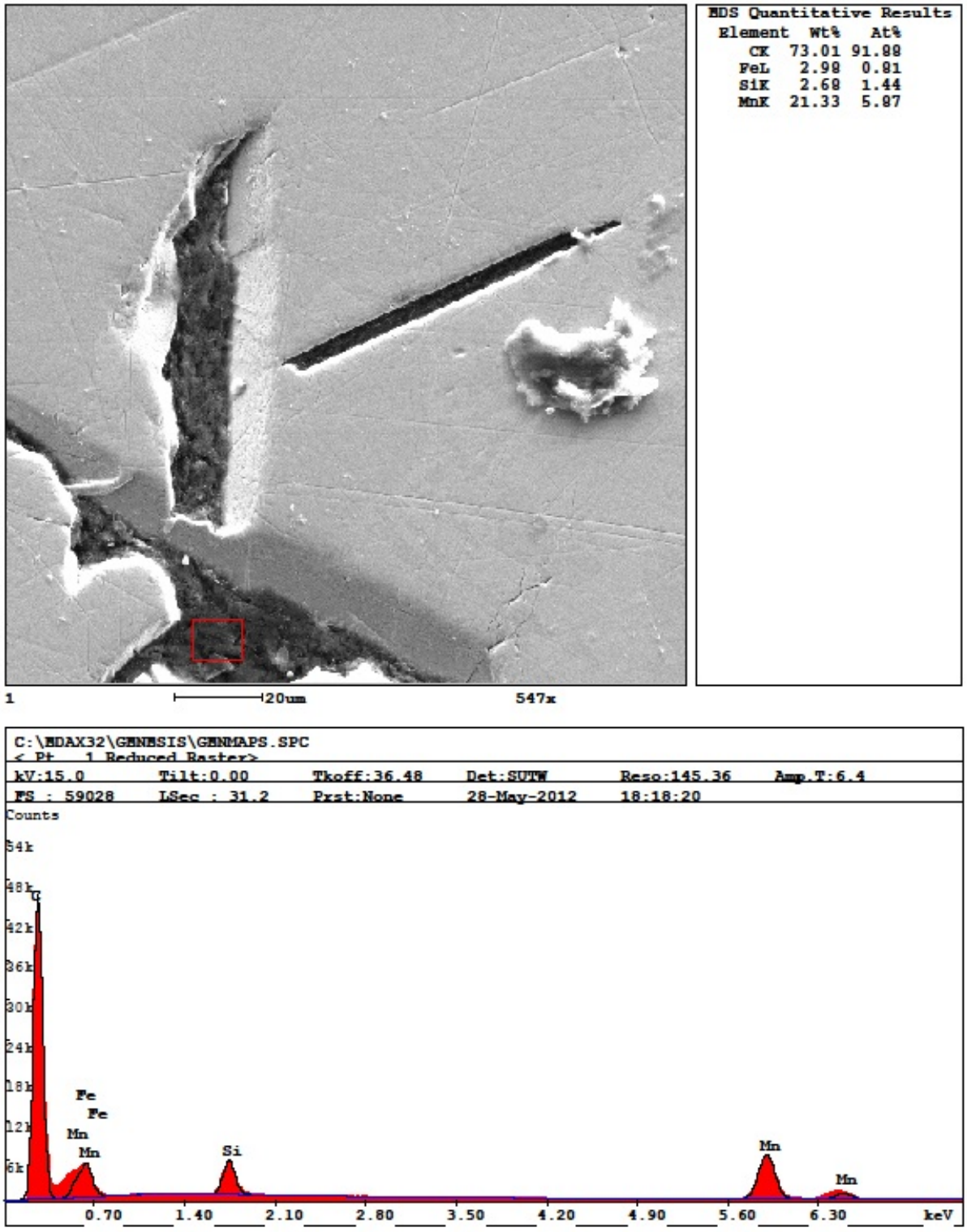

Figure 4.16: EDS analyses of graphite in sample 5 (2 cycles, std. SiMn).

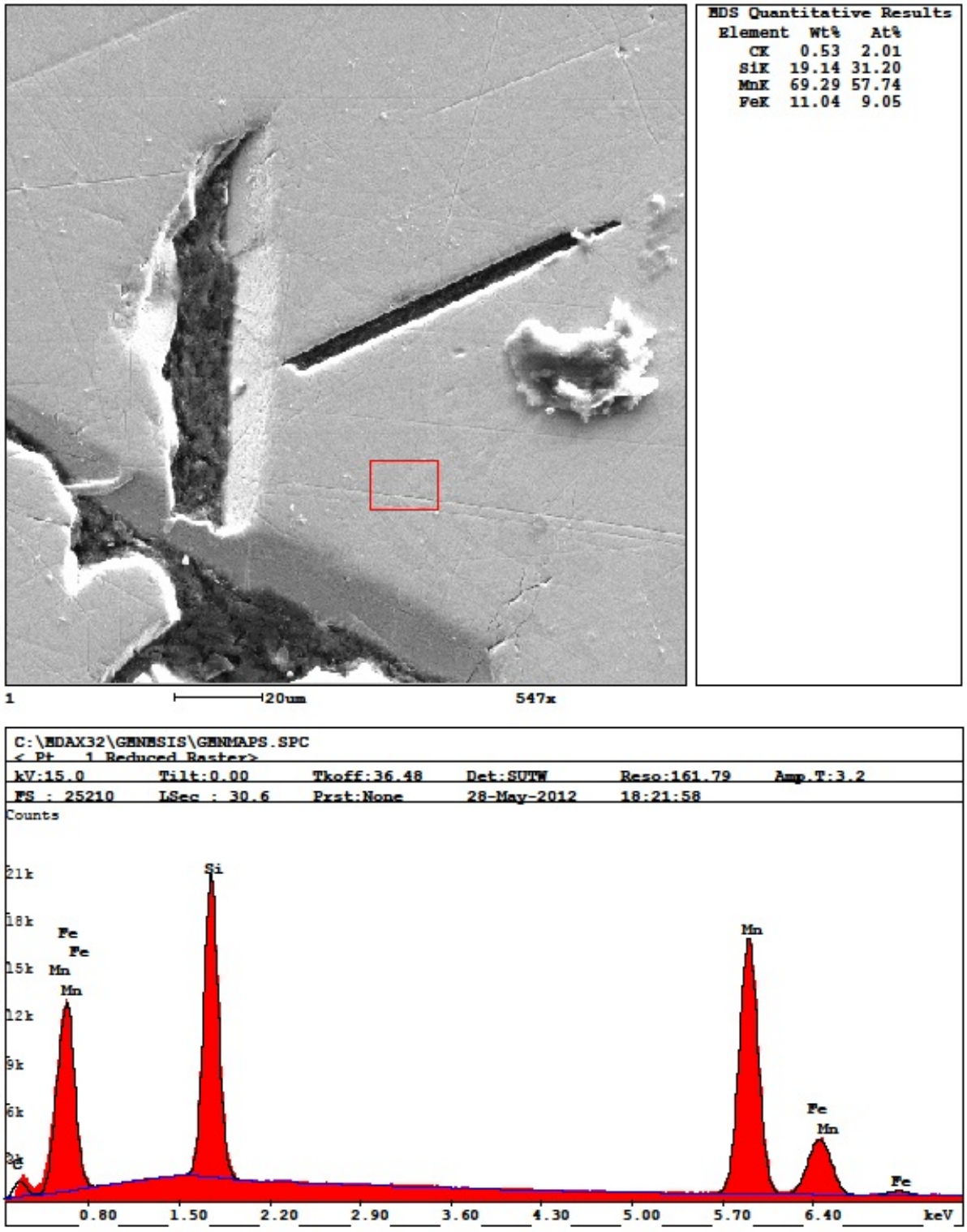

Figure 4.17: EDS analyses of SiMn alloy in sample 5 (2 cycles, std. SiMn).

4.3 HC SiMn

It can be seen that there is a particle of slag and SiMn-metal at the top of the samples. The top particle includes a small amount of graphite flakes. There are some graphite flakes at the top of the samples that are significant larger than those in the bulk and bottom. Vol.% of graphite in samples 4-6 is presented in Table 4.3. There was not conducted any reference experiments of samples 7-9.

Table 4.3: HC SiMn samples 7-9 at 1, 2 and 4 cycles and volume % graphite. The total average graphite grain size was based on measurements, and $m_{C_{Graphite}}$ is the calculated amount of carbon in the form of graphite.

Sample number	# cycles	volume % graphite	$m_{C_{Graphite}}\ [g]$	Graphite grain size $\left[mm^2\right]$
7	1	2.1	0.94	$9.5 \cdot 10^{-4}$
8	2	3.6	1.6	$9.9 \cdot 10^{-4}$
9	4	4.4	2.0	$8.0 \cdot 10^{-4}$

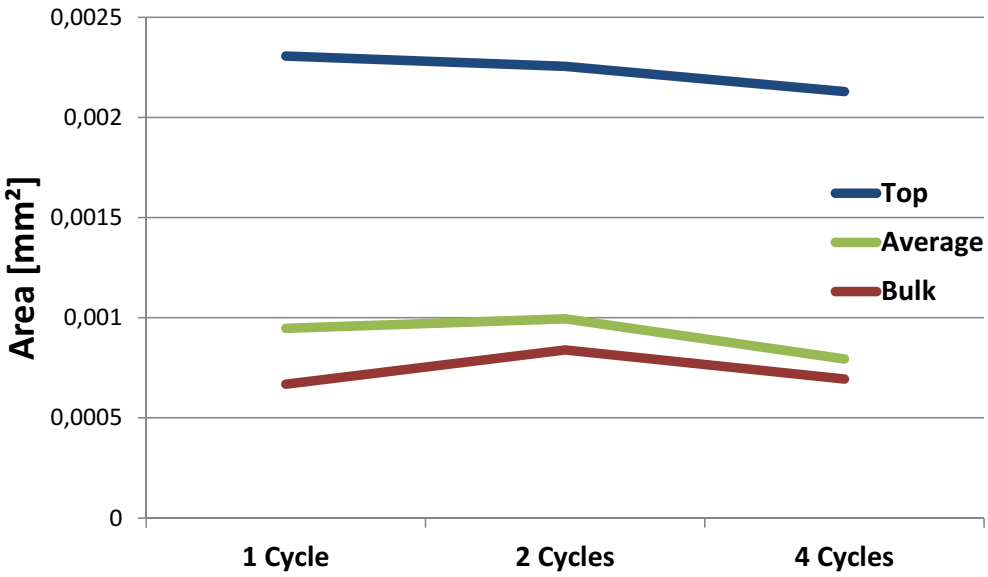

Figure 4.18: The average graphite grain size in the top and bulk of the samples 7-9. The green line is the total average graphite grain size in samples 7-9.

Macroscope pictures of samples 7-9 are presented in Figure 4.19.

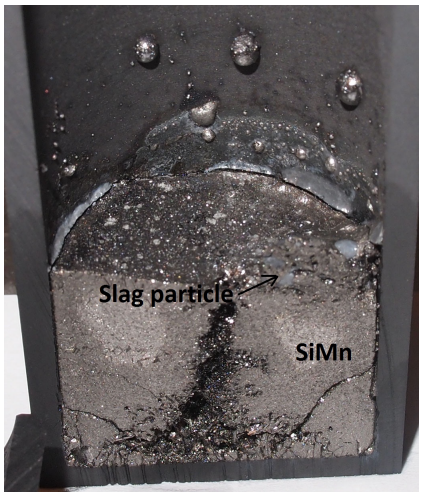

(a) HC SiMn, 1 cycles

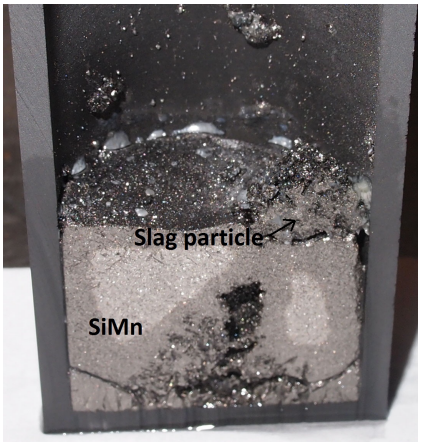

(b) HC SiMn, 2 cycles

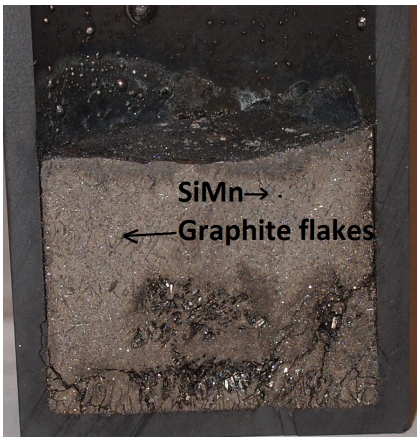

(c) HC SiMn, 4 cycles

Figure 4.19: Macroscopic pictures of (a) sample 7, (b) sample 8 and (c) sample at 9 at 1, 2, and 4 cycles respectively. All 3 samples had a slag particle at the top, but the slag particle was not pictured in sample 9.

In Figures 4.20, 4.21 and 4.22 SEM pictures of the top, bulk and bottom of sample 7-9 are presented.

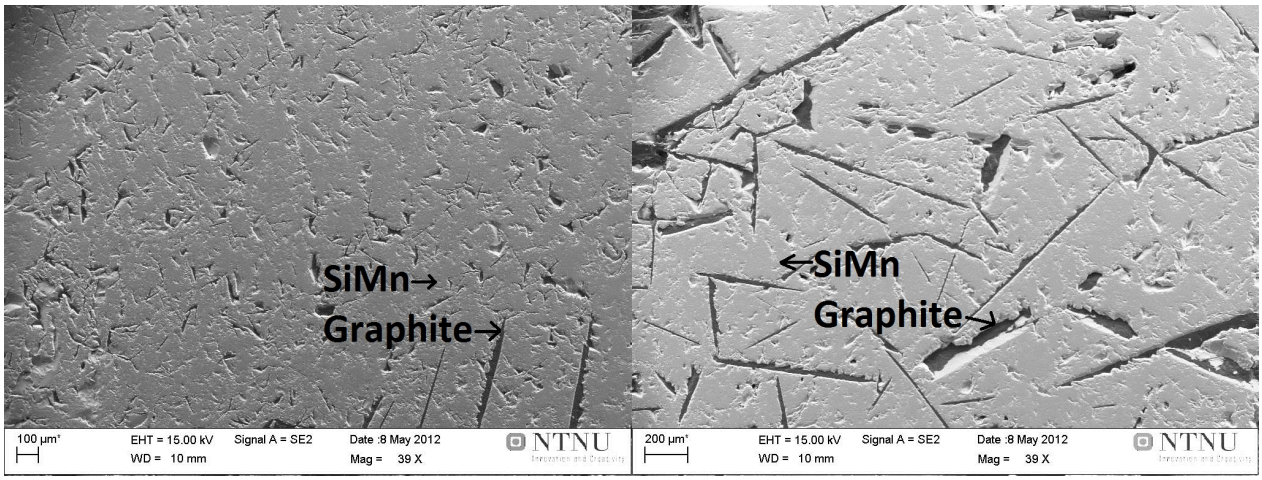

(a) 1 cycle, top of sample 7 **(b)** 2 cycles, top of sample 8

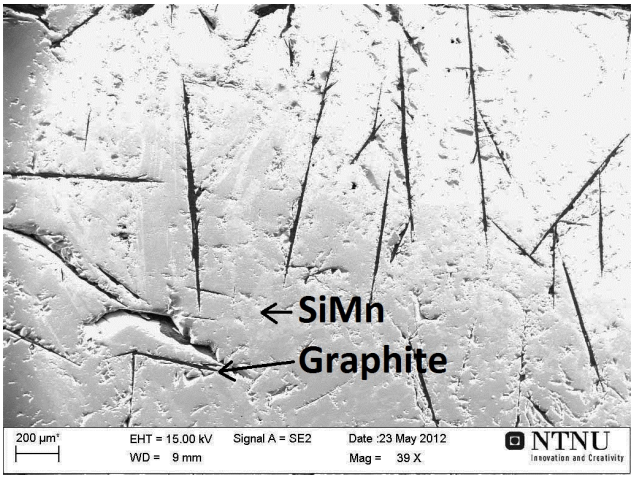

(c) 4 cycles, top of sample 9

Figure 4.20: Pictures taken in the SEM of HC SiMn. (a-c) shows the top of sample 7-9.

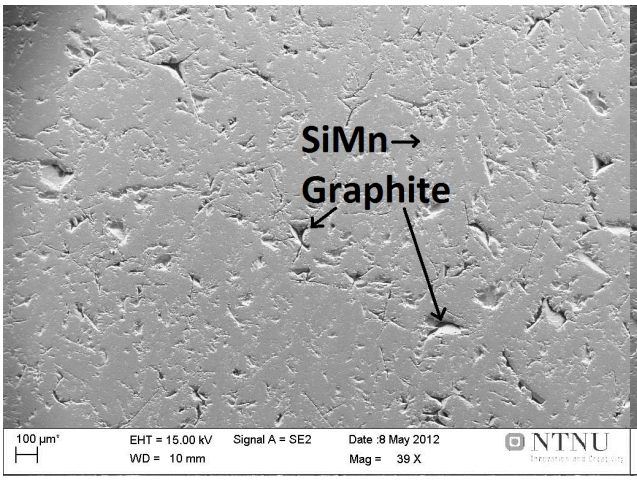

(a) 1 cycle, bulk of sample 7

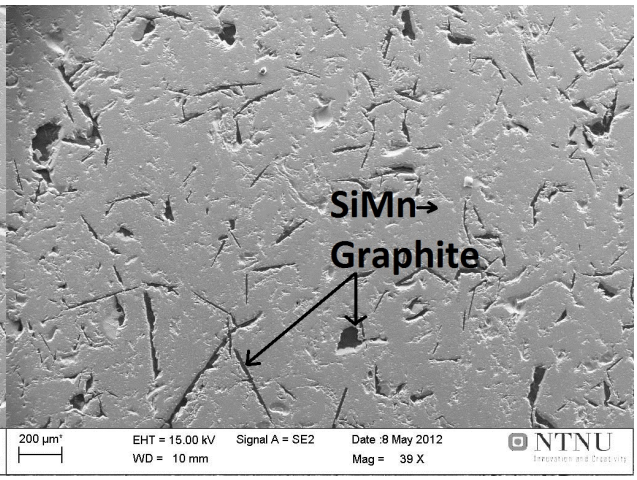

(b) 2 cycles, bulk of sample 8

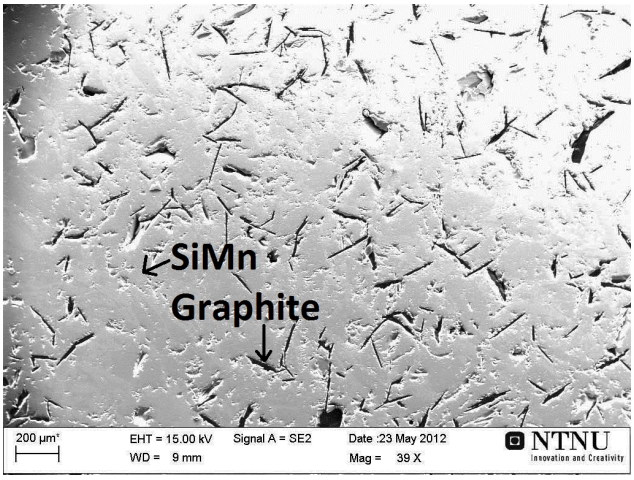

(c) 4 cycles, bulk of sample 9

Figure 4.21: Pictures taken in the SEM of HC SiMn. (a-c) shows the bulk of sample 7-9.

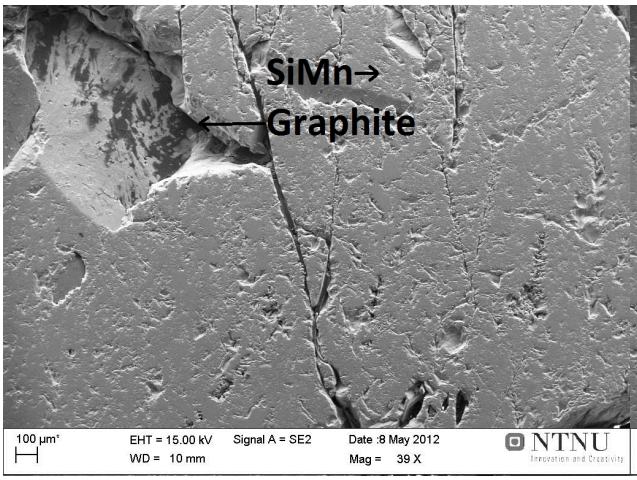

(a) 1 cycle, bottom of sample 7

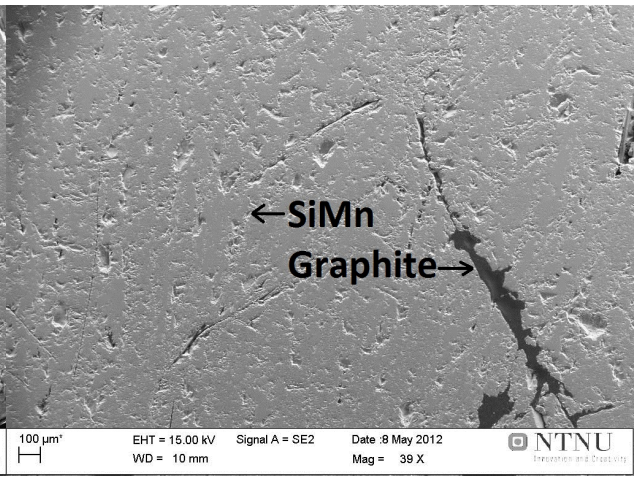

(b) 2 cycles, bottom of sample 8

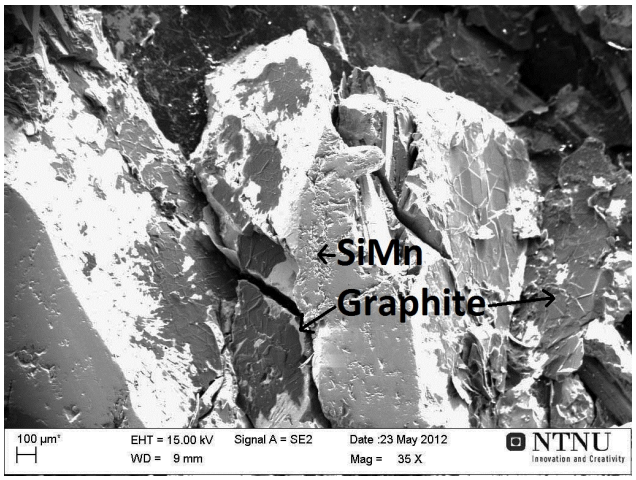

(c) 4 cycles, bottom of sample 9

Figure 4.22: Pictures taken in the SEM of HC SiMn. (a-c) shows the bottom of sample 7-9.

It can be seen from Figure 4.23 that the graphite grains could best be described as flakes not rods. It is suspected that the flakes can be both perpendicular and oblique to the cross section of the samples.

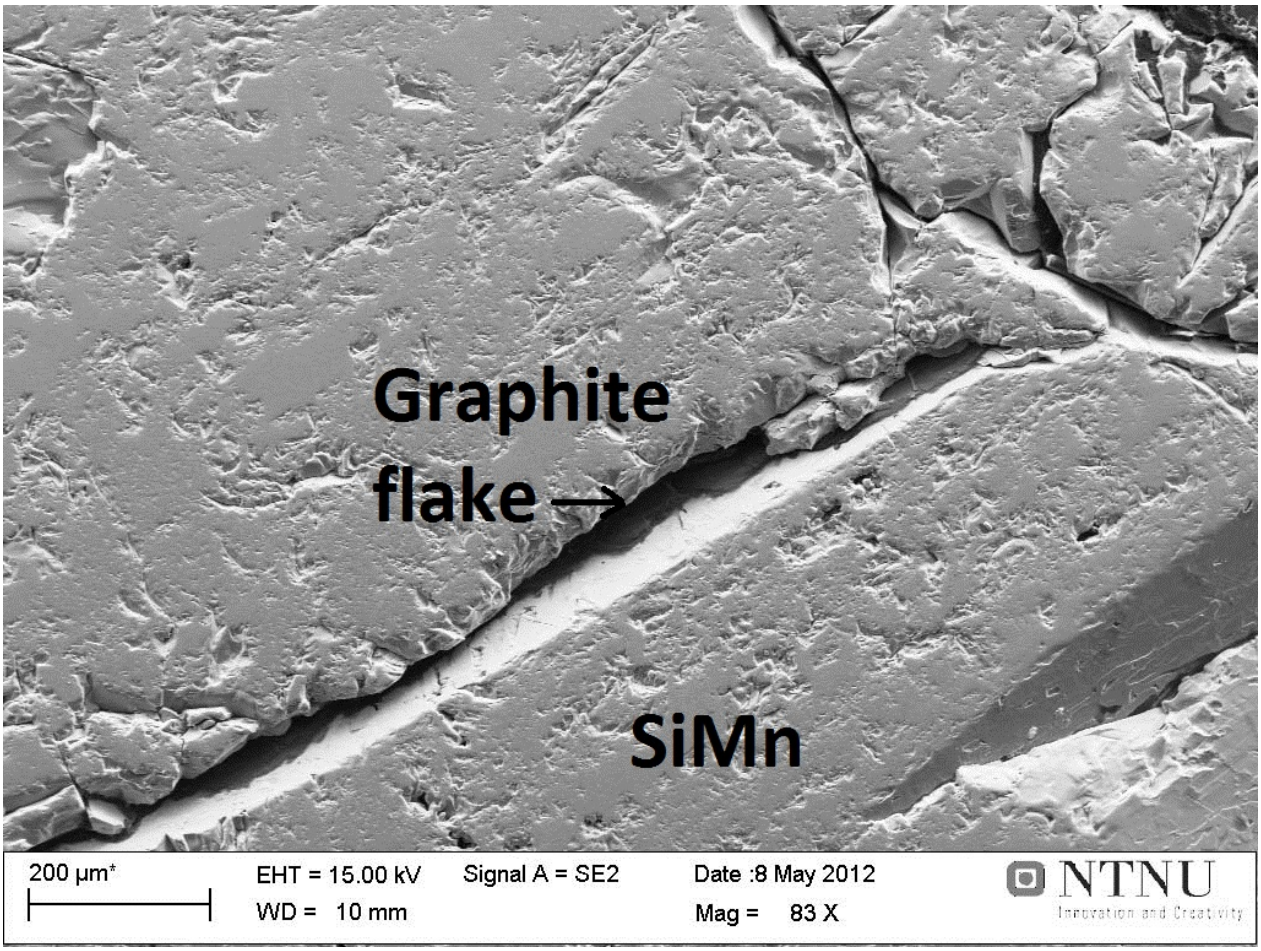

Figure 4.23: Graphite flake at the bottom of sample 7.

The slag composition of the top particle in sample 7 is presented in table 4.4. A parallel of sample 9 was rejected due to suspected high slag amount in the sample and it is thus not representable for the average alloy composition. It can be mentioned that the rejected sample had a layer of TiC at the crucible wall, and some SiC was formed in the bulk and top of the sample. There was a significant layer of slag at the top of the sample.

Table 4.4: Different oxides at top of sample 7. Data from EDAX in the SEM.

Element	Slag 1 [wt.%]	Slag 2 [wt.%]
O	45	44
Al	23	39
Ca	22	-
Si	10	-
Mg	-	17

There was conducted EDS analyses on sample 5 and chemical compositions of graphite and SiMn alloy was found. The EDS analyses of sample 7 is presented in Figure 4.24 and 4.25. The samples were coated with carbon, and the EDAX program compensates for the carbon coat thickness. The exact carbon thickness is still hard to know, and thus the carbon amount in the quantification is not very reliable. The EDS analyses was used continuously on all samples for verification of the phases, but the data was not registered. The analyses of graphite show some of SiMn alloy in the background.

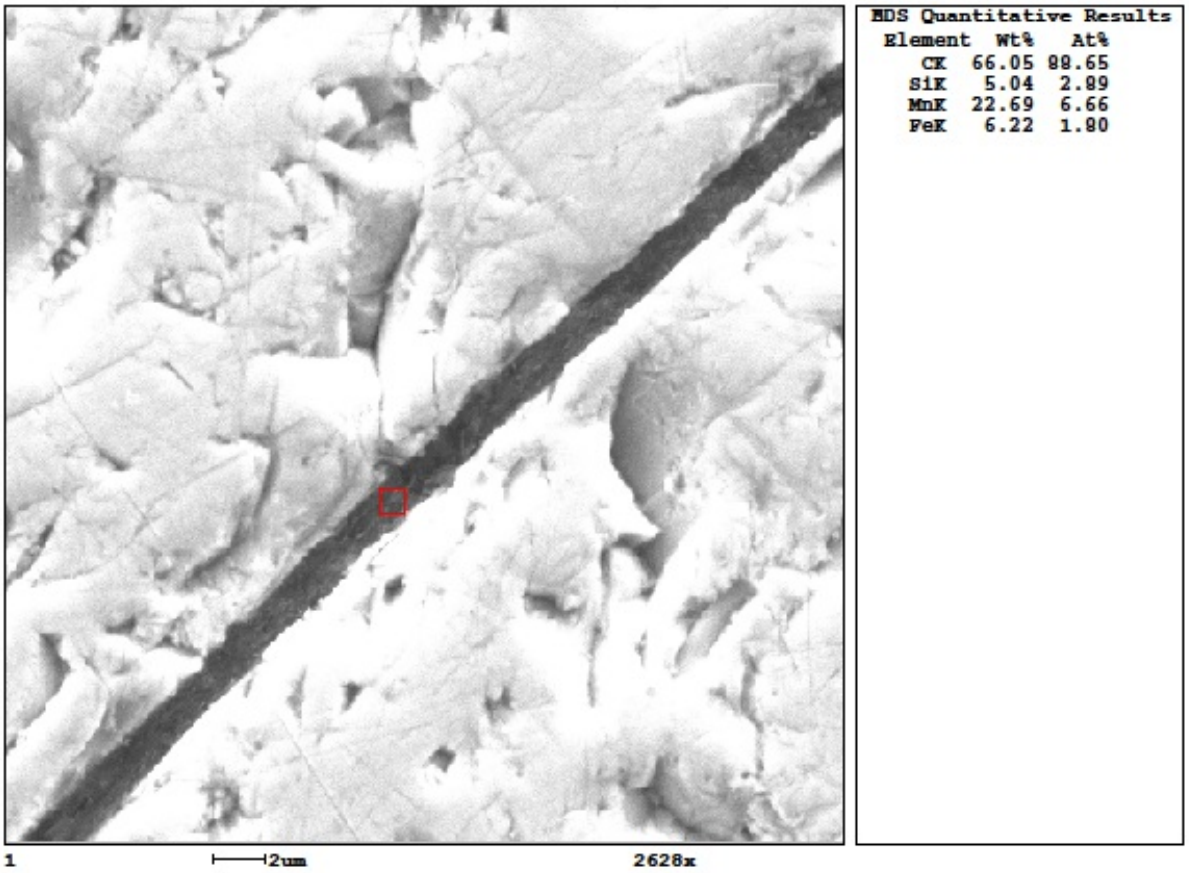

Figure 4.24: EDS analyses of graphite in sample 7 (1 cycle, std. SiMn).

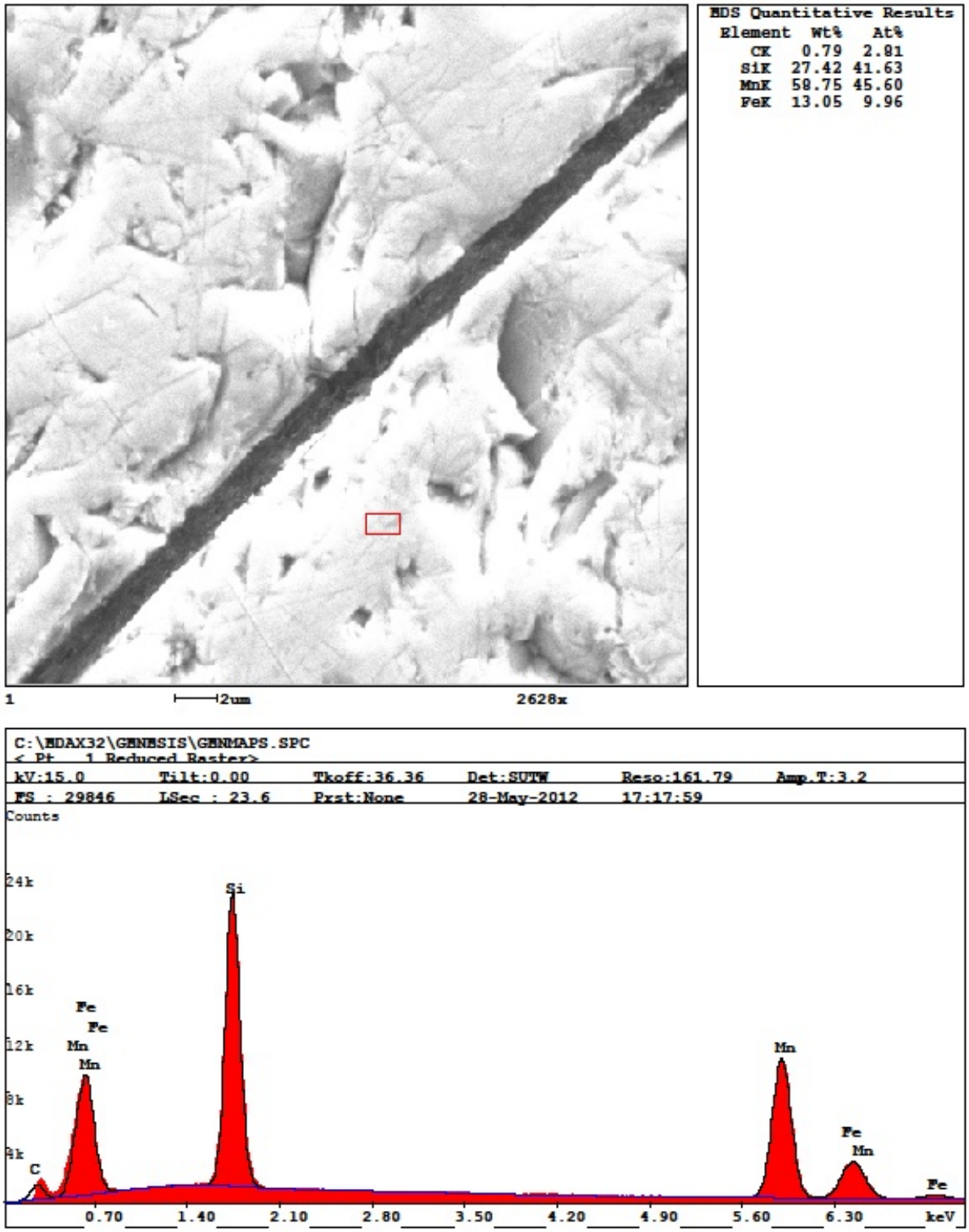

Figure 4.25: EDS analyses of SiMn alloy in sample 7 (1 cycle, std. SiMn).

Chapter 5

Discussion

It was conducted experiments with 3 different SiMn alloys. The results from these 3 alloys, LC SiMn, std. SiMn and HC SiMn will be discussed in the following chapters. In the discussion chapter the following will be presented:

- The main mechanism and rate of formation of SiC and graphite in the silicomanganese process.
- Interface structure of SiC and graphite grains.
- Where the formation occurs.
- Uncertainties in the measurements.
- Industrial perspectives.

5.1 Mechanism

In this chapter the main mechanism of formation of SiC and graphite will be discussed. The crucible dissolves carbon into the alloy to reach equilibrium. Also the driving force of the reactions will be discussed. The rate of formation and driving force of the reaction presents the expected equilibrium composition of the alloy before and after the experiment. The expected difference in carbon between 1610 and 1300°C,$\triangle C$, is compared to the results, and uncertainties in the results is thus quantified.

5.1.1 Main mechanism

As mentioned some carbon from the crucible has dissolved into the liquid alloy to reach equilibrium. This is important because it means that coke in the SAF can dissolve carbon into the SiMn alloy, and thus form SiC or graphite. This phenomena is illustrated in Figure 5.1. Figure 5.1a illustrates that the SiMn alloy is cooled down from 1610 to 1300°C and SiC or graphite is formed. Figure 5.1b illustrates the reheating of the SiMn alloy, where carbon from the crucible is dissolved into the melt to reach equilibrium between silicon and carbon. Figure 5.1c illustrates the cooling of the SiMn alloy after cyclic heating, and more SiC or graphite is formed compared to Figure 5.1a. This can be seen from the carbon balance of the samples that will be presented later.

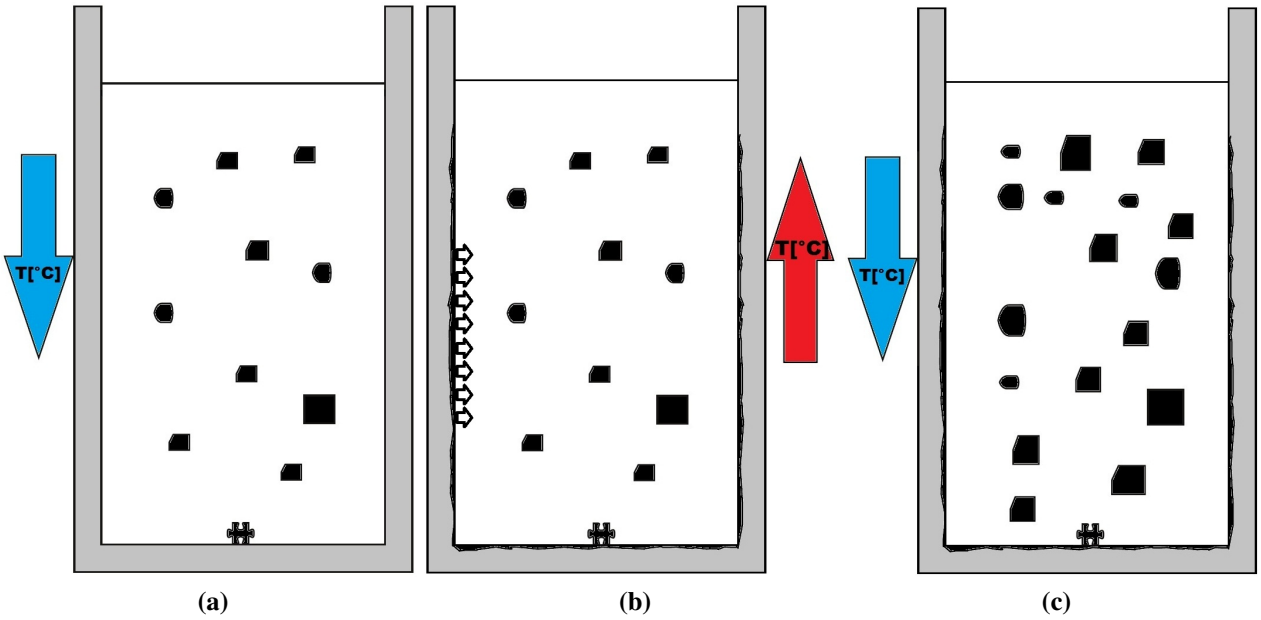

Figure 5.1: (a) SiC or graphite is formed when the SiMn alloy is cooled down from 1610°C. (b) Carbon is dissolved from the crucible to reach equilibrium in the melt when the SiMn alloy is heated up again from 1300°C. (c) Larger amounts of SiC or graphite have accumulated in the melt after step (a) and (b) has been repeated several times.

5.1.2 Mass balance of carbon

If the carbon is dissolved from the crucible into the liquid SiMn-alloy it may be a parallel to the reaction between coke and liquid SiMn in the SiMn-furnace. Olsen et al. (2007) shows that when the temperature in the liquid Mn-Fe-Si-C_{sat} alloy decreases, the solubility of carbon is reduced, and thus graphite or SiC is formed.

The amount of carbon found as SiC or graphite in some of the alloys exceeds the amount of carbon put into the experiments through the alloy, and thus graphite from the crucible has probably dissolved into the alloy. The carbon from the crucible is dissolved to reach equilibrium conditions

in the liquid SiMn alloy as described by Olsen et al. (2007). The mass balance of carbon in the experiments will be discussed below.

Mass balance of carbon for SiC

The amount of carbon bound in SiC in samples 1-3 does not exceed the amount of carbon put into the experiments through the LC SiMn as presented in Figure 5.2. However, according to thermodynamics presented by Olsen et al. (2007), the equilibrium composition of $Mn-Si-Fe-C_{sat}$ alloy would be c. 0.1wt.% carbon at c.29.1wt.% silicon. Carbon would thus have dissolved from the crucible after 2 and 4 cycles, assuming c. 0.1wt.% or more carbon in the alloy. The carbon amount put into the first experiment (1 cycle) should be equal at start and after the experiments. It can be seen from Figure 5.2 that this is not the case, and the difference from "carbon at start" and "total carbon" is thus a quantified deviation that is quite large. However, the tendency in the results relative to one another, makes the deviation tolerable.

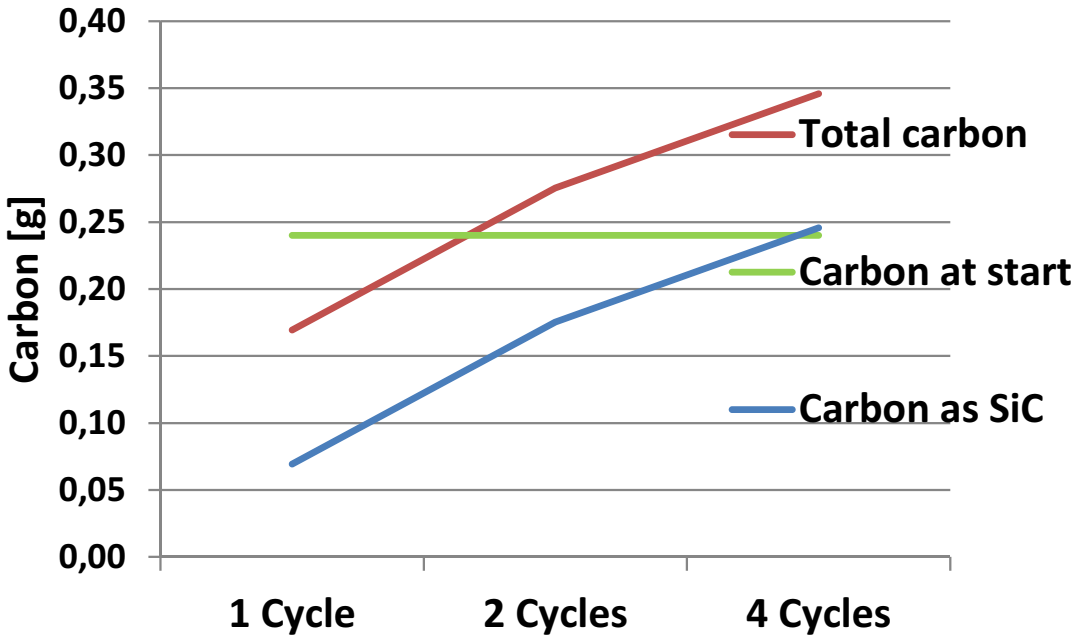

Figure 5.2: Calculated carbon balance of sample 1-3. Carbon at start is the amount of carbon added through the alloy before the experiments started. Carbon as SiC is the calculated amount of carbon bound as SiC after 1, 2 and 4 cycles. Total carbon is the calculated total amount of carbon in the SiC and alloy together assumed 0.1wt.% carbon in the alloy. According to the calculations, carbon should have dissolved from the crucible into the liquid alloy after 2 and 4 cycles.

Mass balance of carbon for graphite

The amount of carbon that dissolved in samples 4-9 to form graphite is presented in Figure (5.3). The figure shows that carbon dissolved from the crucible in sample 4-6, 8 and 9. As discussed

earlier this suggests that if the SiMn is reheated in the submerged arc furnace, it may solve C from the cokebed and thus form SiC or graphite when its cooled. The deviation mentioned in the mass balance of carbon for SiC also applies for graphite.

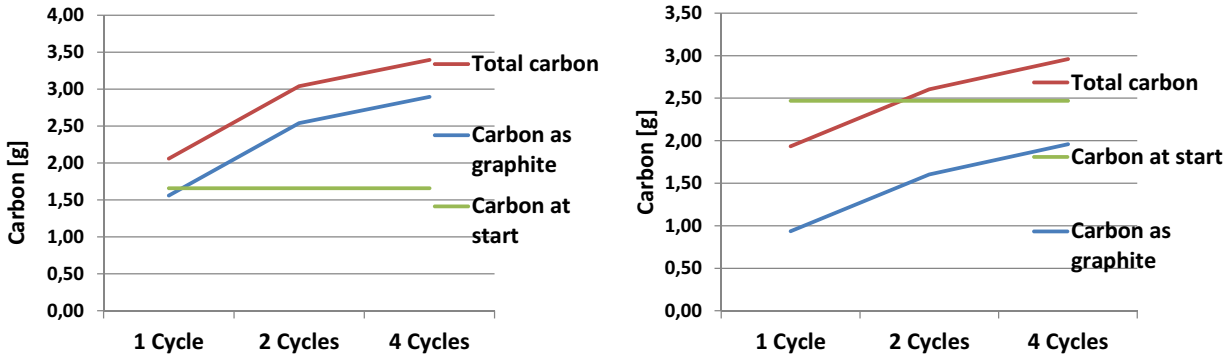

(a) Sample 4-6, std. SiMn

(b) Sample 7-9, HC SiMn

Figure 5.3: Calculated carbon balance of (a) sample 4-6 and (b) sample 7-9. Carbon at start is the amount of carbon added through the alloy before the experiments started. Carbon as graphite is the calculated amount of carbon bound as graphite after 1, 2 and 4 cycles. Total carbon is the calculated total amount of carbon in the graphite and alloy together assumed 0.5wt.% carbon in sample 4-6 and 1wt.% carbon in sample 7-9. According to the calculations, carbon should have dissolved from the crucible into the liquid alloy in all samples in this figure except sample 7.

5.1.3 Rate of formation

The amount of SiC and graphite formed in sample 1-9 increases with number of cycles as presented in Figure 5.4. The results show that the rate of formation of SiC/graphite is reduced by each consecutive cycle. This suggest that $^{SiC}/_{graphite}$ formed after the first cycles can partly dissolve into the liquid SiMn alloy to reach equilibrium. Sample 2, 3a and 3b has partly layers of SiC on the crucible wall, and it is possible that this affects the rate of formation of SiC.

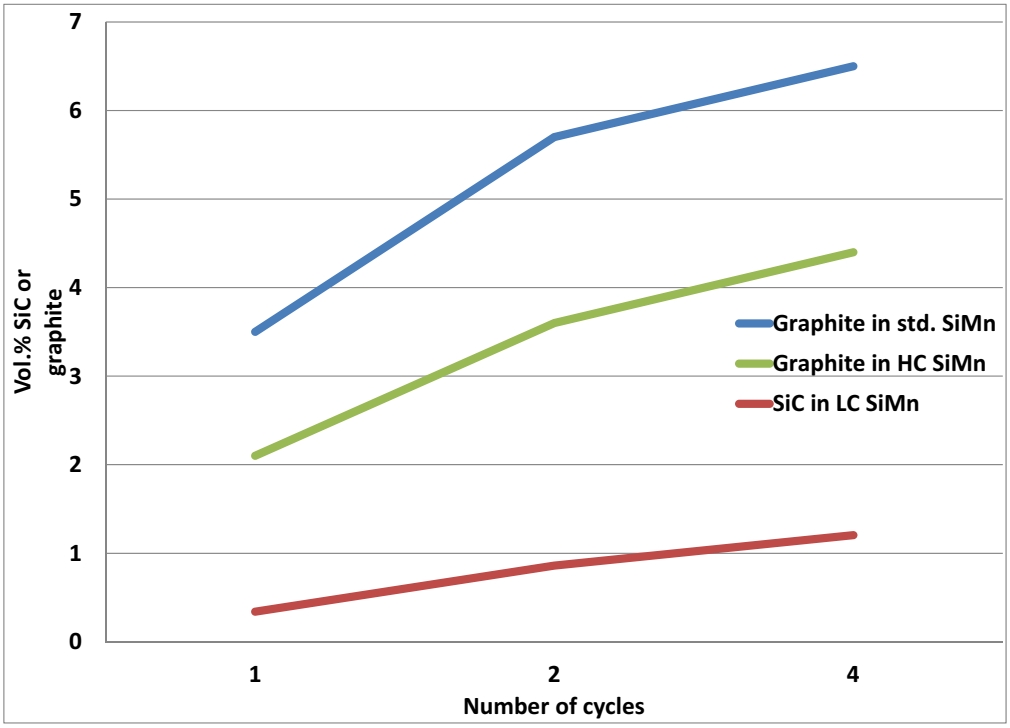

Figure 5.4: Volume % SiC and graphite in samples 1-9. The rate of $^{SiC}/_{graphite}$ formed at each cycle is decreasing with increasing amount of cycles.

As Hon et al. (1980) describes the rate of formation of SiC or graphite can be described by Equation (5.1), when the temperature is constant and the silicon content is the main variable. However, this thesis investigates systems with close to constant silicon content and the temperature as the main variable. The driving force of the formation of SiC and graphite is therefor $(wt.\%C_{1610°C} - wt.\%C_{1300°C})$ in these systems and the rate of formation is presented in Equation (5.2). The SiC and graphite is believed to form when the liquid alloy is cooled from 1610 - 1300°C.

$$r = A \cdot k \cdot \left((wt.\%C)_{metal} - (wt.\%Si)_{C/SiC} \right) \tag{5.1}$$

$$r = A \cdot k \cdot (wt.\%C_{1610°C} - wt.\%C_{1300°C}) \tag{5.2}$$

The driving force of formation of SiC and graphite is modified into the the solubility diagram of carbon and silicon presented in Figure 5.5. The solubility diagram shows the calculated solubility lines between 1500 and 1650°C. The driving force of formation of SiC and graphite from 1610 - 1300°C is c. twice the driving force from 1650 - 1500°C, assuming a linear relationship between the solubility lines. The driving force from 1610 - 1300°C results in a carbon difference,$\triangle C$, and that is the expected dissolved carbon to form SiC or graphite. The numbers in the modified solubility diagram indicates half of $\triangle C$ for the HC, std and LC SiMn samples as follows:

1. HC SiMn (sample 7-9) $\triangle C_{sample\,7-9} = 2 \cdot \triangle C_1 = 2 \cdot 0.7 = 1.4$

2. Std. SiMn (sample 4-6) $\triangle C_{sample\,4-6} = 2 \cdot \triangle C_2 = 2 \cdot 0.8 = 1.6$
3. LC SiMn (sample 1-3) $\triangle C_{sample\,1-3} = 2 \cdot \triangle C_3 = 2 \cdot 0.3 = 0.6$

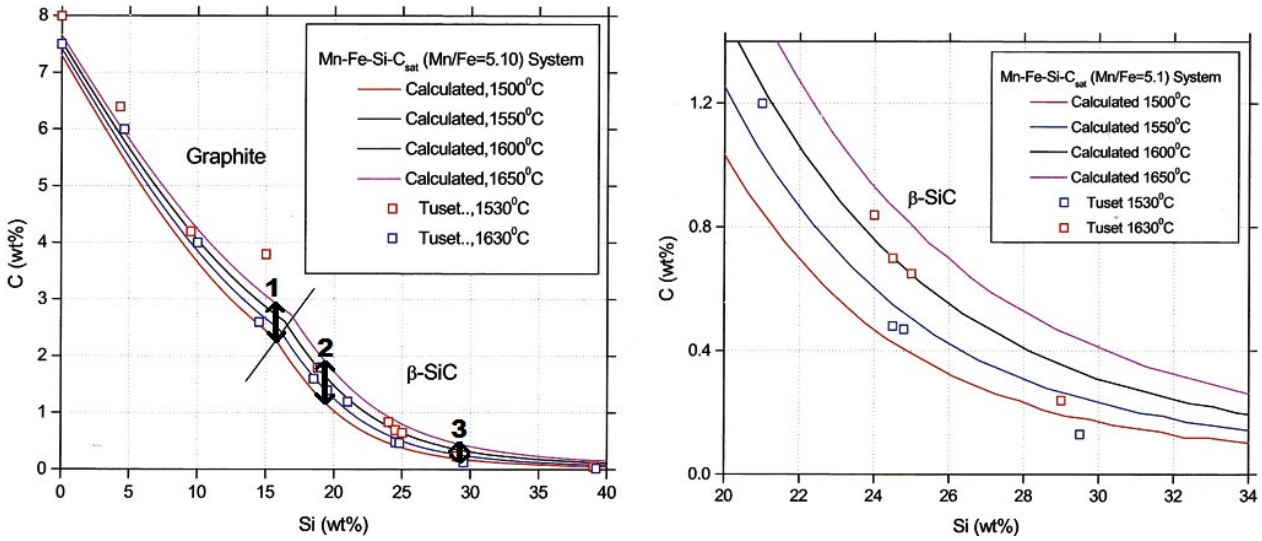

Figure 5.5: Calculated carbon solubility as a function of silicon content in a Mn-Fe-Si-C_{sat} alloy with $^{Mn}/_{Fe}$ = 5.1 between 1500°C and 1600°C. The graph on the right side show a close up of the high silicon area. Figure is taken from Olsen (2001)

The carbon equilibrium composition at 1610°C of samples 1-3 is c. 0.4wt.%, and a reduction in carbon content of 0.6wt.% is impossible. A carbon content in the alloy of c.0.1wt%. after the experiments is more likely and assumed, thus resulting in $\triangle C'_{sample\,1-3} = 0.3$. This means that each time a sample is cooled from 1610°C the expected carbon dissolved from SiMn alloy,$\triangle C$ forms SiC or graphite as presented in Table 5.1. The deviation between the calculated values and the results are large, but the tendency in the results relative to one another, makes the deviation tolerable.

Table 5.1: $\triangle C_{Calculated}$ is the expected carbon dissolved during cooling to form SiC or graphite. $\triangle C_{Results}$ is the carbon amount in the measured SiC or graphite in the experiments. The deviation is the absolute value of the difference between $\triangle C_{Calculated}$ and $\triangle C_{Results}$. The $\triangle C_{Results}$ (LC SiMn, 4 cycles) is the average of sample 3a and 3b.

Alloy	Cycles	$\triangle C_{Calculated}\,[g]$	$\triangle C_{Results}\,[g]$	Deviation $[g]$
HC SiMn	1	1.4	0.94	0.46
	2	2.8	1.6	1.2
	4	4.2	2.0	2.2
Std. SiMn	1	1.6	1.6	0
	2	3.2	2.5	0.7
	4	4.8	2.9	1.9
LC SiMn	1	0.3	0.34	0.04
	2	0.6	0.86	0.26
	4	0.9	1.21	0.31

5.2 Interface structure of SiC and graphite grains

5.2.1 Interface structure of SiC

SiC is formed when the liquid LC SiMn-alloy is cooled. The dissolved carbon would react with silicon in the liquid alloy and form SiC as presented in equation 5.3. (Olsen et al. 2007)

$$C + \underline{Si} = SiC\,(s) \tag{5.3}$$

The results show that SiC can be in the form of granular, angular grains or as dendrites. Kurtz & Fisher (1998) explains that dendritic growth happens into a poor inoculated liquid. In this case it can be assumed that the liquid SiMn-alloy is poorly inoculated on carbon. According to thermodynamics Olsen et al. (2007) presents that when the liquid SiMn-alloy is low on silicon, graphite would form instead of SiC . When the liquid has a low amount of carbon atoms, dendritic SiC can form. The dimensionless entropy, α, can be used to predict interface structure. For $\beta - SiC$ the dimensionless entropy is 2.0 which is in the borderline of dendritic and planar growth. According to Kurtz & Fisher (1998) this would mean that $\beta - SiC$ probably has planar, angular grains, but its

possible to get dendrites too. In the case of sample 1-3 there is a mixture of dendritic and angular SiC.

When SiC clusters are formed, the area with SiC is significantly increased. Comparing SiC clusters with planar, angular grains shows that the average clusters is one decade larger than the average planar, angular SiC grains. These SiC clusters are a mixture of SiC and SiMn-metal as presented in Figure 5.6.

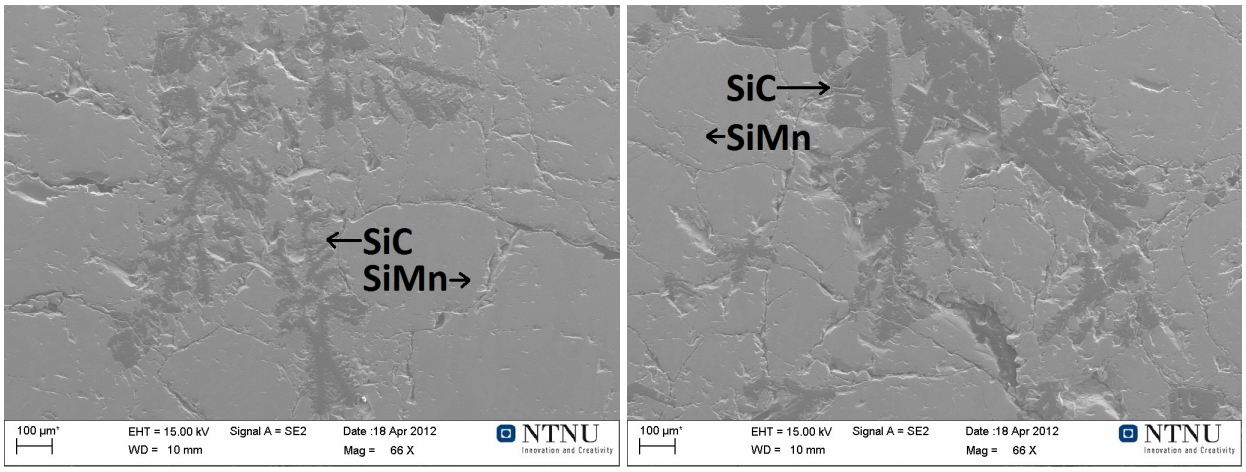

(a) **(b)**

Figure 5.6: SiC clusters with intermediate SiMn-alloy. (a) SiC in the form of dendrites and (b) SiC in the form of angular, planar grains with dendrites growing on them. Both SEM pictures is taken at the top of sample 3a. The average size of the SiC clusters is c. $0.7mm^2$. The dark gray phase is the SiC and the light gray phase is SiMn-alloy.

5.2.2 Interface structure of graphite

The dissolution of carbon from the SiMn alloy to form graphite can be described by Equation (5.4). According to Olsen et al. (2007) the activity coefficient of carbon in Equation (5.4) is dependent on other pure elements in the alloy such as silicon, manganese and iron. Sample 4-6 have an $^{Mn}/_{Fe}$ ratio of 6.4 which is not far from the $^{Mn}/_{Fe}$ ratio in the solubility diagram of carbon and silicon in a $Mn-Fe-Si-C_{sat}$ alloy as presented in Figure 5.5.

$$\underline{C} = C_{gr} \tag{5.4}$$

Graphite is formed when the liquid std. and HC SiMn-alloy is cooled. Graphite is the stable phase of the dissolved carbon coexisting with liquid alloys until the silicon content reaches a certain value. According to Olsen et al. (2007) the point of coexistence where SiC starts to be the stable phase increases slightly with temperature from c.16-18wt.% silicon the solubility diagram of carbon and silicon in a $Mn-Fe-Si-C_{sat}$ alloy with a $^{Mn}/_{Fe}$ ratio of 5.1 presented in Figure 5.5. This

suggests that the std SiMn with an original composition of 19.0wt.% silicon and 1.66wt.% carbon should form SiC from the dissolved carbon, however graphite was found to be the stable phase in samples 4-6. This is in accordance with Tuset & Sandvik (1970) that found that that with silicon concentrations less than 20wt.% the dissolved carbon precipitated out as graphite flakes in the cross section of the samples.

In accordance with Gruzleski (1975) the graphite grains are suspected to be flakes as presented in Figure 5.7. A vertical or horizontal cross section might not be sufficient to picture the correct grain size of oblique graphite grains. In future work, etching of the samples should be done to obtain an in dept analyses of graphite grains.

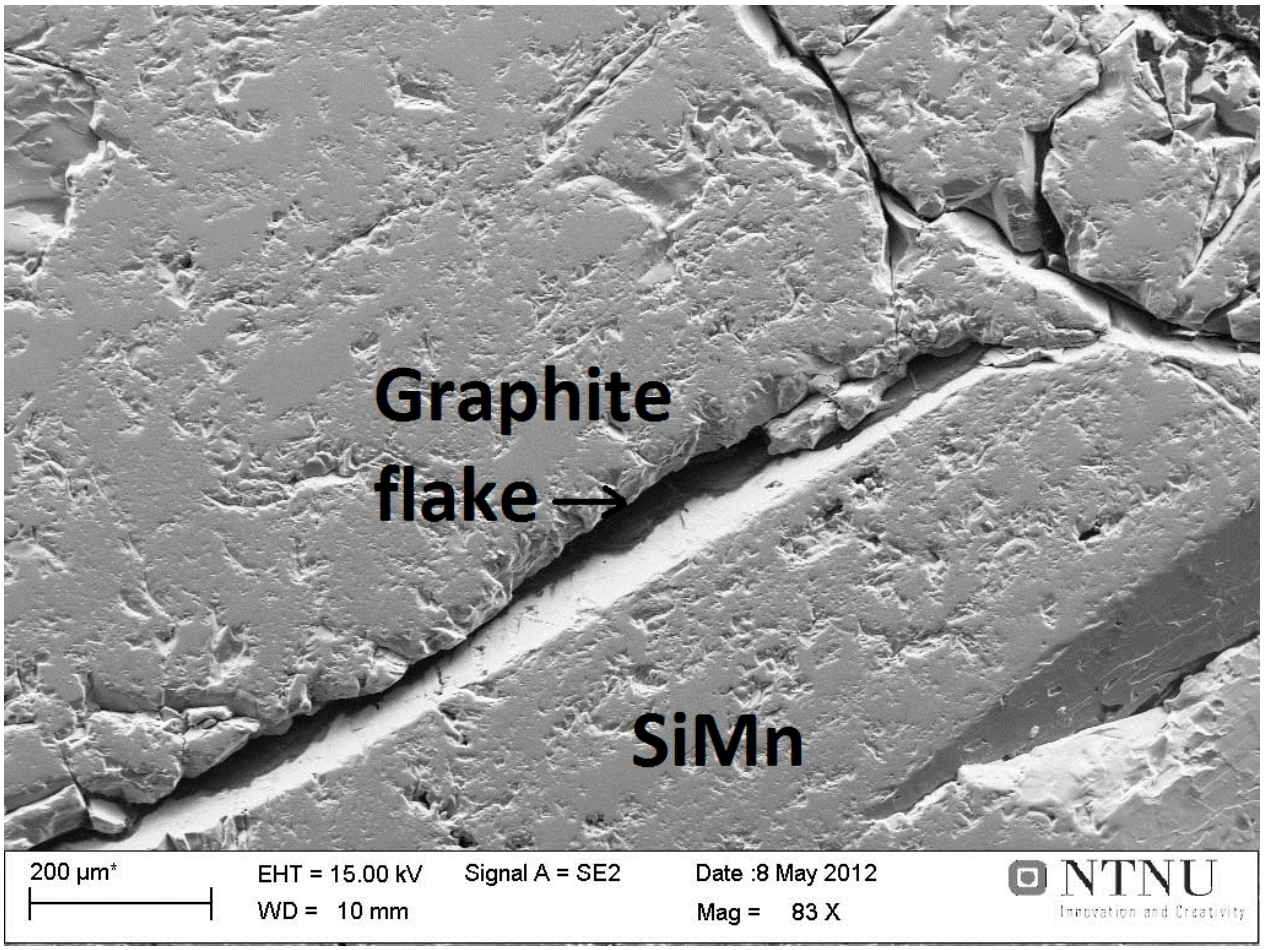

Figure 5.7: Graphite flake at the bottom of sample 7.

5.3 Placement of SiC and graphite grains

The results from the vertical tube furnace shows that SiC has formed in the SiMn alloy when subjected to heating cycles. Above 90vol.% of the SiC was found on the top of the samples, while the rest was found on the crucible wall or as dendrites protruding from the crucible bottom upwards

in the SiMn alloy. The results from the vertical tube furnace also showed that graphite formed in the SiMn alloy when subjected to heating cycles. The graphite was found all over the samples, but the length of the graphite flakes was 2-4 times longer at the top of the samples compared to the bulk. This will be discussed in the following chapters.

5.3.1 Placement of SiC

Kurtz & Fisher (1998) explains that nucleation occurs at existing surfaces, thus it is likely that SiC forms on the graphite crucible and grows from existing SiC grains. However, previous experiments with HC FeMn + Si by Davidsen (2011) and Einan (2011) suggest that SiC forms in the bottom, bulk and top of the liquid alloy. These experiments had quite steep cooling rate after its holding time at 1600°C. With a longer cooling time and most likely a lower viscosity due to less SiC than these previous experiments, the SiC floats to the top because of its lower density ($\rho_{SiC} = 3.21 g/cm^3$) than the SiMn-alloy ($\rho_{SiMn} = 6.3 g/cm^3$) as described by Hon et al. (1980). The previous experiments by Einan (2011) could be described as quenching the alloy and thus trapping the SiC grains where it is formed.

The average SiC grain size in sample 1-3 is presented in Figure 5.8. It can be seen from the figure that the angular grains increase slightly in size from 1 to 2 cycles, and increases significantly at 4 cycles. In practice this means that at 4 cycles many of the grains have grown into each other and merged. This is consistent with the visual observations of the samples.

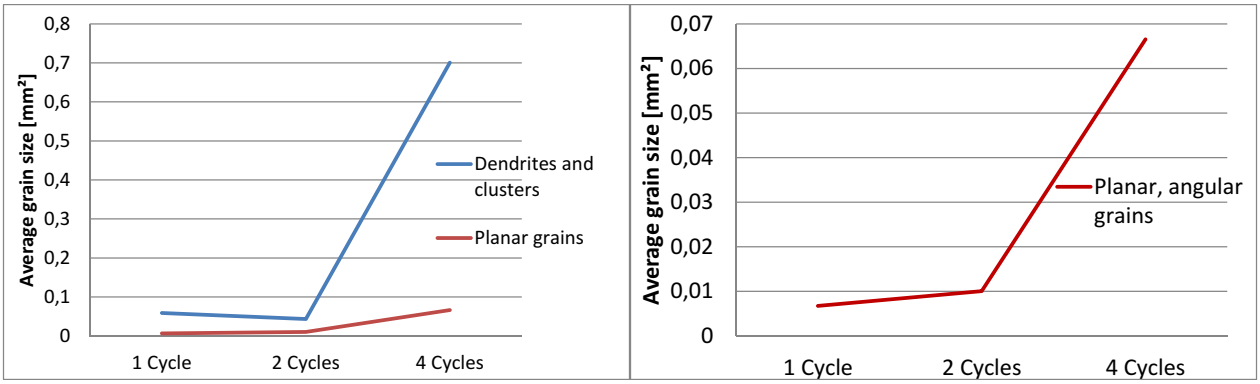

Figure 5.8: (a) The average size of SiC grains in sample 1-3 after cyclic heating and (b) a close up on the size of planar, angular grains.

5.3.2 Placement of graphite

From the density difference between graphite ($\rho_{graphite} = 2.2 g/cm^3$) and SiMn ($\rho_{SiMn} = 6.3 g/cm^3$), the graphite is expected to float up in the crucible. However, the graphite flakes in samples 4-9 did not float up to the surface. The reason for this could be that the viscosity of the samples

with graphite are higher than the one with SiC due to the higher amount of graphite than SiC particles. It is also possible that the friction on the graphite flakes are relative large or the buoyancy is fairly equal to the drag. Unfortunately the modified Stoke's Equation for non-spherical particles, presented in Equation (5.5), is only viable for particles with diameters less than $100\mu m$. The diameter of some of the graphite flakes can be seen from Figure 4.15 on page 49 and is often in the area 100-400μm and thus Stoke's Equation is not viable.

$$v_{stokes\,d_e} = \frac{d_e^2 \cdot g \cdot \left(\rho_f - \rho_s\right)}{30\mu} \tag{5.5}$$

The average graphite grain size formed in samples 4-9 is in the order of c. $0.5 - 2 \cdot 10^{-3} mm^2$ as presented in Figure 5.9, and the graphite grains at the top of the samples have an average grain size in the order of $2 - 4 \cdot 10^{-3} mm^2$. The average graphite grain size from the std. SiMn experiments increased from 1 cycle to 4 cycles while the average graphite grain size from the experiments with the HC SiMn remains unchanged after 4 cycles. This can be explained by the different chemical compositions of std. and HC SiMn. The higher amount of carbon in the HC SiMn alloy makes nucleation of graphite easier. This is because the nucleation of a spherical crystal with radius, r, is given by the number of atoms, each of volume V', and given by Equation (5.6) as described by Kurtz & Fisher (1998). When the crystal cluster reaches a critical radius, and thus a critical number of carbon atoms, a nucleus is formed.

$$r \cong \sqrt[3]{\frac{n3V'}{4\pi}} \tag{5.6}$$

It is possible that the driving force of formation of graphite as described by Hon et al. (1980) can affect the grain size of graphite. As discussed earlier the driving force of formation of graphite is larger for the HC SiMn than the std. SiMn.

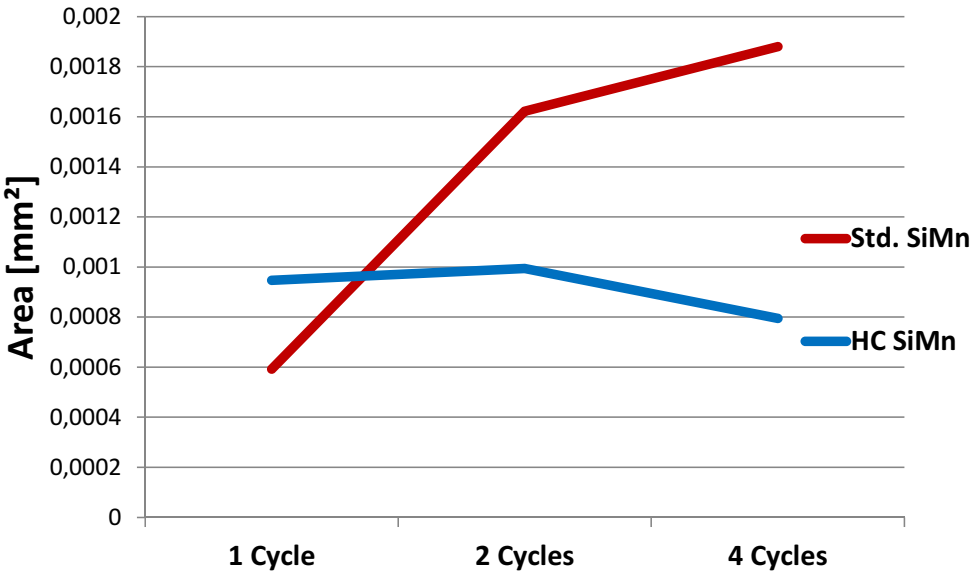

Figure 5.9: The average graphite grain size of experiments with std. SiMn (samples 4-6) and HC SiMn (samples 7-9). The average graphite grain size from the std SiMn experiments increased significantly from 1 to 4 cycles, while the average graphite grain size from the HC SiMn did not change much from 1 to 4 cycles.

5.4 Uncertainty

The uncertainty in these experiments is mainly in the deviation from expected carbon consumption and the measured carbon content in the results. Each time a sample is cooled from 1610°C the expected carbon dissolved from SiMn alloy,$\triangle C$ forms SiC or graphite. The deviation between the calculated values and the results are large, but the tendency in the results relative to one another, makes the uncertainty tolerable.

It can be seen that the observed amount of carbon after the 1 cycle experiments is not the same as the carbon amount put into the experiments. This can either be due to dissolution of carbon or it is a deviation. This uncertainty is also large, but the experiments show a good tendency relative to one another.

All the measurements have been conducted by the author, and this keeps the measurement uncertainties to as low as possible.

5.5 Formation of cavities

All samples had cavities in the middle of the sample. The cavities may have been formed due to:

- Gas formation
- Shrinkage of metal during solidification
- Wetting to graphite crucible

Gas formation is unlikely because only one of nine samples had a cavity with an opening to the surface. Gas channels would probably have formed due to escaping gas.

The metal shrank during solidification creating cracks in the alloy and between the alloy and the crucible. The wetting of the alloy to the crucible does appear to be good, due to some droplets on the crucible wall. A partly SiC layer was observed on some of the graphite crucible, and this was to be expected. When there was a SiC layer between the crucible wall and the metal these zones were very brittle, and this suggests that the SiC and metal was non-wetting.

5.6 Industrial formation of SiC and graphite

The formation of SiC can happen through the reaction between carbon and silicon in the liquid SiMn alloy. The results obtained in this report, together with the masters thesis by Davidsen (2011) give a good indication that the settling of SiC in the metal is relative slow. SiC can probably form in small amounts when the metal is tapped due to declining temperature in the furnace during tapping, however much of the SiC formed in the submerged arc furnace should be tapped together with the metal, and settle during refining or stay in the alloy.

In the submerged arc furnace the reduced metal droplets will drain down beneath the cokebed and slag layer into the metal layer as it is formed. These silicon rich SiMn droplets will probably reach equilibrium between silicon and carbon. Results obtained in this report suggest that if the alloy has a low carbon content, SiC dendrites can form. The SiC dendrites formed in the $Mn-Si-Fe-C$ alloy in this report grew much larger than the angular SiC grains, with intermediate alloy.

A higher temperature in the furnace will enhance the formation of SiC due to a larger driving force and thus a higher rate of formation of SiC. The rate of formation of graphite is affected by temperature in the same way as SiC.

The formation of graphite in the SiMn alloy can happen when the silicon content of metal is less than c. 20wt%. The results from this report suggest that the settling of graphite is slower than the settling of SiC. Most of the graphite was evenly dispersed in the alloy, however there was a 3mm area at the top with a significant higher graphite content. Graphite can probably form in small amounts when the metal is tapped due to declining temperature in the furnace during tapping, however much of the graphite formed in the submerged arc furnace should be tapped together with the metal, settle at the top during refining or stay in the alloy. Graphite has been found in production of std. SiMn. (Tangstad 2012)

Temperature fluctuations in the SiMn process is believed to be caused by the following reasons:

1. Tapping causes mainly the tapped SiMn to be cooled.
2. Normal temperature fluctuations in the furnace caused by
   (a) The change in size of the cokebed over time causes a change in resistance and thus heat in the furnace.
   (b) Active and inactive zones in the furnace. Active zones may be near the electrodes and the cokebed, while inactive zones is the low temperature zones of the furnace.
3. Operational downtime causes the furnace to go from being hot, cooling down and being heated again.

These normal, slow temperature fluctuations over time is suspected to be the cause of accumulation of SiC and graphite.

Chapter 6

Conclusion

This thesis covers a study of the formation of SiC and graphite in a $Mn-Si-Fe-C_{sat}$ system. The goal of this thesis has been to determine how temperature fluctuations affect the formation of SiC and graphite in the SiMn process. The conclusions drawn are as follows:

Experiments with three different SiMn alloys were conducted. Carbon from the crucibles dissolved into the liquid SiMn alloy to reach equilibrium between carbon and silicon. This is important because it means that coke in the submerged arc furnace can dissolve carbon into the SiMn alloy, and thus form SiC or graphite.

SiC that forms in a $Mn-Si-Fe-C$ alloy can have an interface structure of granular, angular grains and as dendrites. When SiC accumulates in the $Mn-Si-Fe-C$ system, clusters of SiC particles with intermediate SiMn alloy can form. This study shows SiC clusters that is typically a decade larger than the average SiC particle. The SiC particles settles at the top of the melt when a cooling rate of $18^{\circ}\text{C}/_{min}$ is used.

Graphite that is formed in the $Mn-Si-Fe-C$ system can have an interface structure of flakes. When the carbon content of the liquid SiMn is high enough, nucleation of new graphite grains happens instead of grain growth. The graphite flakes did not settle, but remained evenly dispersed in the SiMn alloy. This may be due to high viscosity in the melt, high friction on the graphite flakes or the buoyancy can be fairly equal to the drag of the graphite particles.

The rate of formation of ${}^{SiC}/_{graphite}$ in $Mn-Si-Fe-C_{sat}$ alloys is reduced slightly by each consecutive temperature cycle. This suggest that ${}^{SiC}/_{graphite}$ formed after the first cycles only partly dissolve into the liquid SiMn alloy to reach equilibrium.

Bibliography

Alstad, A. (2011), 'Schematics of graphite cruicible', Personal communication.

Askeland, D. R. & Phulé, P. P. (2006), *The science and engineering of materials*, international student edn, Bill Stenquist.

Aylward, G. & Findlay, T. (2008), *SI Chemical Data*, 6 edn, John Wiley & Sons Australia, Ltd.

Cantor, B. & Doherty, R. D. (1979), 'Heterogeneous nucleation in solidifying alloys', *Acta Metallurgica* **27**, 34.

Chase, M. W. (1998), *NIST-JANAF THERMOCHEMICAL TABLES*, Vol. 9 of *Journal of physical and chemical reference data, Monograph*, 4 edn, American Chemical Society and the American Institute of Physics.

Ciftja, A. (2011*a*), EPMA study of the escavation samples from Elkem Thamshavn, Technical report, SINTEF.

Ciftja, A. (2011*b*), XRD results from furnace excavation at Finnfjord AS, Technical report, SINTEF.

Davidsen, J. E. (2010), Reaction mechanisms in the silicomanganese process, Technical report, Department of Material Science and Engineering, NTNU.

Davidsen, J. E. (2011), Formation of Silicon Carbide in the Silicomanganese Process, Master's thesis, NTNU.

Davidsen, J. E. (2012), 'Cooling rate of HC SiMn + Si experiments', E-mail correspondance 29.05.2012.

DiVenuti, A. G. & Ando, T. (1998), 'A Free Dendritic Growth model Accomodating Curved Phase Boundaries and High Peclet Number Conditions', *Metallurgical and Materials Transactions A* **29A**, 3047–56.

Einan, J. (2011), Formation of SiC in liquid Mn-Si-Fe-C systems, Project work, NTNU.

Fullham, E. F. (2012), 'Ernest f. fullham, inc.'. Accessed: May 26th, 2012.
URL: *http://www.fullam.com/Light.htm*

Gruzleski, J. E. (1975), 'On the growth of sperulitic graphite in nodular cast iron', *Carbon* **13**, 167–173.

Harris, G. L. (1995), *Properties of silicon carbide*. Chapter 2.

Hoel, E. G. (1998), Structures and phase relations in silicomanganese alloys, PhD thesis, NTNU.

Hon, M. H., Davis, R. F. & Newbury, D. E. (1980), 'Self-diffusion of 30Si in polycrystalline beta-SiC', *Journal of Materials Science* **15**, 2073–80.

Ishihara, K., Maeda, M. & Shingu, P. (1985), 'The nucleation of metastable phases from undercooled liquids', *Acta Metallurgica* **33**(12), 2113 – 2117.
URL: *http://www.sciencedirect.com/science/article/pii/0001616085901725*

Ivantsov, V. & Dmitreiev, V. (1998), 'Dissolution and growth of silicon carbide crystals in melt-solutions.', *Materials Science Forum* **264-268**, 73–76.

Krishnarao, R. V. & Subrahmanya, J. (1995), 'Formation of SiC from rice husk silica-carbon black mixture: Effect of rapid heating', *Ceramics International, 22* pp. 489–492.

Kurtz, W. & Fisher, D. (1998), *Fundamentals of Solidification*, TRANS TECH PUBLICATIONS.

Li, C., Huang, J., Cao, L. & Lu, J. (2009), 'Synthesis of SiC nanowires from gaseous SiO and pyrolyzed bamboo slices', *Journal of Physics: Conference Series* **152**.

Lindstad, L. H. (2002), Recrystallization of silicon carbide, PhD thesis, NTH, Trondheim.

Löser, W. & Herlach, D. M. (1992), 'Theoretical Treatment of the Solidification of Undercooled Fe-Cr-Ni Melts', *Metallurgical and Materials Transactions A* **23A**, 1585–91.

Nelson, W. E., Halden, F. A. & Rosengreen, A. (1966), 'Growth and Properties of SiC Single Crystals', *Journal of Applied Physics* **37**, 333 – 336.

Olsen, S. E. (2001), Fundamental principles of silicomanganese production, Technical report, SINTEF.

Olsen, S. E. & Tangstad, M. (2004), Silicomanganese production - process understanding, *in* 'INFACON X'.

Olsen, S. E., Tangstad, M. & Lindstad, T. (2007), *Production of Manganese Ferroalloys*, Tapir Academic Press.

Ray, H. S. (1993), *Kinetics of Metallurgical Reactions*, INTERNATIONAL SCIENCE PUBLISHER.

Roine, A. (2002), 'HSC chemistry 5.11'.

Sandvik, K. L., Digre, M. & Malvik, T. (1999), *Oppredning av primære og sekundære råstoffer*, Trondheim: Tapir.

Tangstad, M. (2012), Personal communication 06.06.2012.

Tanso (2011), 'Characteristic chart of ig-15', E-mail correspondance 12.09.2011.

Thompson, C. & Spaepen, F. (1983), 'Homogeneous crystal nucleation in binary metallic melts', *Acta Metallurgica* **31**(12), 2021 – 2027.
URL: *http://www.sciencedirect.com/science/article/pii/0001616083900196*

Tuset, J. K. & Sandvik, J. (1970), The Solubility of Carbon in Ferrosilicomanganese at 1330-1630°C, Technical report, SINTEF.

WashingtonMills (2012), 'Datasheet no. 1'. Accessed: April 16th, 2012.
URL: *http://www.washingtonmills.no/*

Zhou, H. & Singh, R. N. (1995), 'Kinetics model for the growth of silicon carbide by the reaction of liquid silicon with carbon', *Joinal of the American Ceramic Society, 78 (9)* pp. 2456–62.

Appendix A

Microscope pictures

The microscope pictures are enlarged and added in this appendix. Samples 1-3 are presented in Figure A1-A9. Samples 4-6 are presented in Figure A10-A18 and samples 7-9 are presented in Figures A19-A27. The microscope pictures are presented in the same order of appearance as in the results chapter. First is the top of sample 1-3 presented in Figure A1-A3, then the bulk and so on.

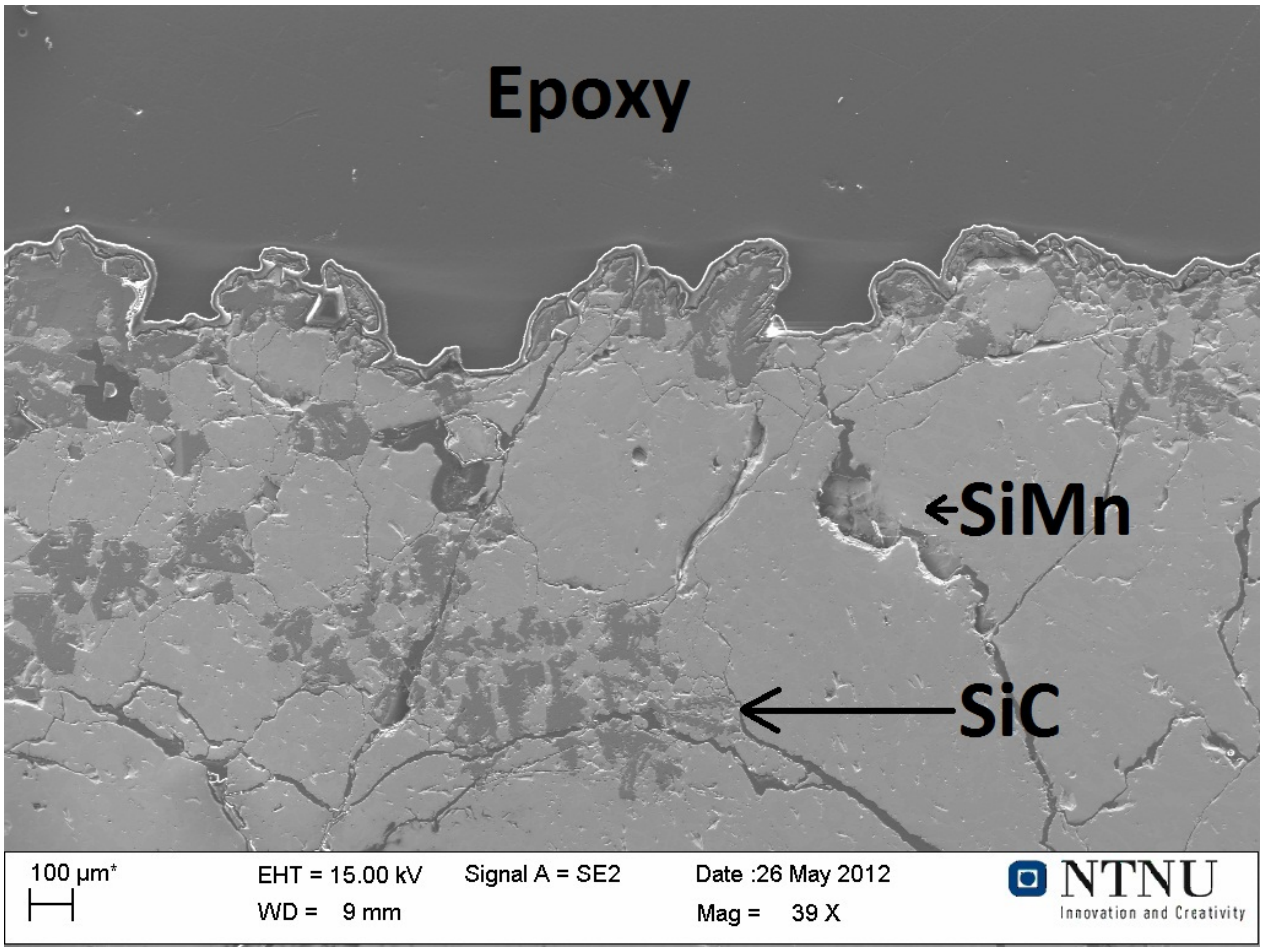

Figure A.1: 1 cycles, top of sample 1

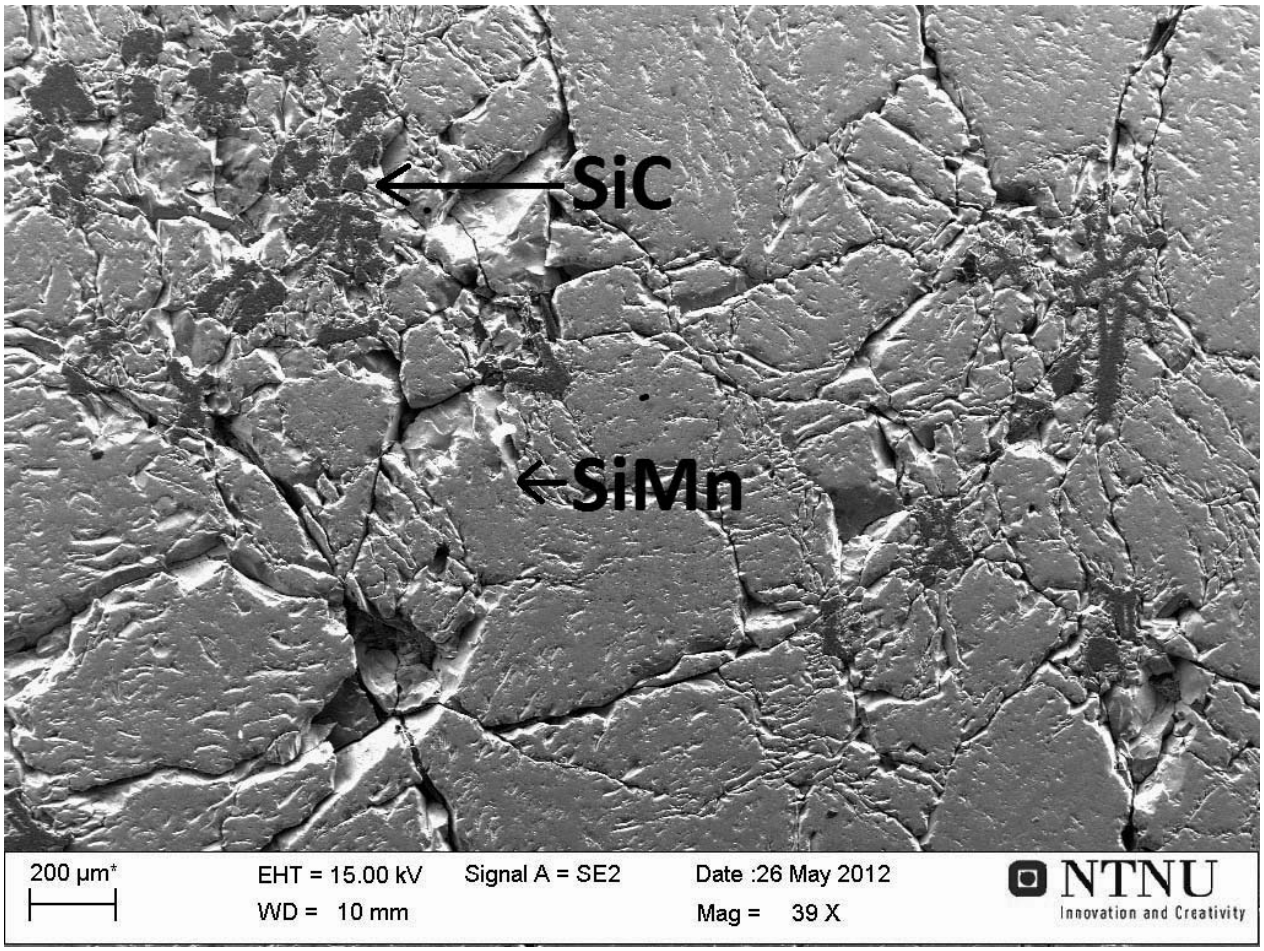

Figure A.2: 2 cycles, top of sample 2

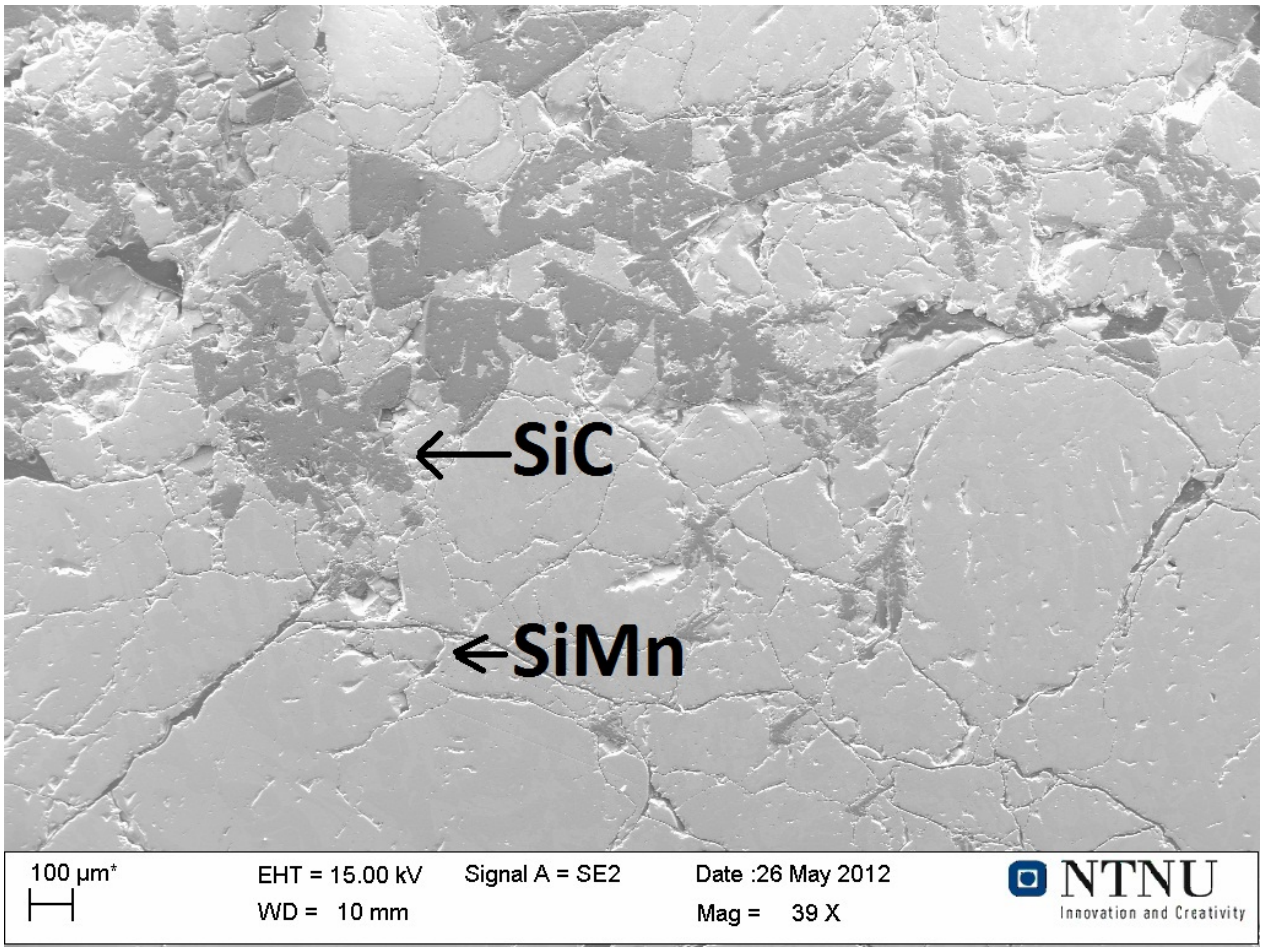

Figure A.3: 4 cycles, top of sample 3a

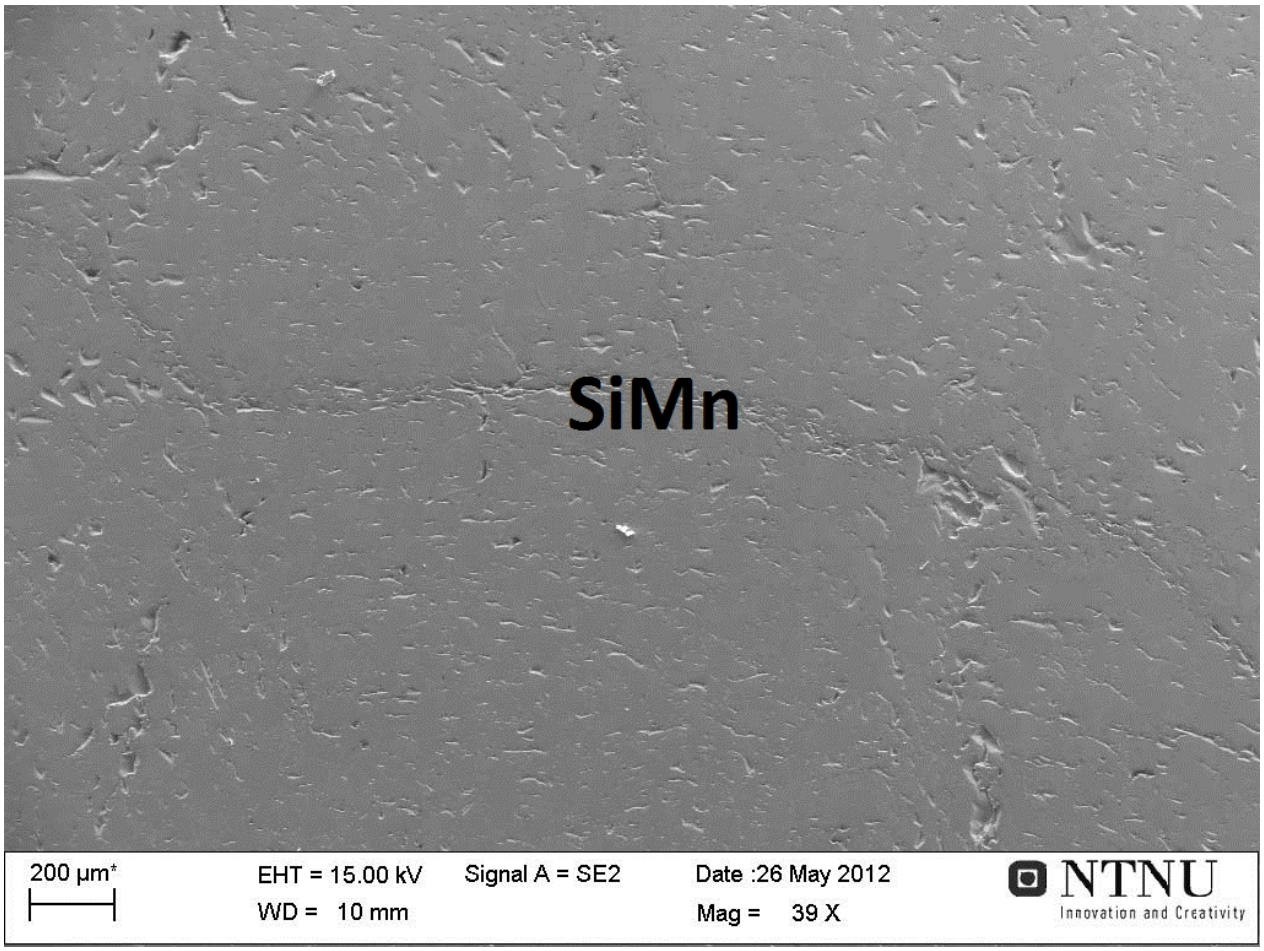

Figure A.4: 1 cycles, bulk of sample 1

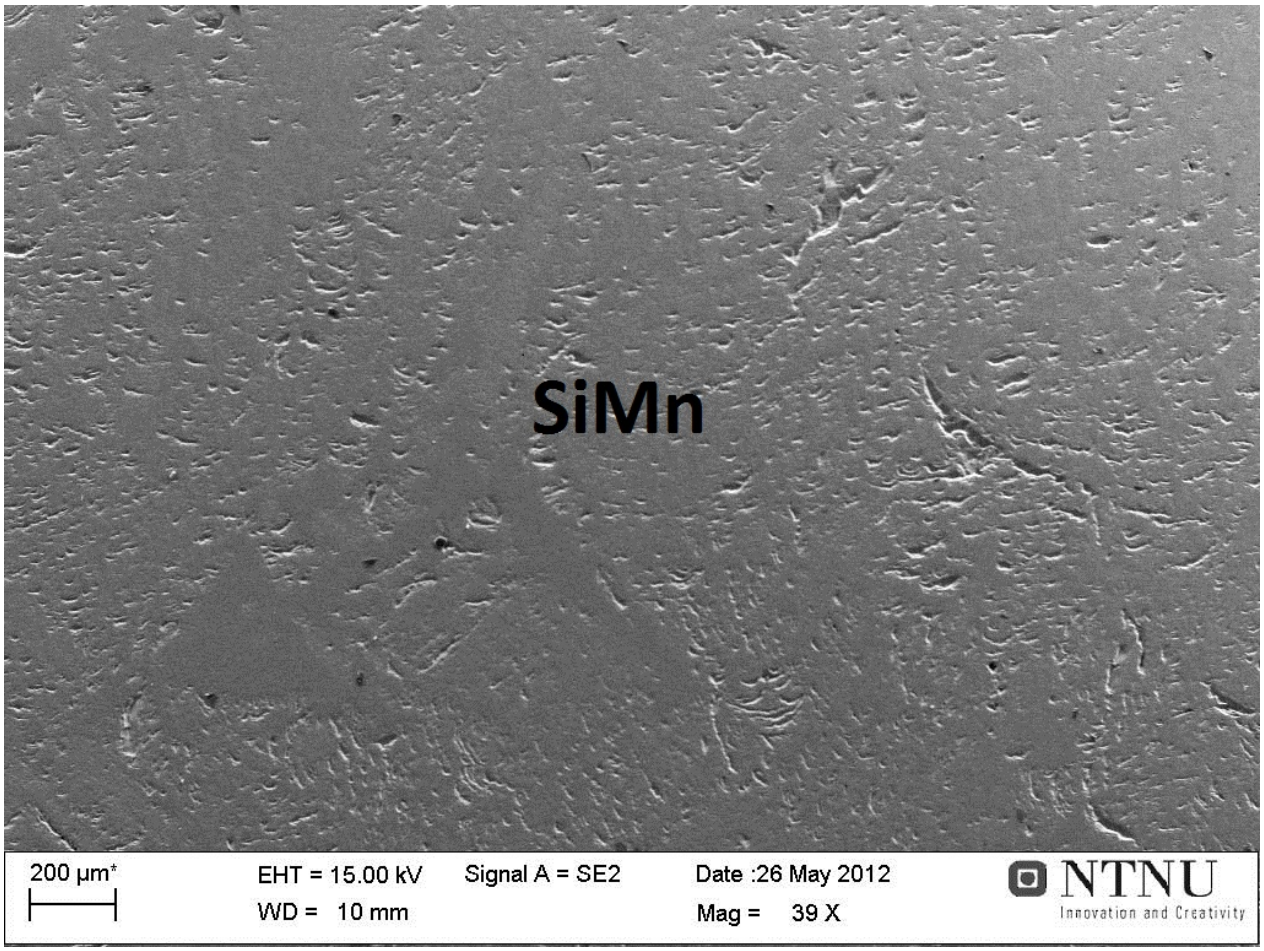

Figure A.5: 2 cycles, bulk of sample 2

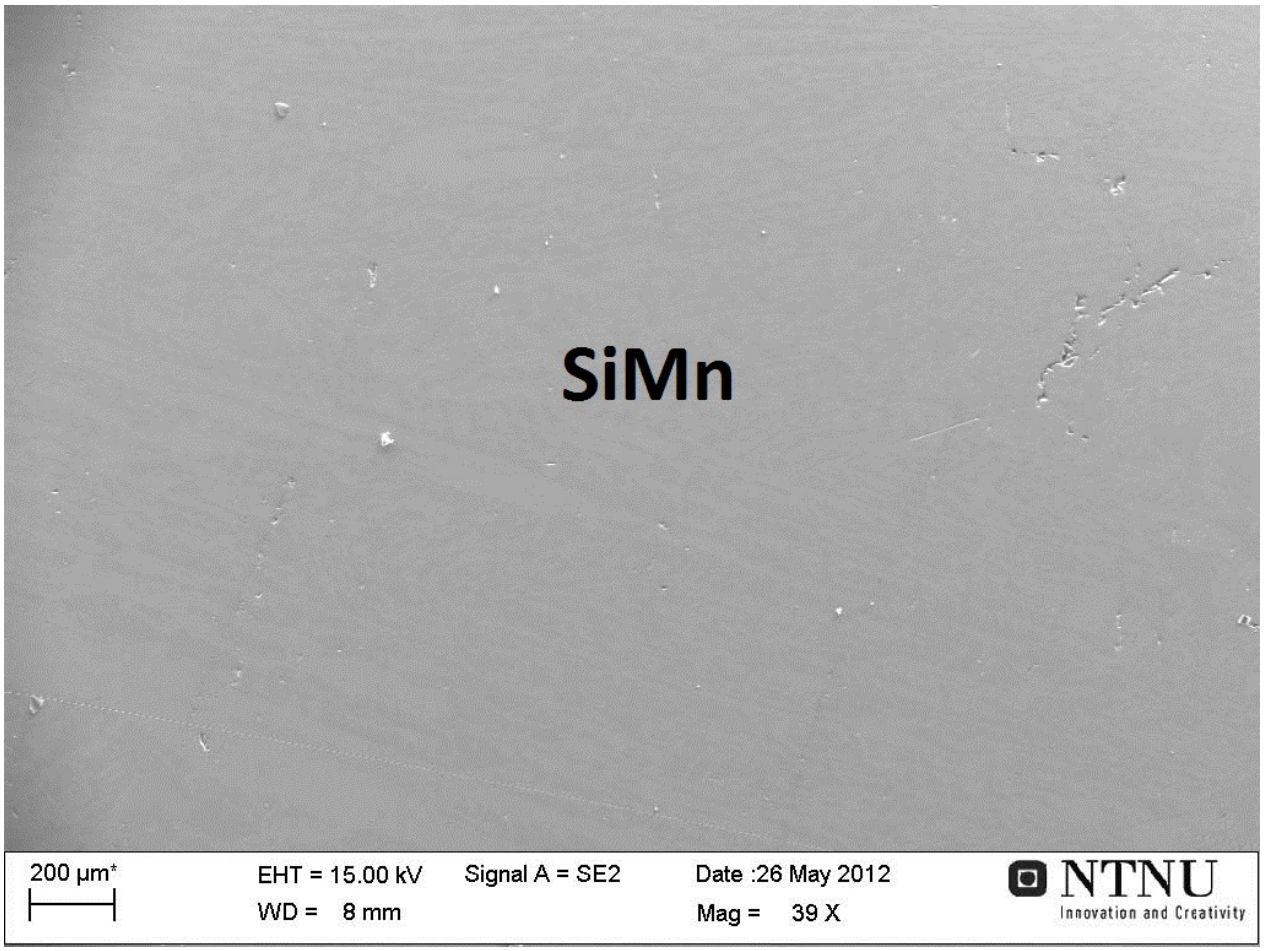

Figure A.6: 4 cycles, bulk of sample 3

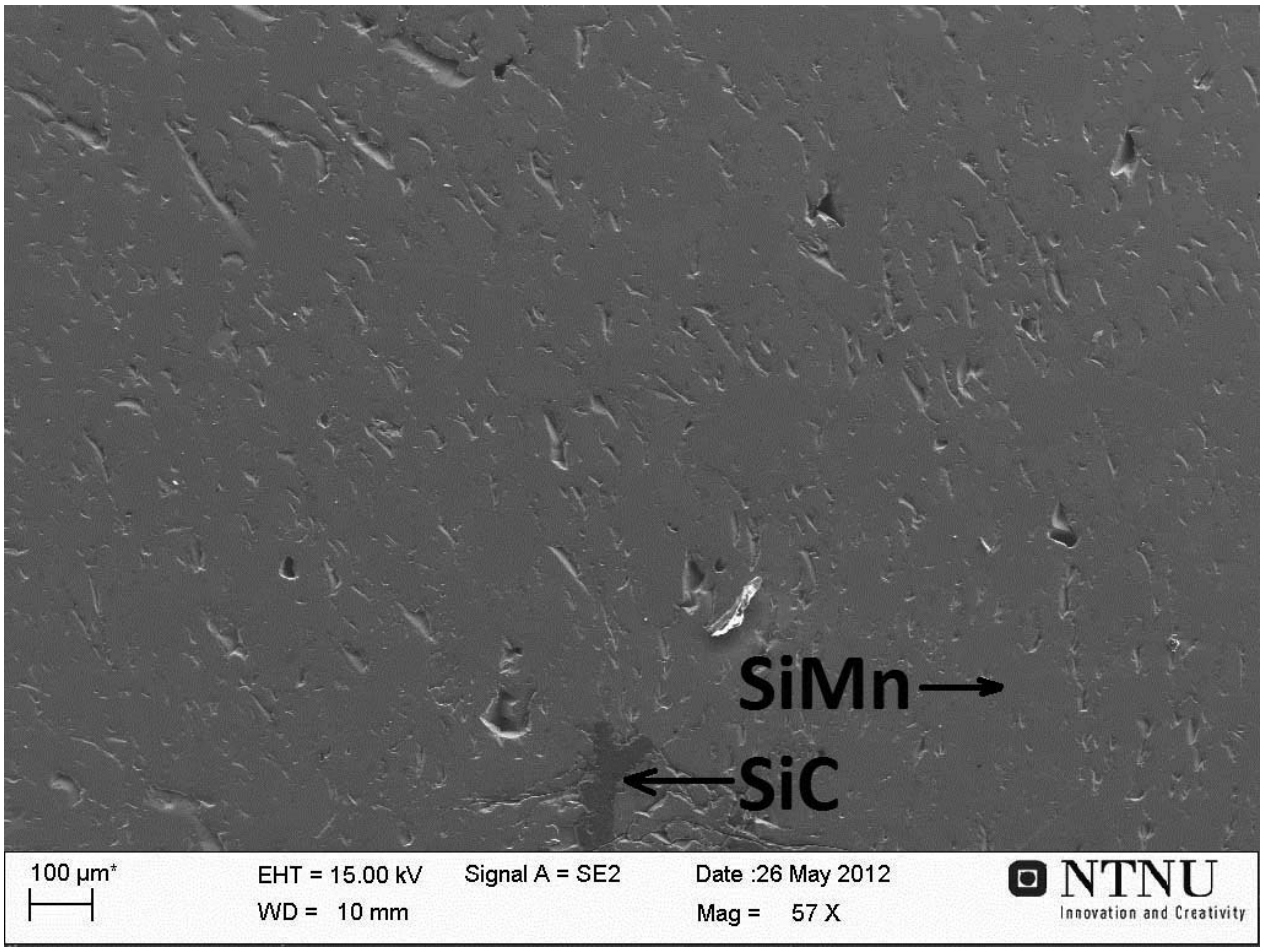

Figure A.7: 1 cycles, bottom of sample 1

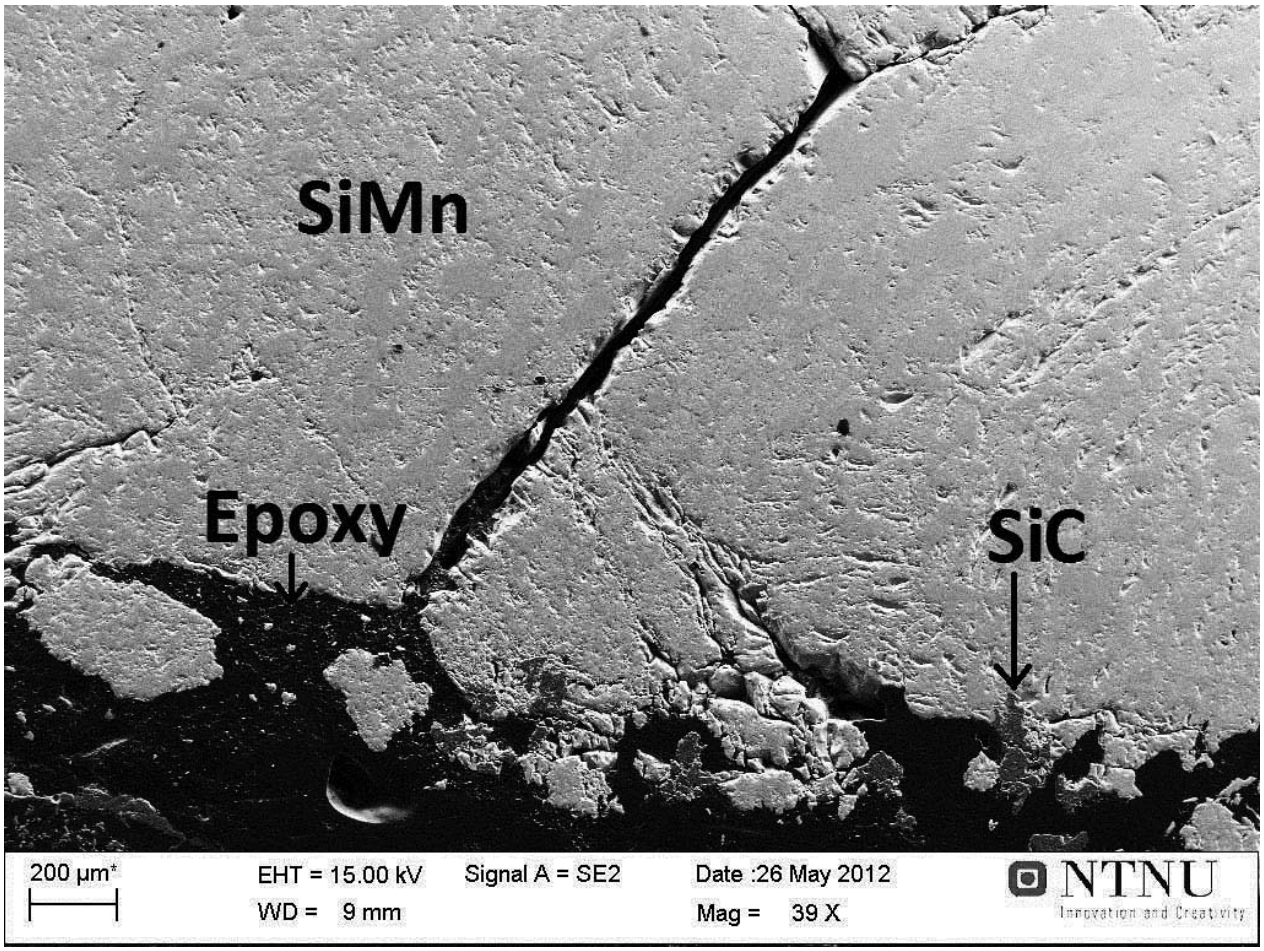

Figure A.8: 2 cycles, bottom of sample 2

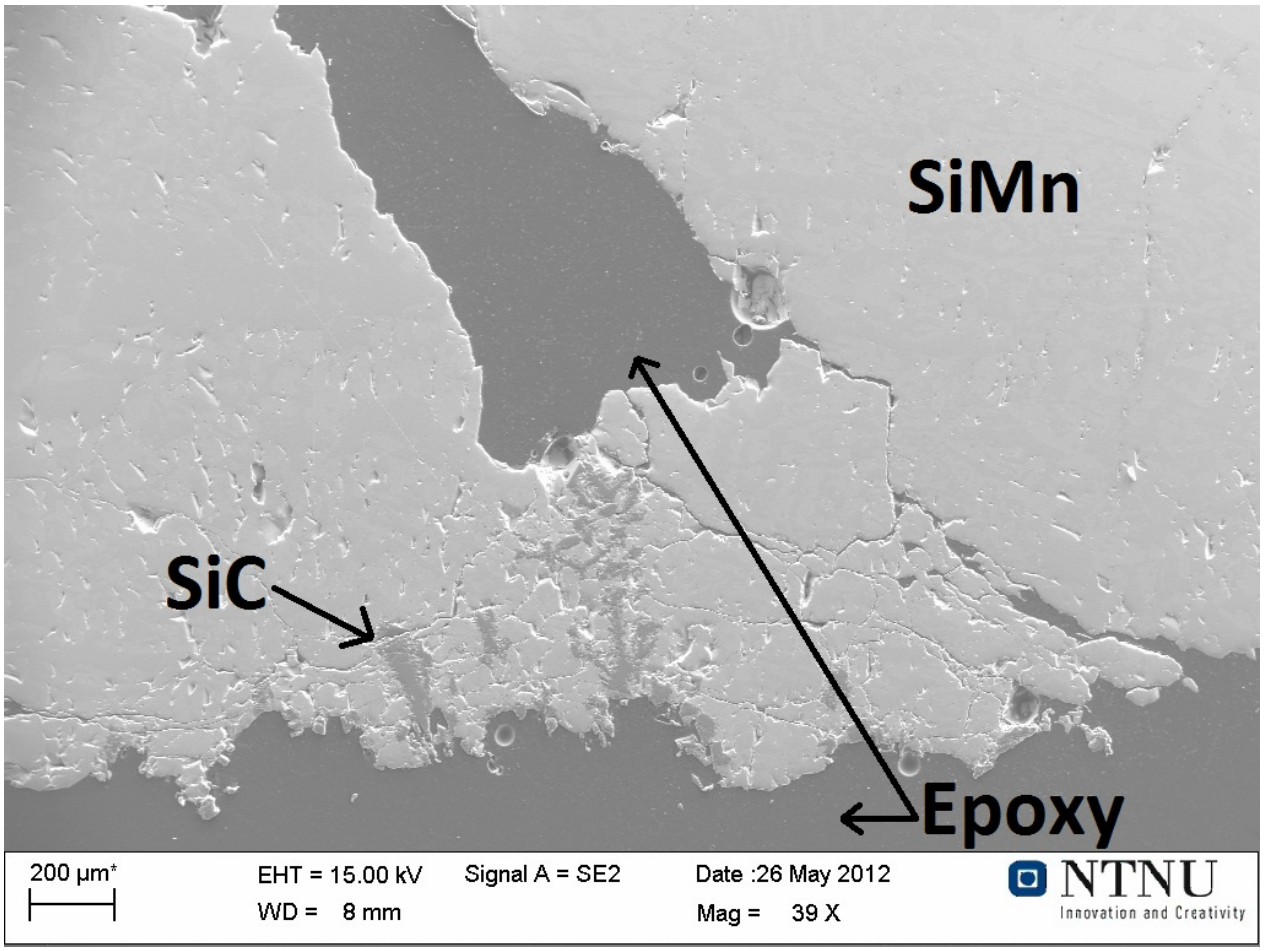

Figure A.9: 4 cycles, bottom of sample 3a

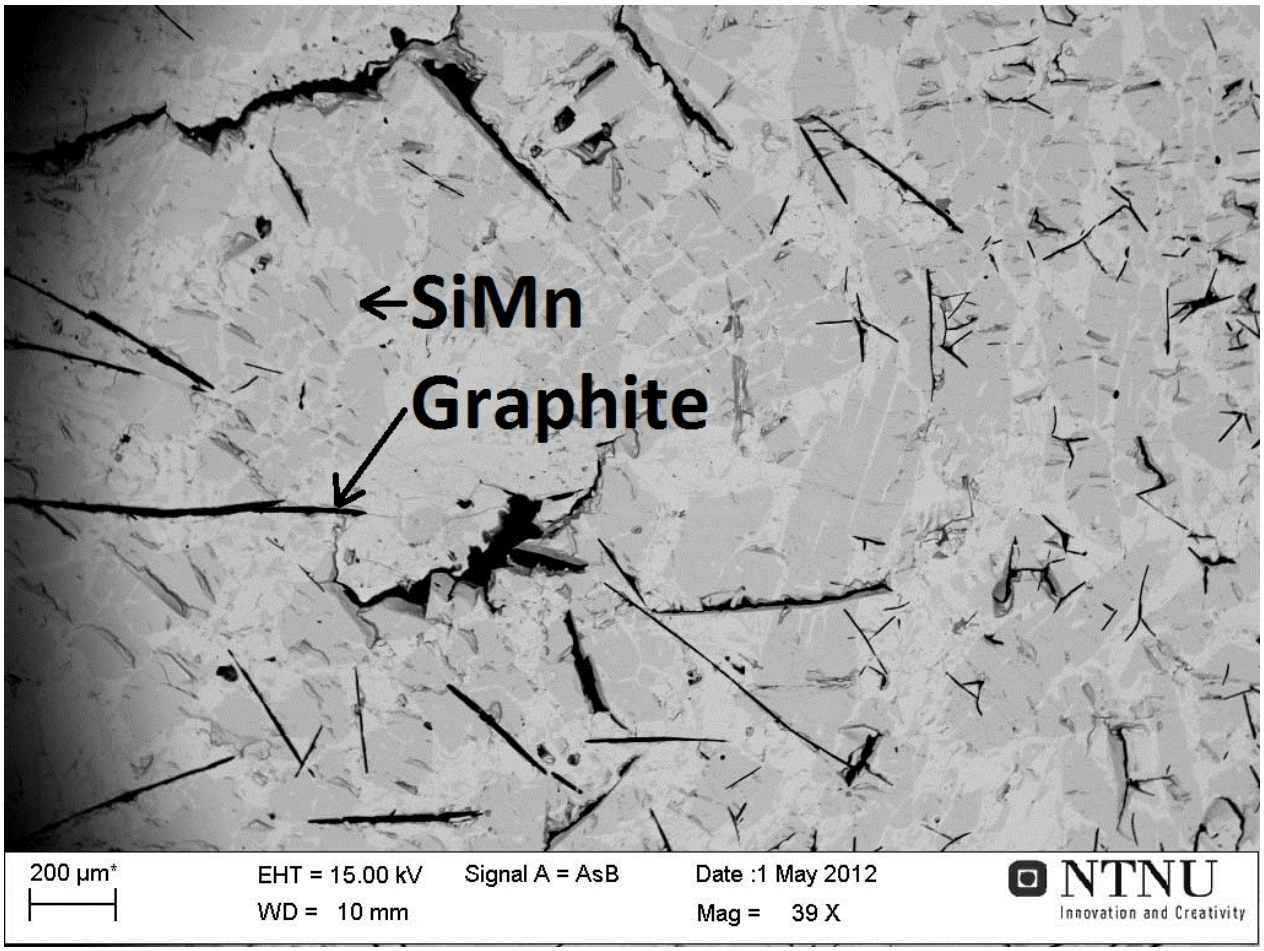

Figure A.10: 1 cycle, top of sample 4

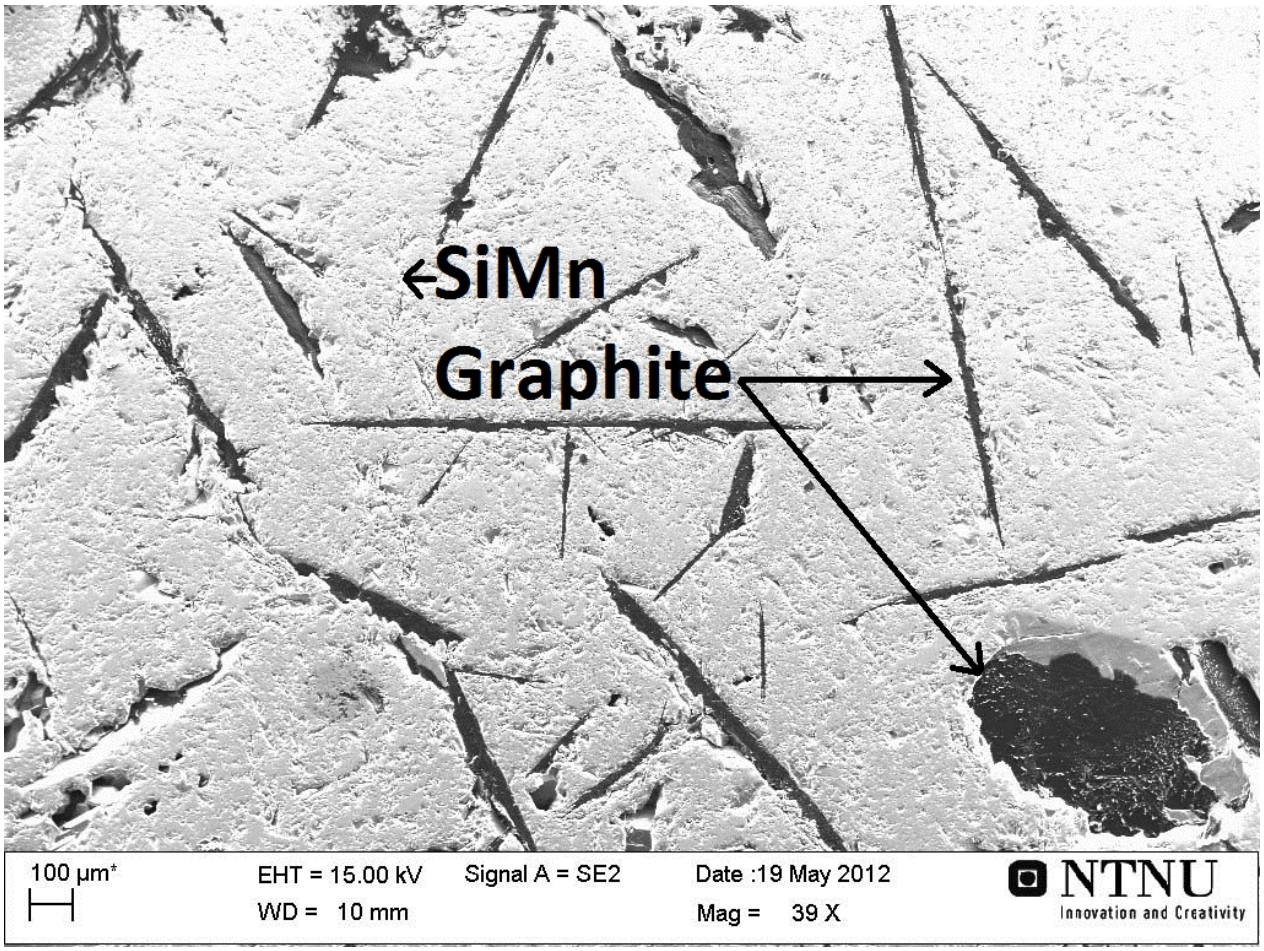

Figure A.11: 2 cycle, top of sample 5

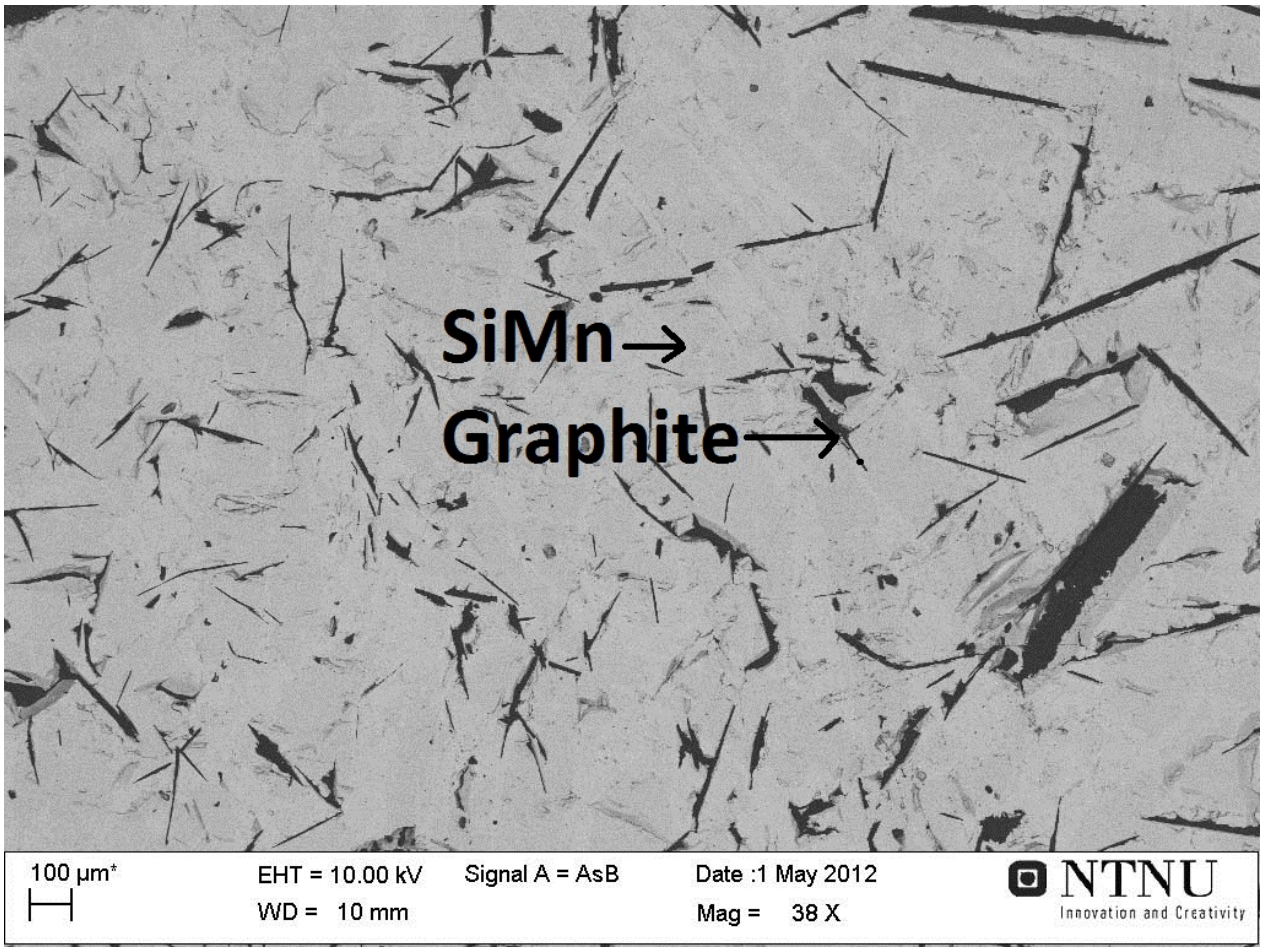

Figure A.12: 4 cycle, top of sample 6

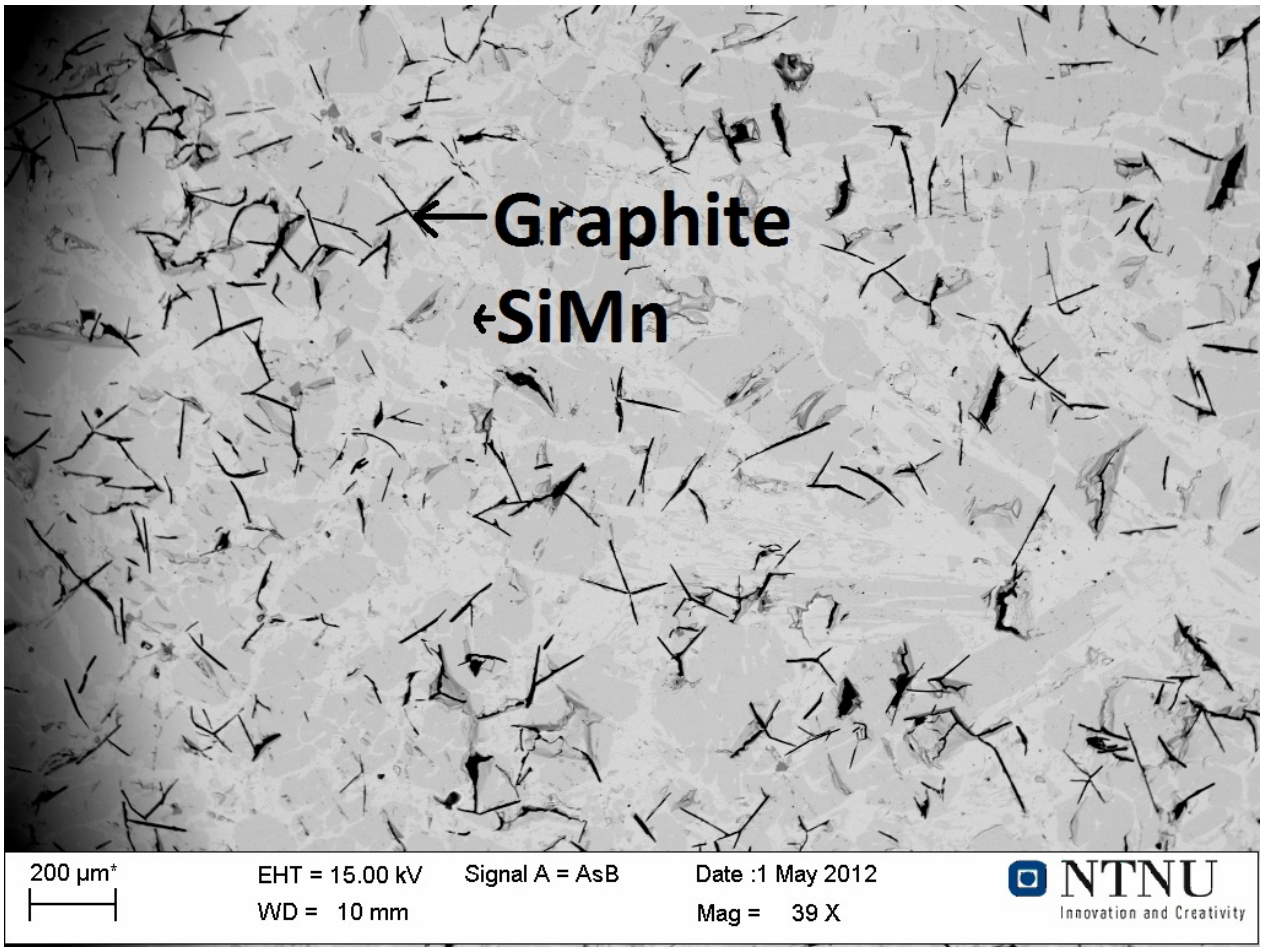

Figure A.13: 1 cycle, bulk of sample 4

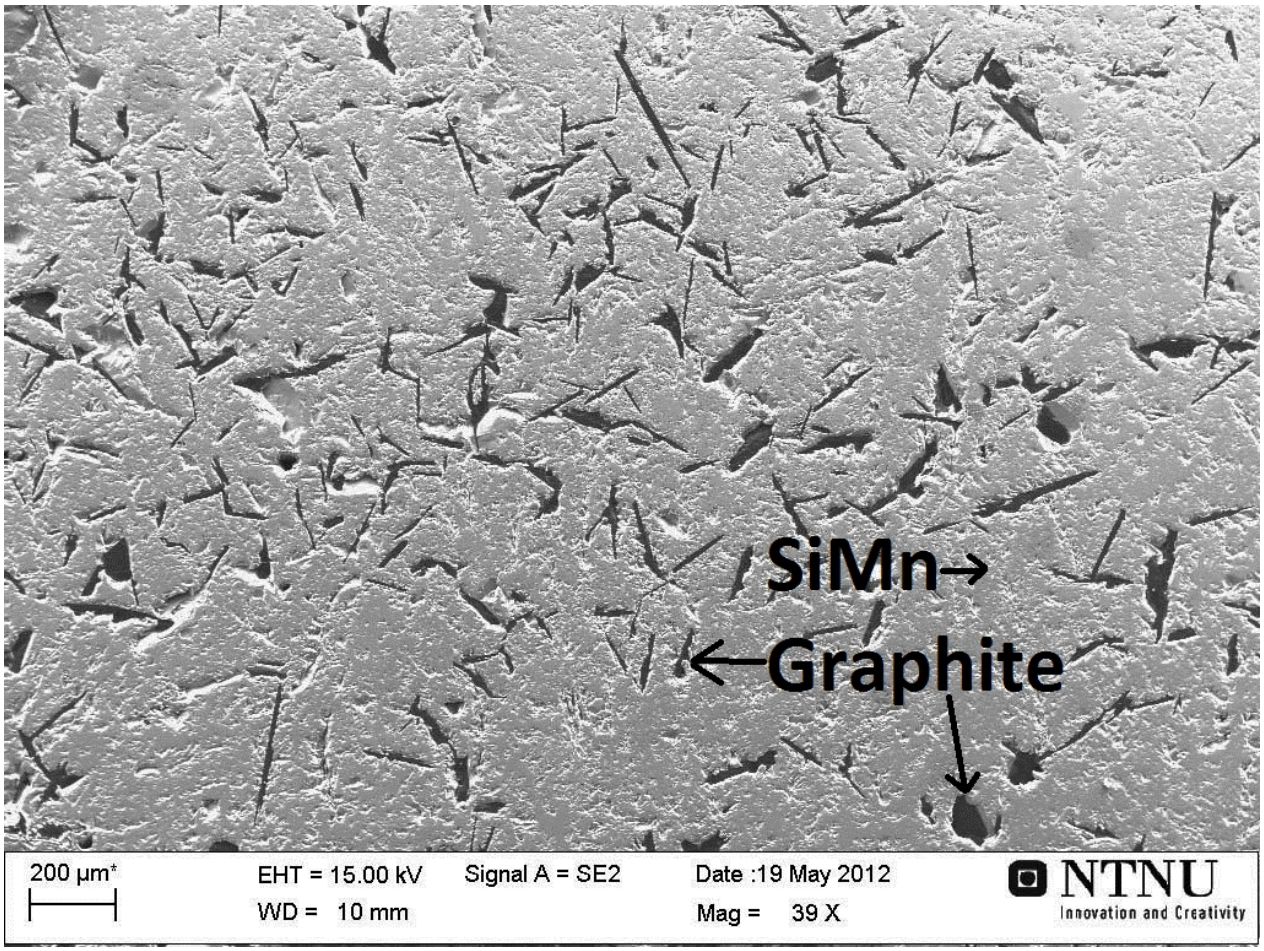

Figure A.14: 2 cycles, bulk of sample 5

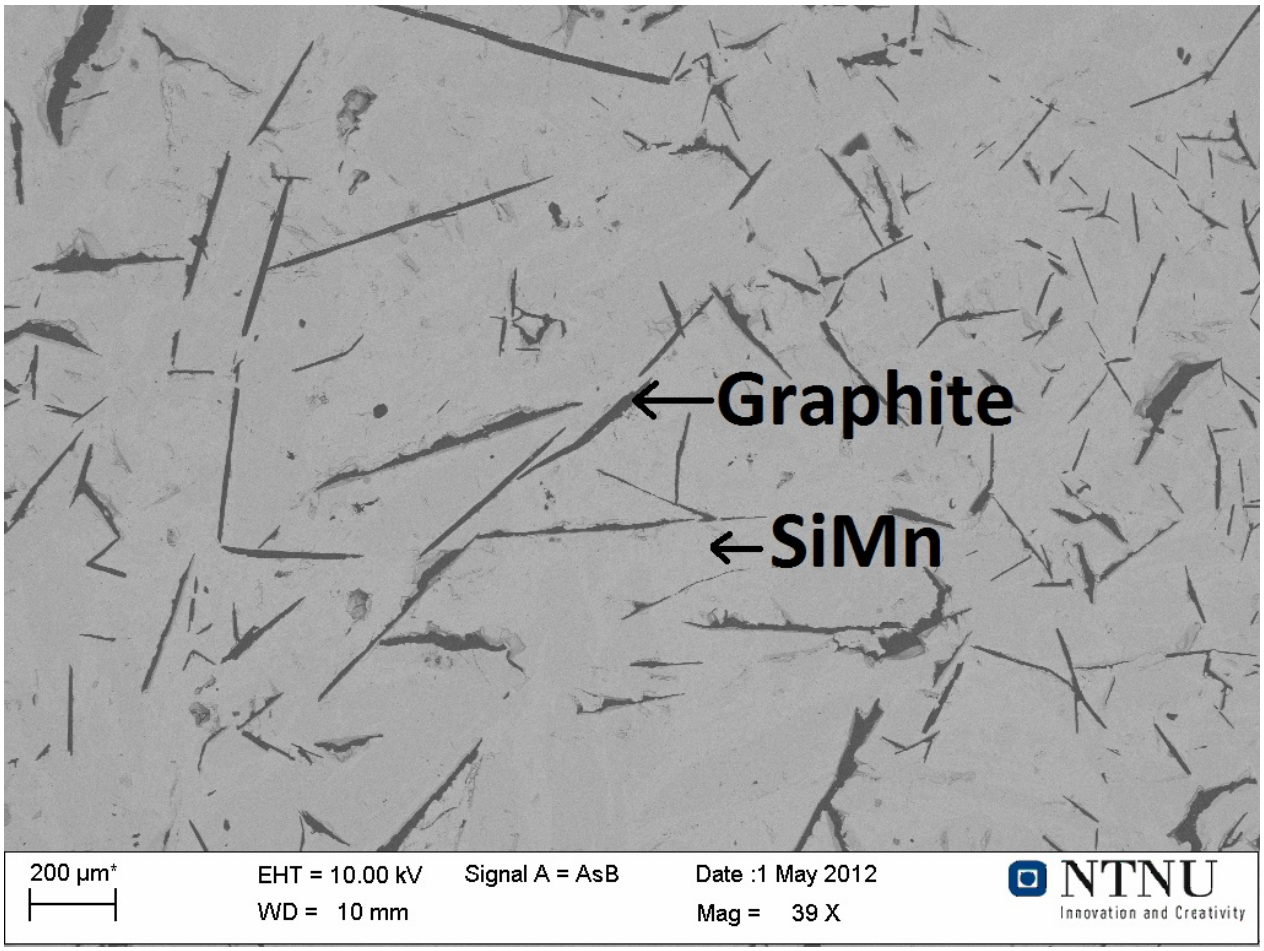

Figure A.15: 4 cycles, bulk of sample 6

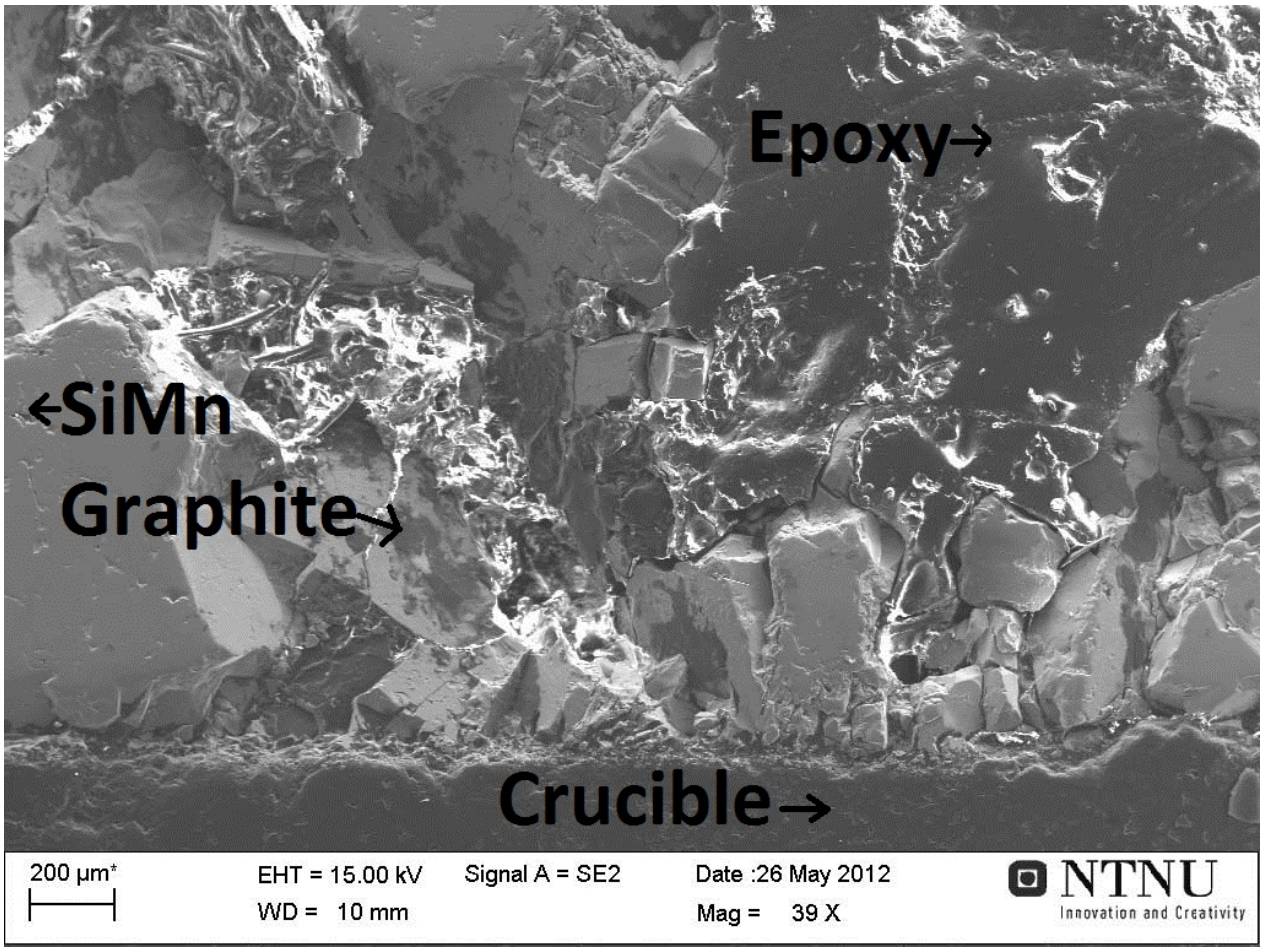

Figure A.16: 1 cycle, bottom of sample 4

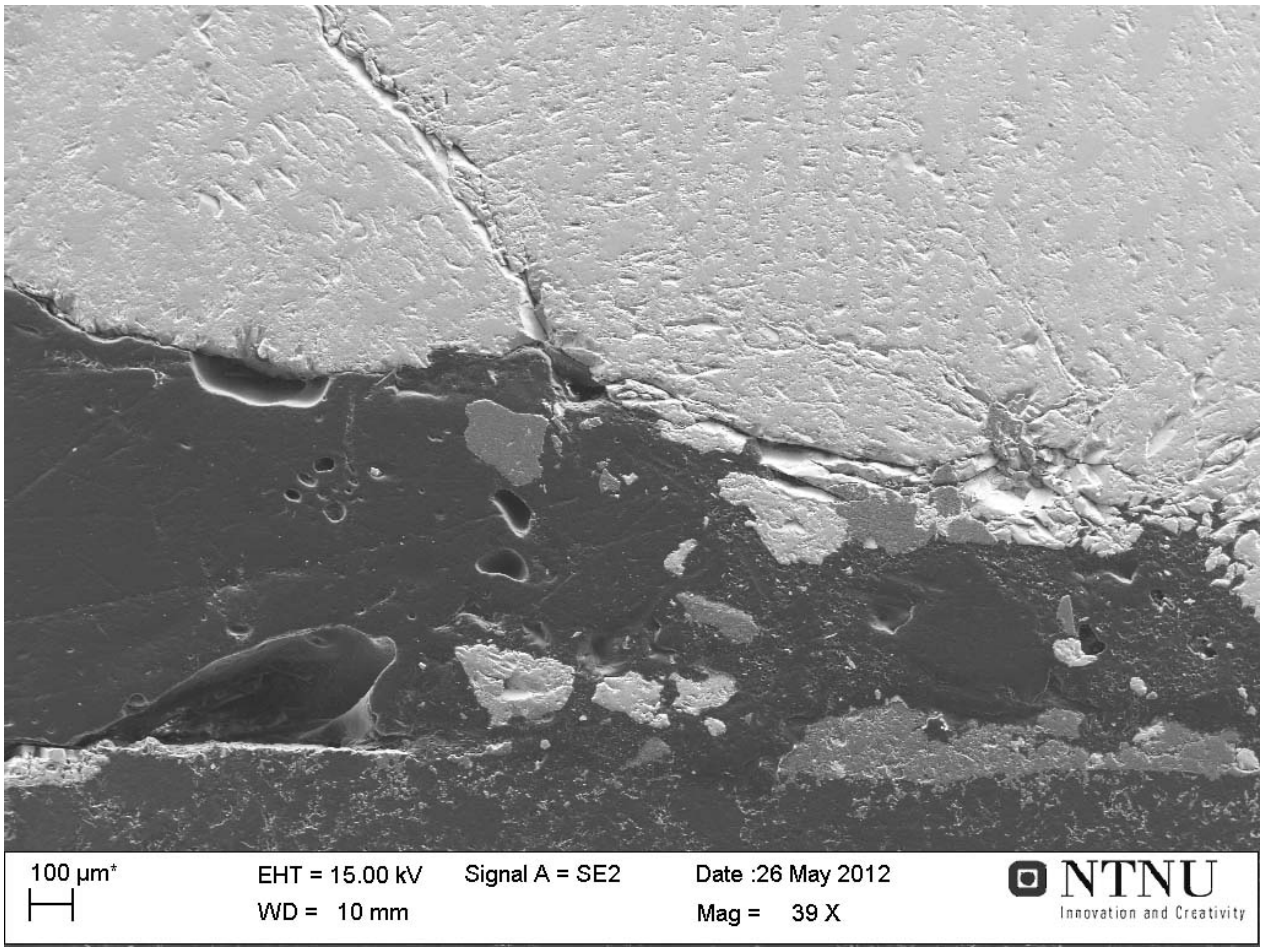

Figure A.17: 2 cycles, bottom of sample 5

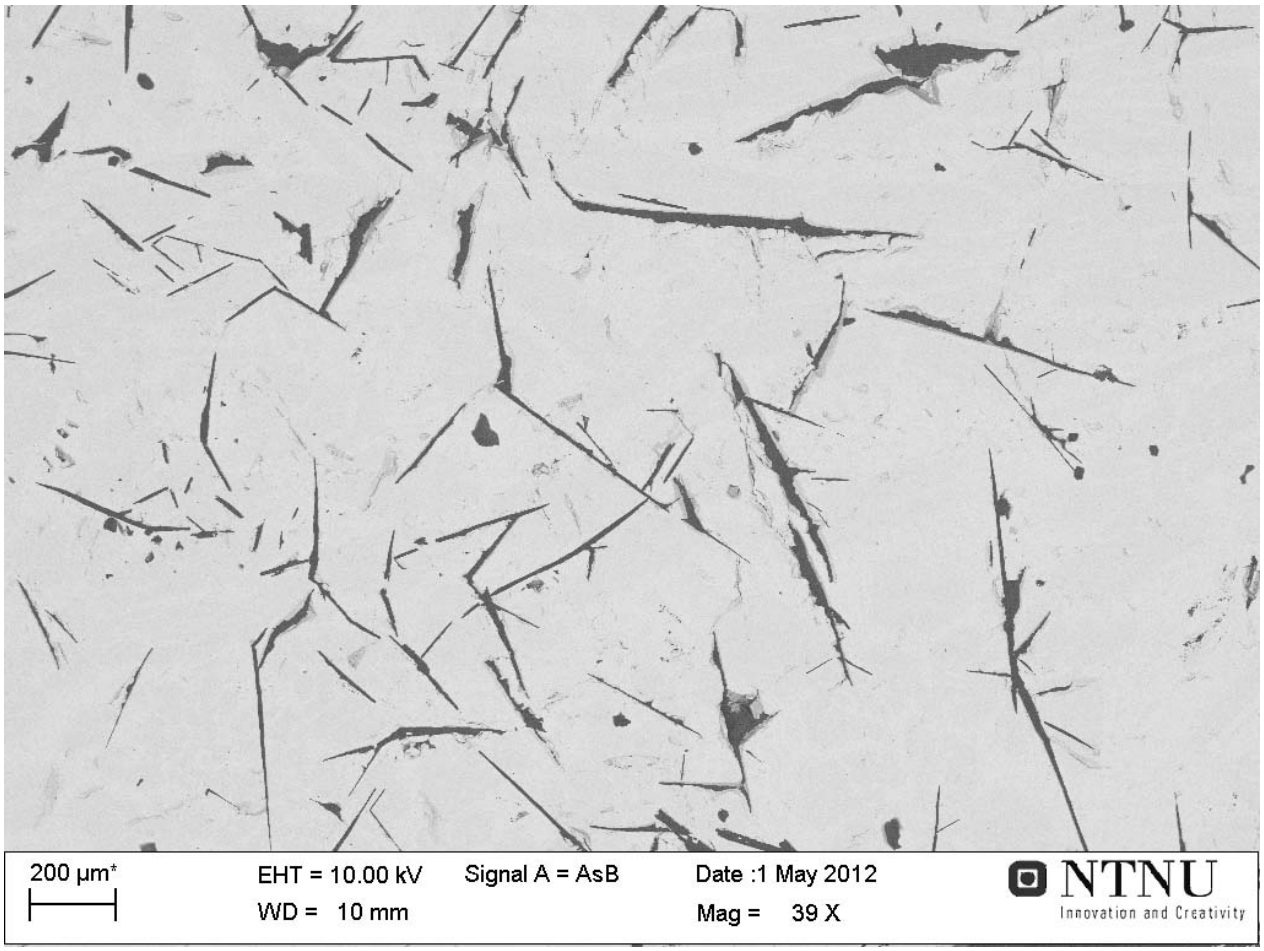

Figure A.18: 4 cycles, bottom of sample 6

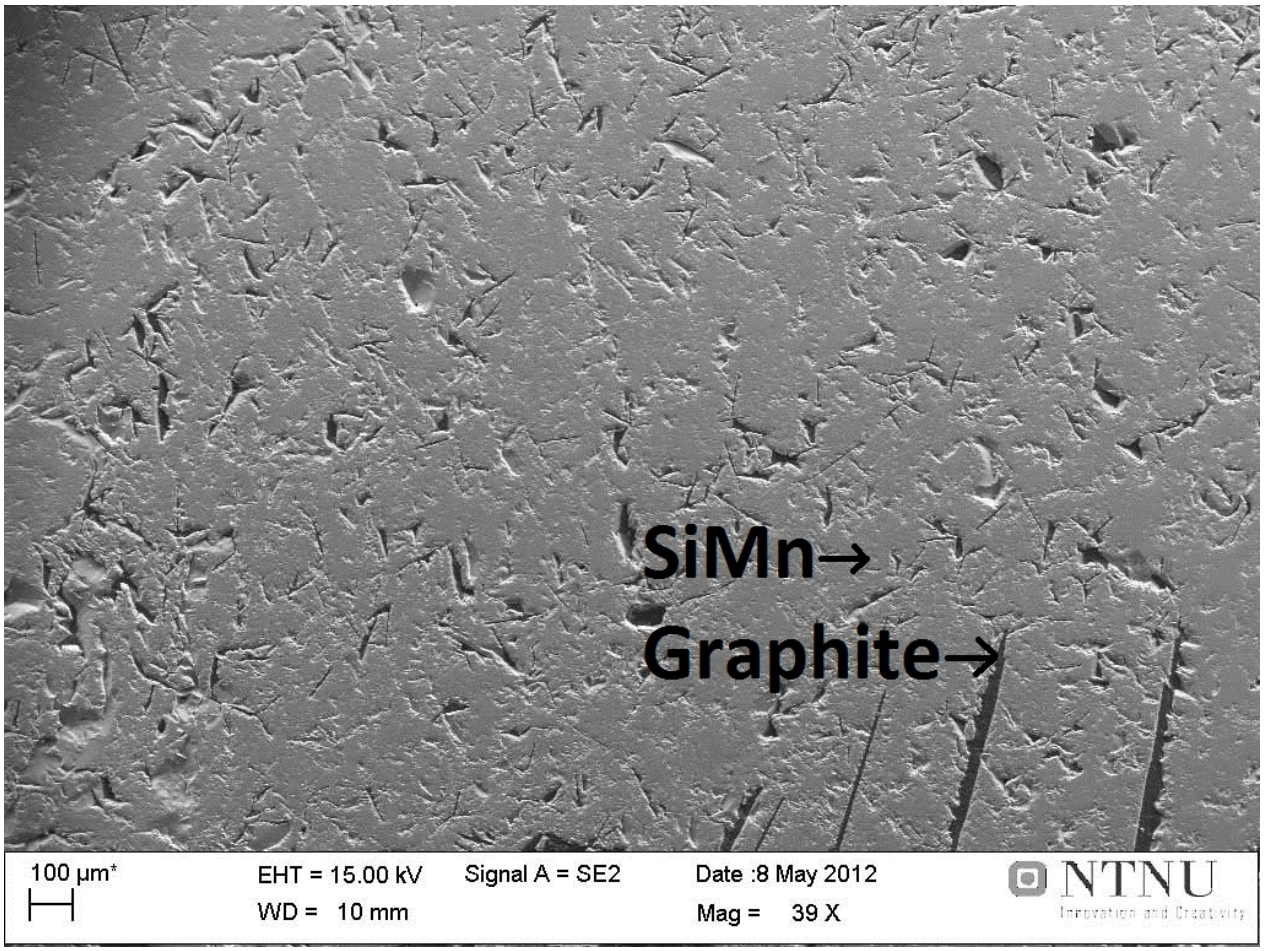

Figure A.19: 1 cycle, top of sample 7

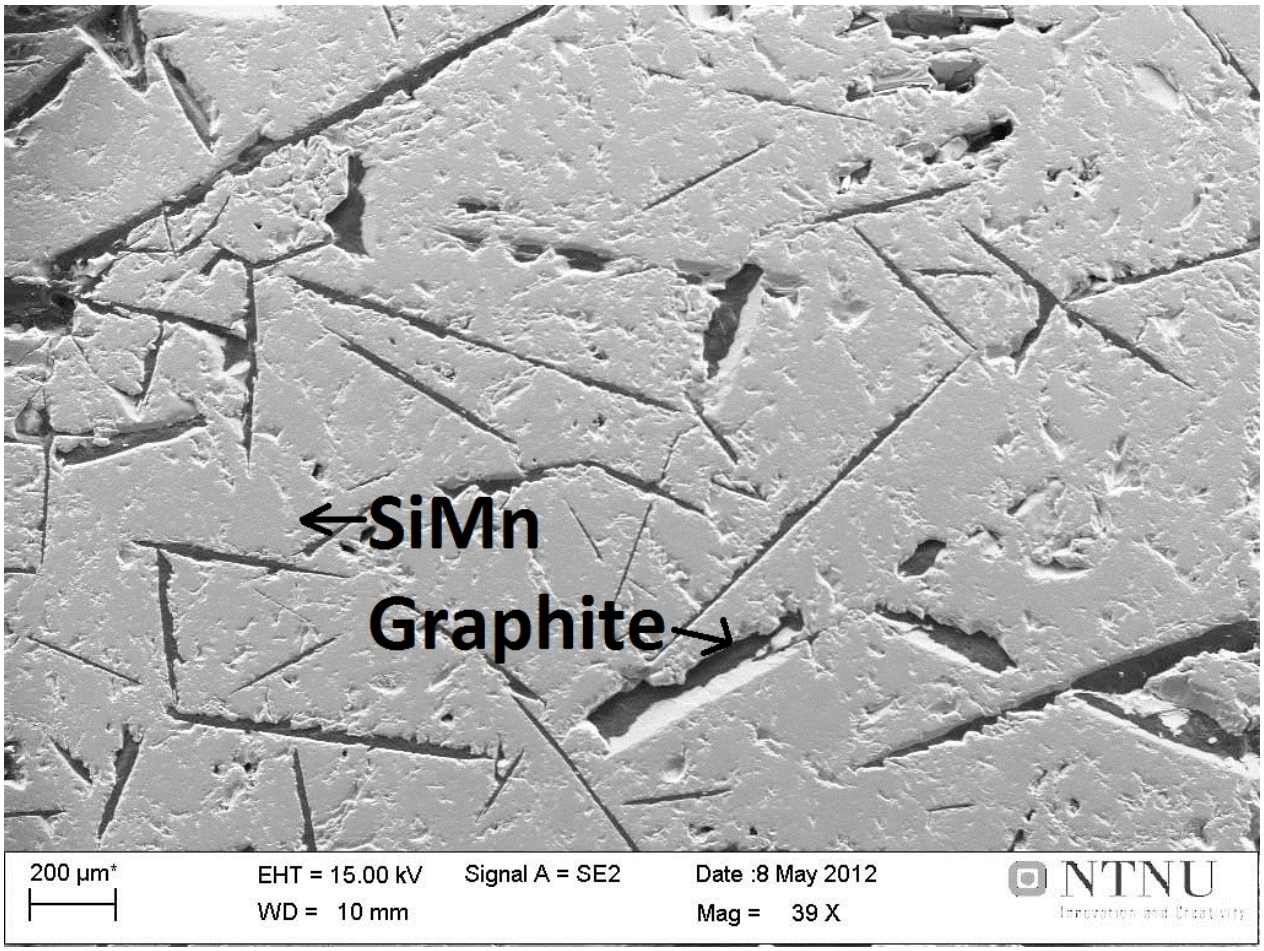

Figure A.20: 2 cycles, top of sample 8

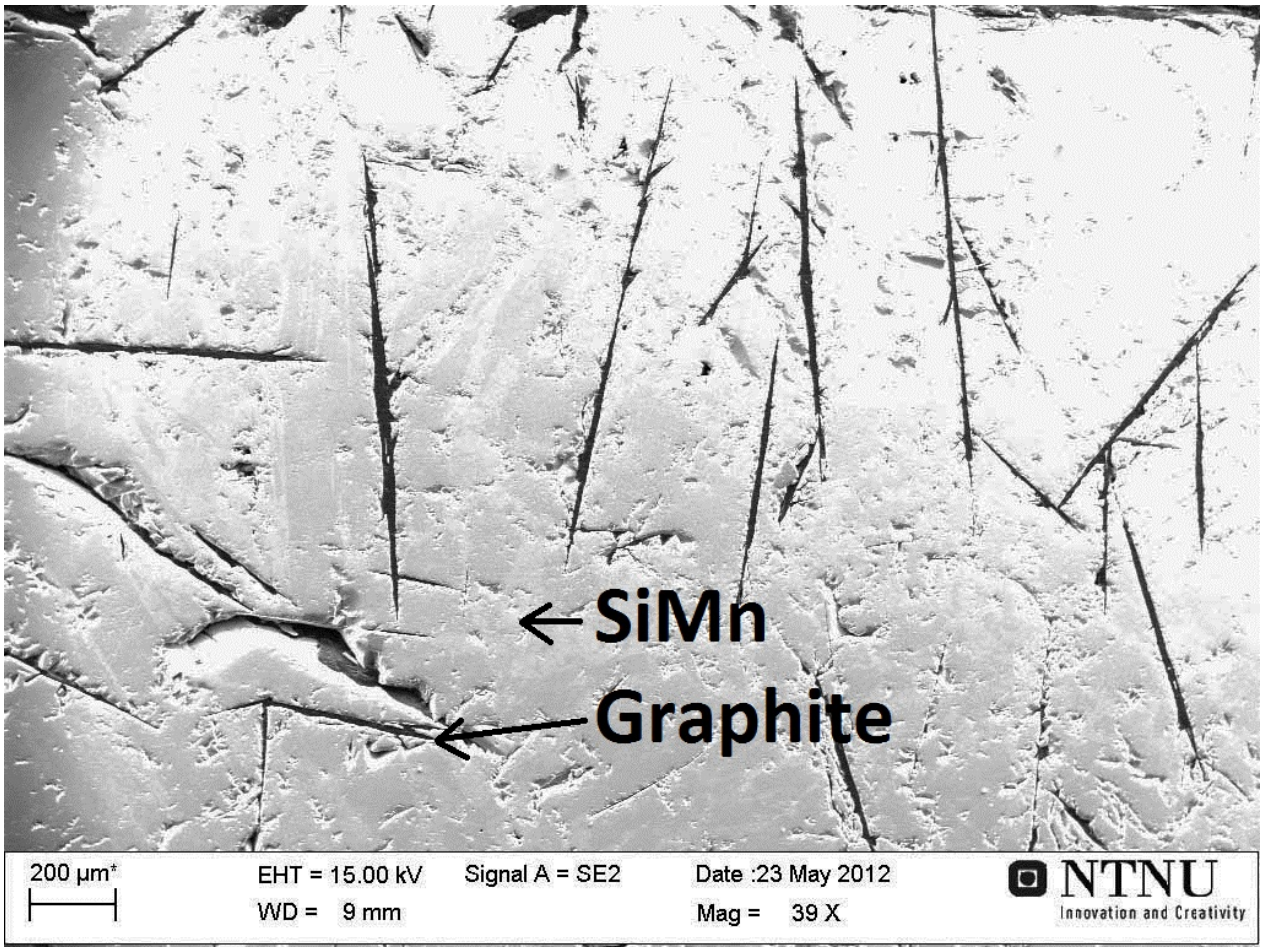

Figure A.21: 4 cycles, top of sample 9

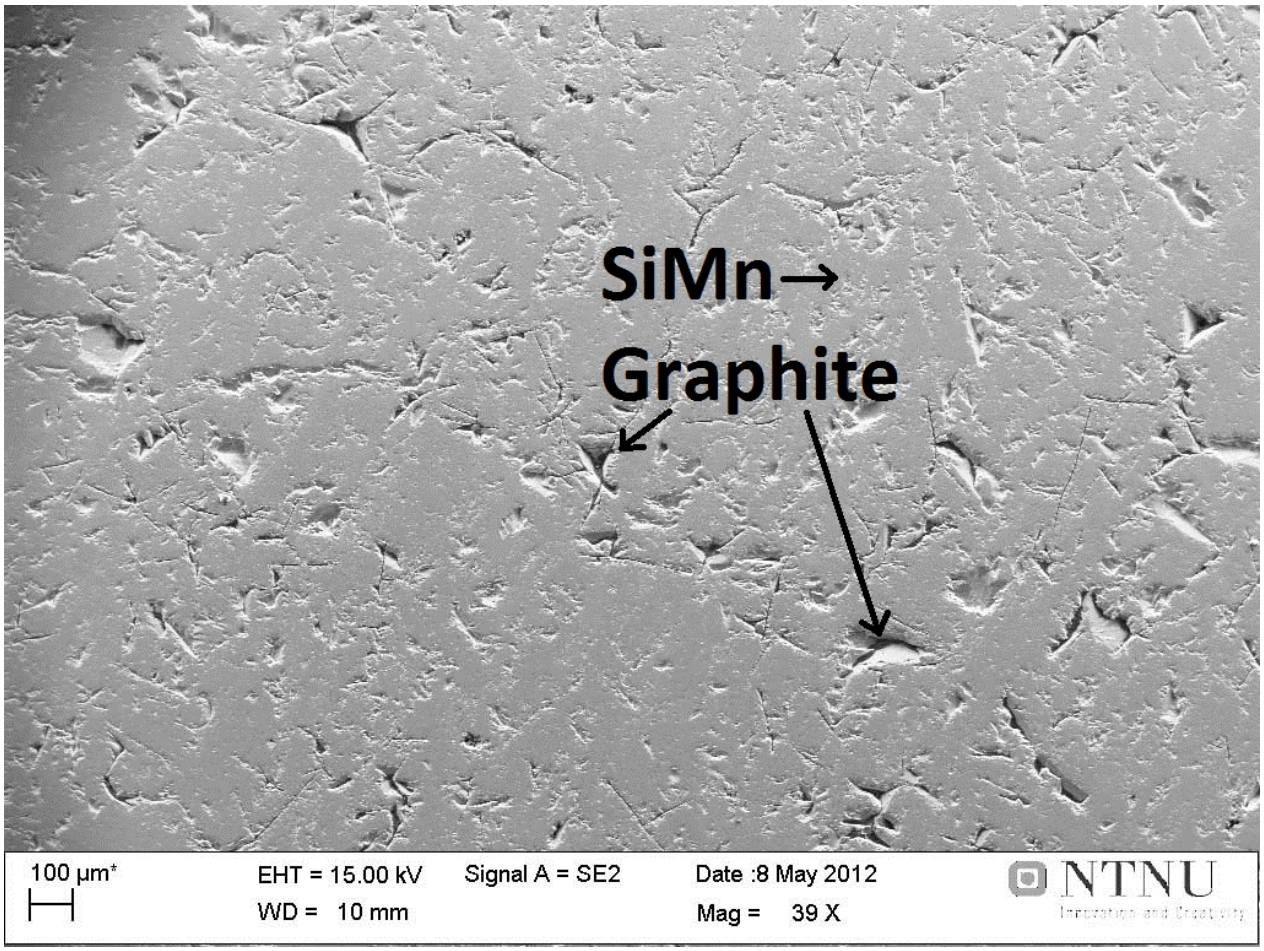

Figure A.22: 1 cycle, bulk of sample 7

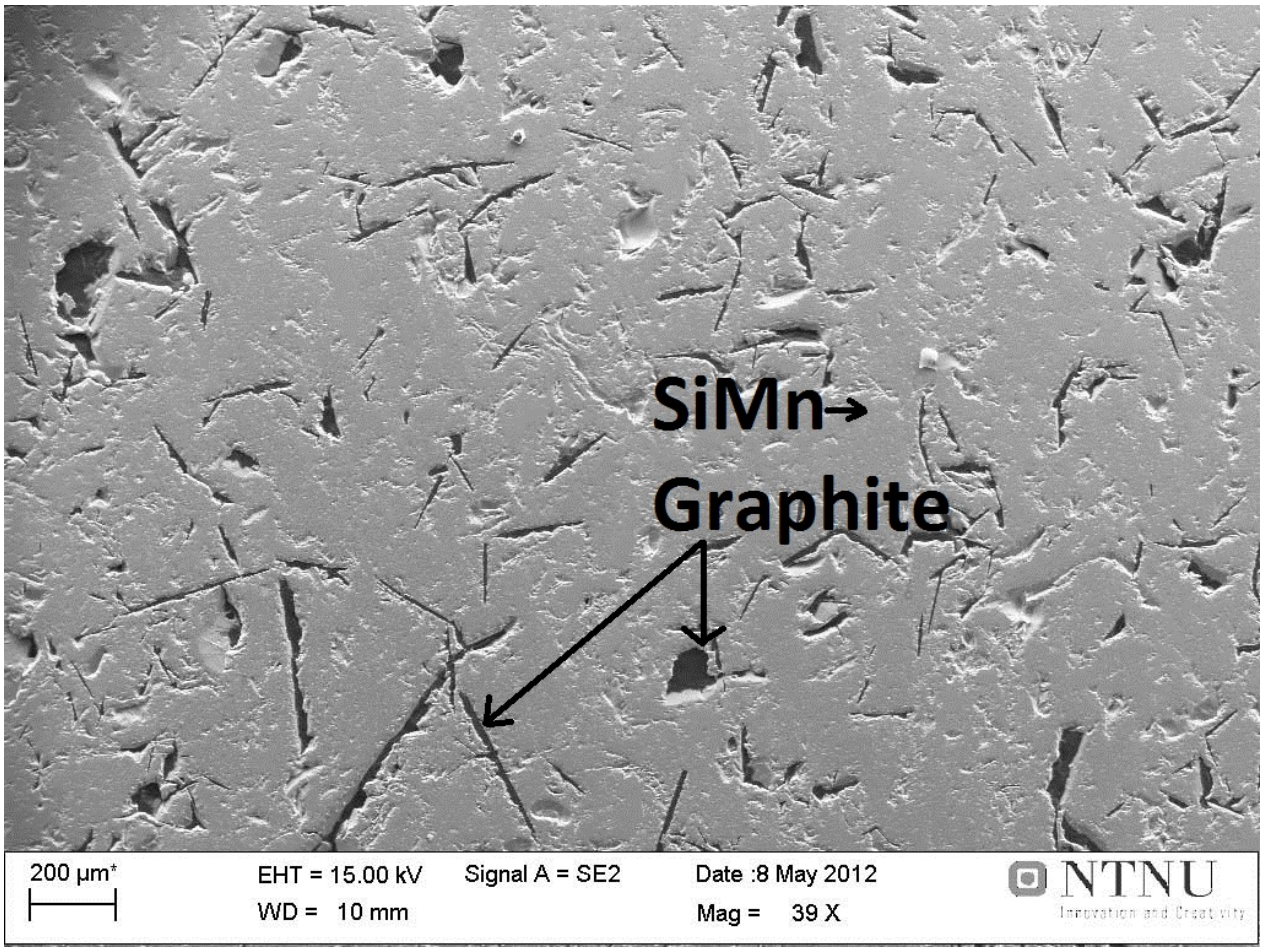

Figure A.23: 2 cycles, bulk of sample 8

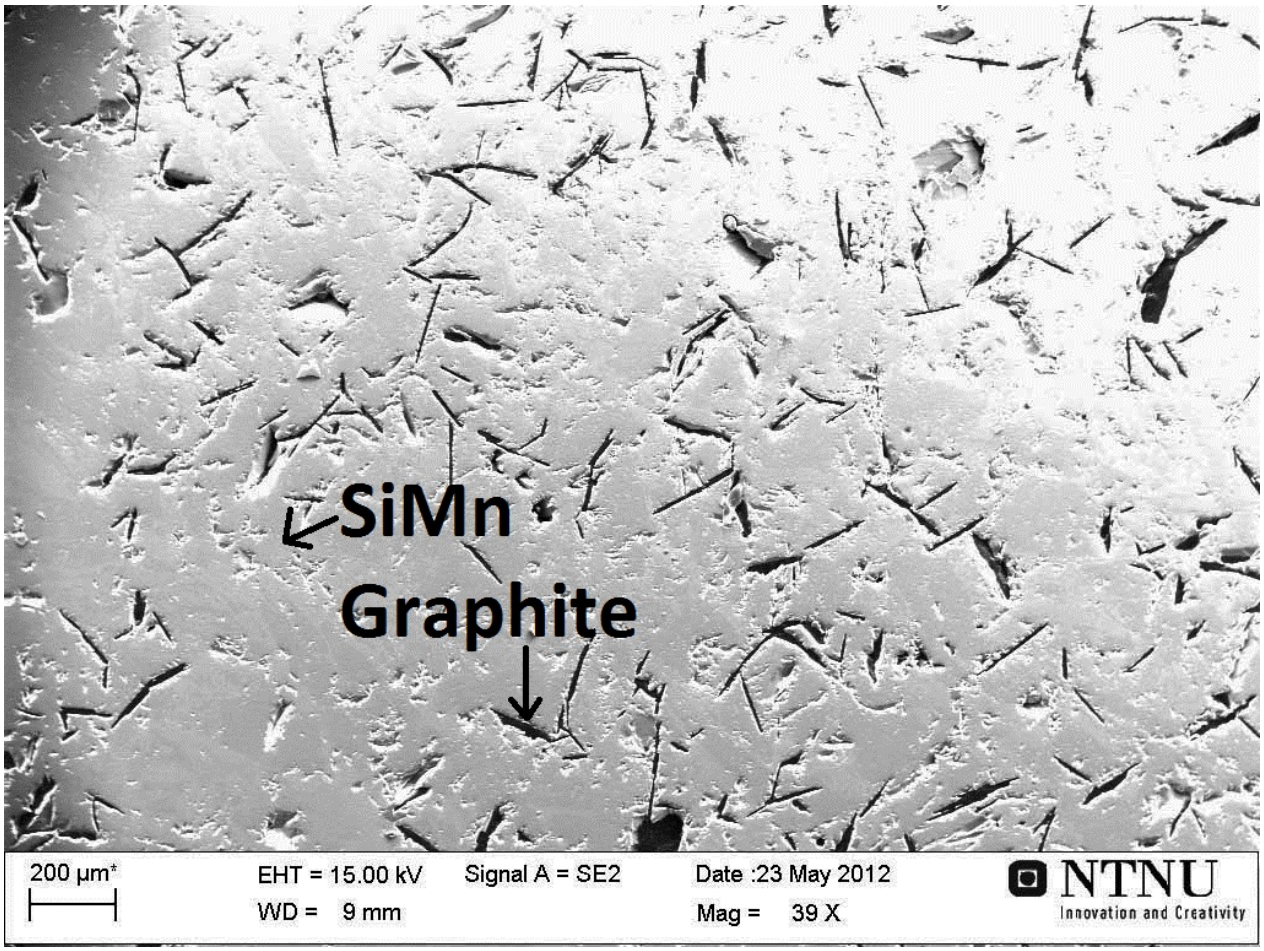

Figure A.24: 4 cycles, bulk of sample 9

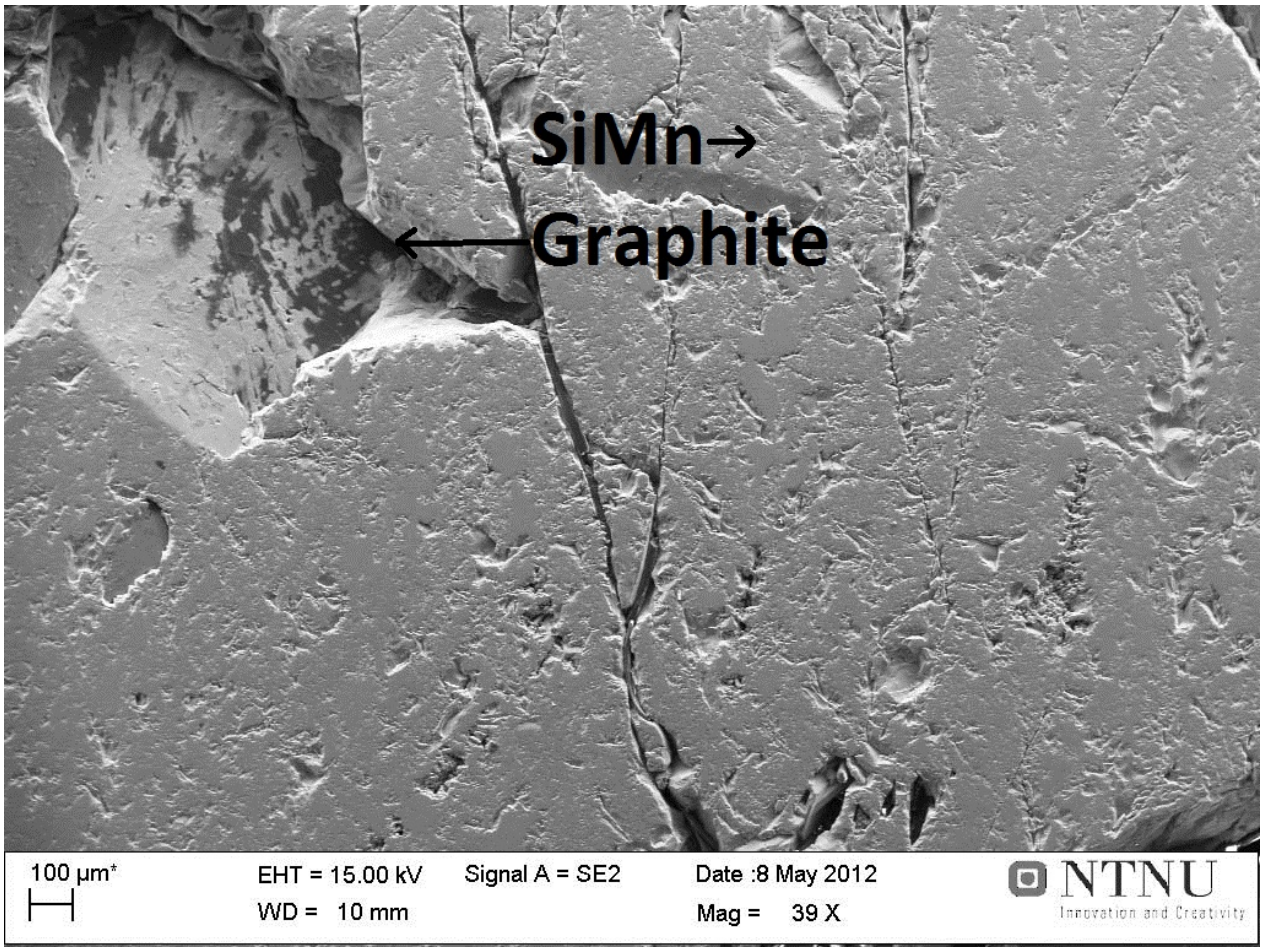

Figure A.25: 1 cycle, bottom of sample 7

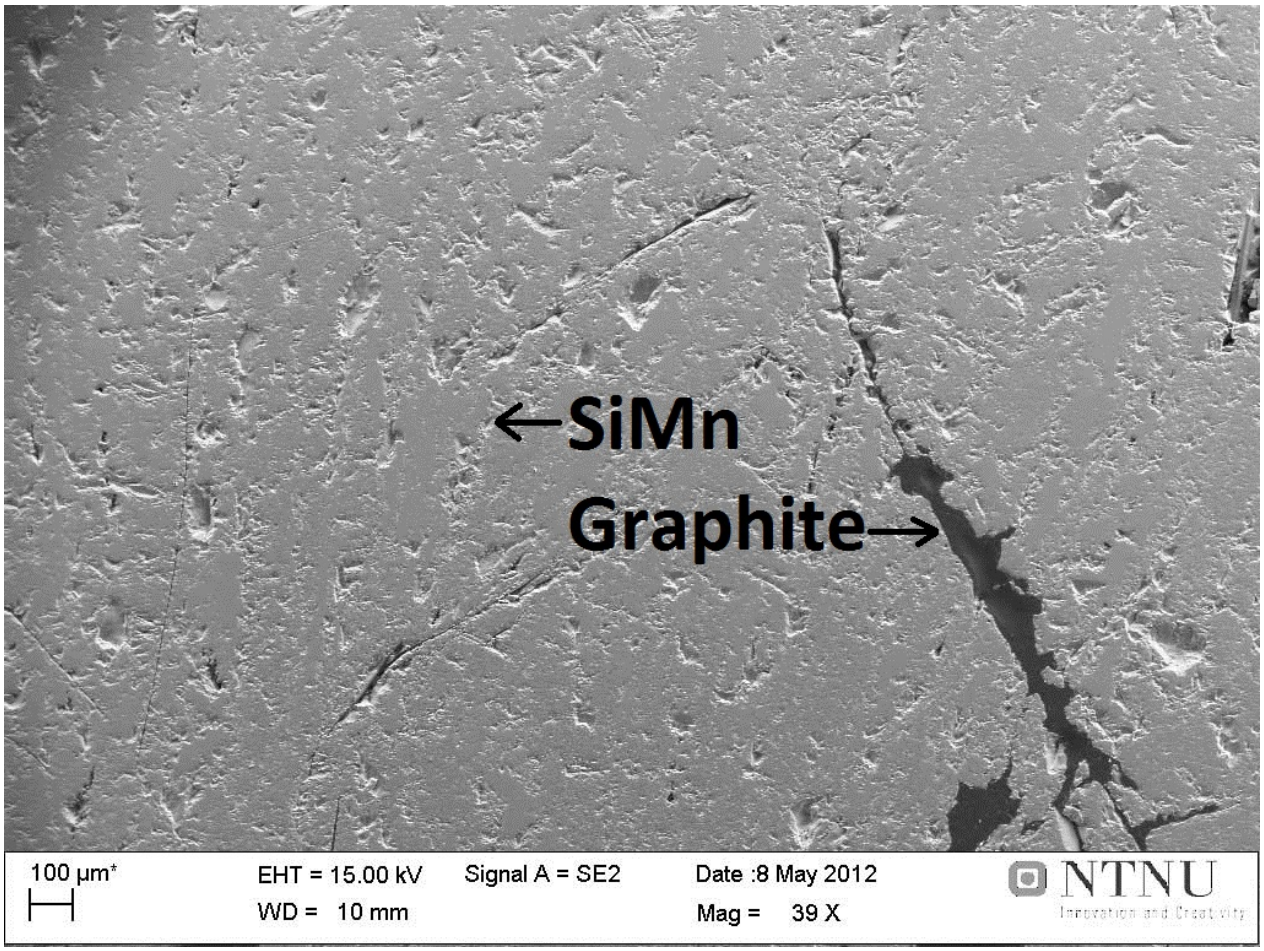

Figure A.26: 2 cycles, bottom of sample 8

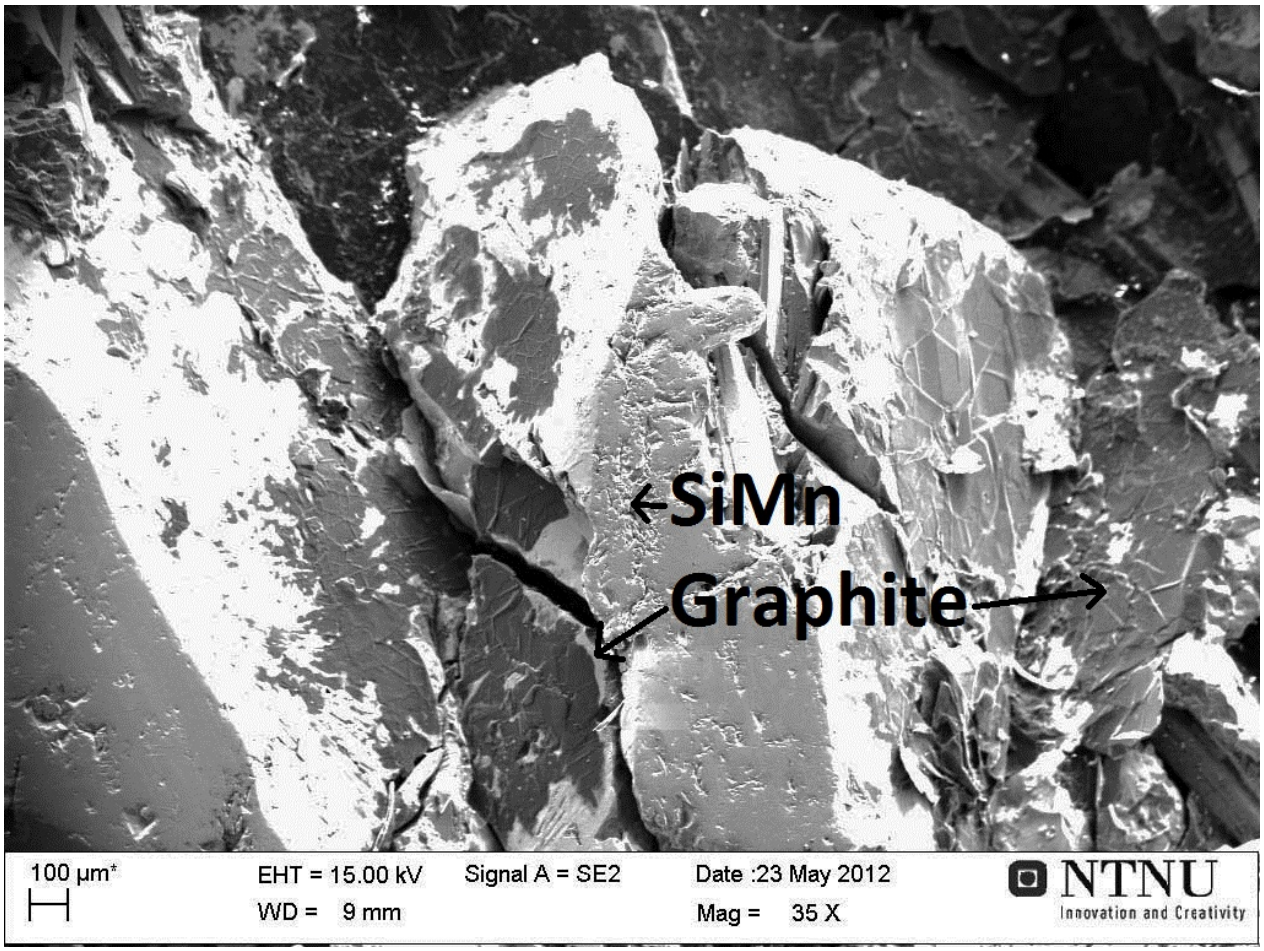

Figure A.27: 4 cycles, bottom of sample 9

Appendix B

Datasheet of the crucible material IG-15

In Figure B.1 the datasheet of the material used to produce the crucibles is presented.

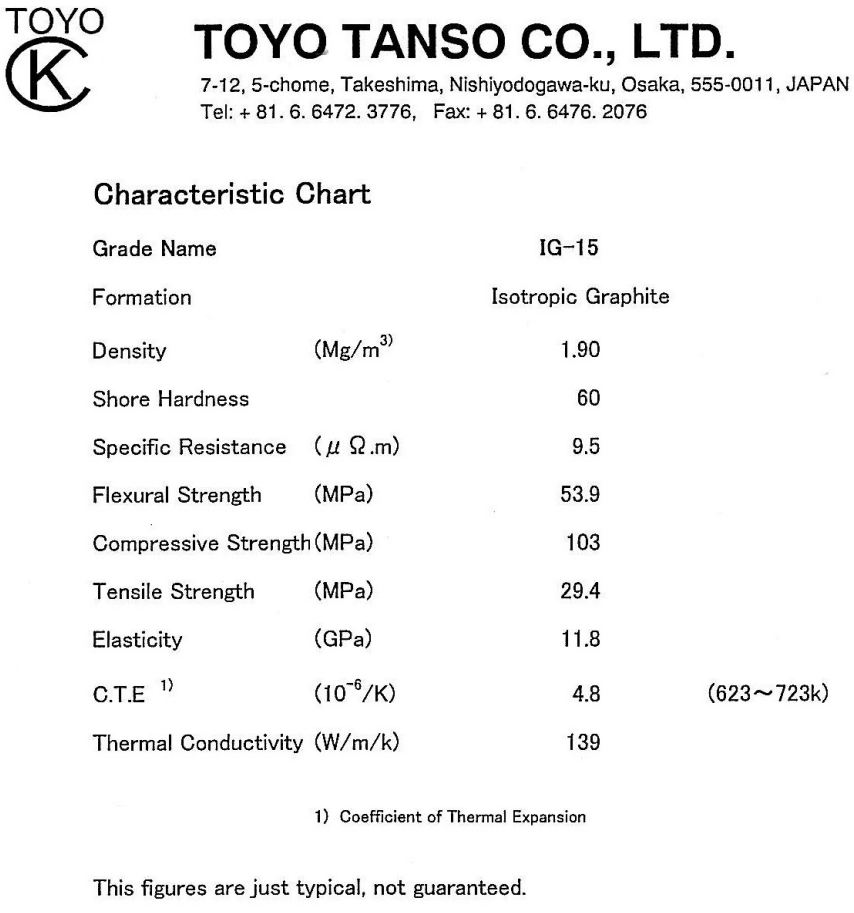

TOYO

TOYO TANSO CO., LTD.

7-12, 5-chome, Takeshima, Nishiyodogawa-ku, Osaka, 555-0011, JAPAN
Tel: + 81. 6. 6472. 3776, Fax: + 81. 6. 6476. 2076

Characteristic Chart

Grade Name		IG-15	
Formation		Isotropic Graphite	
Density	(Mg/m^{3})	1.90	
Shore Hardness		60	
Specific Resistance	($\mu\Omega$.m)	9.5	
Flexural Strength	(MPa)	53.9	
Compressive Strength	(MPa)	103	
Tensile Strength	(MPa)	29.4	
Elasticity	(GPa)	11.8	
C.T.E 1)	(10^{-6}/K)	4.8	(623～723k)
Thermal Conductivity	(W/m/k)	139	

1) Coefficient of Thermal Expansion

This figures are just typical, not guaranteed.

Figure B.1: Datasheet of the material used in the crucibles. Characteristic chart supplied by Tanso (2011).